

PHYSICAL NATURE OF LIGHT-EMITTING CENTERS IN SPARK-PROCESSED
SILICON

By

JELIAZKO G. POLIHRONOV

A DISSERTATION PRESENTED TO THE GRADUATE SCHOOL
OF THE UNIVERSITY OF FLORIDA IN PARTIAL FULFILLMENT
OF THE REQUIREMENTS FOR THE DEGREE OF
DOCTOR OF PHILOSOPHY

UNIVERSITY OF FLORIDA

2002

Dedicated to my wife, Angelina Polihronova

ACKNOWLEDGMENTS

I would like to express my special gratitude to Dr. Rolf Hummel for being my advisor and chairman of the committee that supervised my work. I am very grateful for his support, encouragement and guidance through the years of my graduate studies. I would like to thank him for providing me the opportunity to study in a world-class university, which has enriched my scientific and research experience. I highly appreciate the knowledge I have received about the art of modern engineering and experimental physics. I am grateful to Dr. Hai-Ping Cheng, Dr. Paul Holloway, Dr. Susan Sinnott, Dr. Robert DeHoff and Dr. Adrian Roitberg for the helpful discussions and for serving on my supervisory committee. Many special thanks are extended to Dr. Magnus Hedström for his invaluable contributions to the present work. I appreciate highly the encouragement he has provided and the practical advice for the parameterization and applications of the INDO computer code.

I would like to direct thanks to Dr. Nigel Shepherd, who has been a very good colleague and friend. Many thanks also to Thierry Dubroca, Michele Manuel, Dr. Michael Stora, Dr. Matthias Ludwig and Dr. Fabio Fajardo for their friendship and collaboration. I would like to thank David Burton, Kwanghoon Kim, Anthony Stewart, Grif Wise and Shidong Yu for their help and cooperation.

My sincere gratefulness is dedicated to my spouse Angelina Polihronova and to my daughter Virginia Polihronova for their immeasurable love, encouragement and support.

TABLE OF CONTENTS

	<u>page</u>
ACKNOWLEDGMENTS	iii
ABSTRACT.....	vi
CHAPTER	
1 INTRODUCTION	1
2 THE MOLECULAR ORBITAL THEORY	6
The Hartree-Fock Approximation.....	6
Computational Implementation of the Hartree-Fock Approximation	11
Further Approximations within Hartree-Fock	12
Intermediate Neglect of Differential Overlap (INDO).....	12
Neglect of Diatomic Differential Overlap (NDDO)	13
Configuration Interaction.....	14
3 COMPUTATIONAL METHODS.....	17
Background	17
ZINDO	18
MOPAC: AM1 and PM3	20
4 CALCULATIONS AND RESULTS	25
Known Facts About Spark-processed Silicon.....	25
Research Procedure.....	27
Optical Properties of a-SiO ₂ – based Clusters	29
Optical Properties of Silicon Rings.....	37
Optical Properties of Other Silicon Clusters.....	44
Compound	46
Optical Properties of Silicon Particles in an Amorphous SiO _x N _y matrix	49
The Role of N in the Optical Properties of Spark-processed Silicon	51
Silicon Spark-processed in Pure Oxygen.....	65
Si ₆ Clusters in Spark-processed Silicon.....	67
5 SUMMARY OF RESULTS	72
6 FUTURE WORK.....	75

APPENDIX

A SHORT INTRODUCTION INTO DIFFERENTIAL REFLECTOMETRY	77
B POROSITY AND DENSITY OF SPARK-PROCESSED SILICON [96]	83
Abstract.....	83
Introduction.....	84
Method	85
Results and Discussion	94
Density of Spark-processed Si	97
Conclusions.....	102
LIST OF REFERENCES	103
BIOGRAPHICAL SKETCH	110

Abstract of Dissertation Presented to the Graduate School
of the University of Florida in Partial Fulfillment of the
Requirements for the Degree of Doctor of Philosophy

PHYSICAL NATURE OF LIGHT-EMITTING CENTERS IN SPARK-PROCESSED
SILICON

By

Jeliazko G. Polihronov

December 2002

Chair: Rolf E. Hummel

DEPARTMENT: MATERIALS SCIENCE AND ENGINEERING

Spark-processed silicon (sp-Si) is an amorphous, luminescent material that exhibits *emission* spectra, peaked around 385, 525 and 650 nm. In order to understand the photoluminescence (PL) behavior of sp-Si, UV/visible optical absorption spectra of a large variety of silicon-based molecular clusters were calculated and compared with experimentally measured absorption spectra of sp-Si. All structures in this study were optimized with the AM1 or the PM3 method. The optical absorption spectra were calculated using the quantum-mechanical INDO method together with configuration interaction, which was parameterized for Si.

The experimentally measured *absorption* spectrum of sp-Si exhibits peaks at 245, 277, 325 and 389 nm. In an attempt to reproduce this spectrum computationally, the present work includes a detailed study of the optical properties of silica clusters, Si rings, Si clusters and cages, Si oxides and oxynitrides.

While the spectra of silica, Si rings and OH-terminated Si clusters resemble certain features of the experimental absorption spectrum of sp-Si, remarkable agreement is achieved in the case of a Si cluster, surrounded by an amorphous matrix. The agreement improves when the size of the model Si cluster increases from Si_3 to Si_{14} . χ^2 statistical analysis of the calculated spectra shows that the presence or absence of N influences the optical properties of such complexes.

Silicon spark-processed in pure O does not photoluminesce when excited by laser light having a wavelength of 325 nm. The absorption spectrum of this material differs from the one obtained on Si spark-processed in air. The statistical analysis comparing various cluster models to the two spectra shows that certain Si cluster sizes are favored in the case of Si processed in air, while this is not true for Si processed in O.

CHAPTER 1 INTRODUCTION

Silicon is a material of substantial importance for the electronic industry. It has been studied in a course of decades and is extensively used in the production of electronic elements and integrated circuits. Si is non-toxic, it is readily available and has stable oxides, which are easily deposited and patterned on a Si substrate. Technologically, Si is extracted from common sand (SiO_2) and purified to electronic, high-purity grade material by various crystal growth techniques.

Advanced technology has the goal to create miniaturized, high-speed electronic devices. Utilizing Si for the fabrication of such devices would be highly beneficial due to the advantages of this material. Due to the high speed of light, very high speeds of communication are achieved when optical and electronic devices are integrated on the same chip. However, crystalline Si has an indirect band gap and cannot be used for the production of light-emitting devices.

Recent research efforts have resulted in the development of novel Si-based materials, containing miniature Si particles with nanometer sizes. The physical properties of systems with small dimensions are governed by the laws of quantum mechanics. The band gap of nanometer-sized Si particles is no longer narrow and indirect, thereby allowing emission of light. Therefore, the materials, containing Si nano-particles are of special interest due to the optical properties of the small Si clusters embedded in them. Research efforts have been directed towards the understanding of the physical properties

of such materials with the goal of achieving detailed knowledge of the observed physical phenomena, as well as preparing these materials for technological use.

In 1992, Hummel and Chang [1] developed a new method for preparation of a Si-based luminescent material. The so-called spark-processed Si (sp-Si) photoluminesces in the visible region, having characteristic peaks [2] near 385, 525 and 650 nm, as established by Ludwig [3] (Fig. 1-1, the peak at 650 nm is seen as a shoulder of the dominant blue/green peak). The photoluminescent properties of the material exhibit high stability against etching in buffered hydrofluoric acid, thermal annealing up to 1100 °C and UV irradiation. During the past few years, a number of papers describing and characterizing various properties of sp-Si have been published. The main focus of previous research has been on the optical properties with the goal to provide a description of the photoluminescence (PL) mechanism. Generally, two approaches have been applied—the first approach represents an effort to narrow down the number of possible PL mechanisms utilizing various experimental techniques; the second approach involves experiments to identify the luminescent centers and the physical process of emission.

The first approach has resulted in the elimination of a number of proposed mechanisms [4]. Nevertheless, the PL phenomenon has not been identified with certainty and detail. The second approach is inherently limited since sp-Si, being an inhomogeneous material, is very difficult to characterize at an atomic level. The traditional X-ray diffraction, X-ray absorption and other related methods are not able to provide definitive data in the case of inhomogeneous, multi-phase materials since their results are averaged over the bulk of the material. The average chemical composition of the sp-Si has been studied at various depths with small-spot X-ray Photoelectron

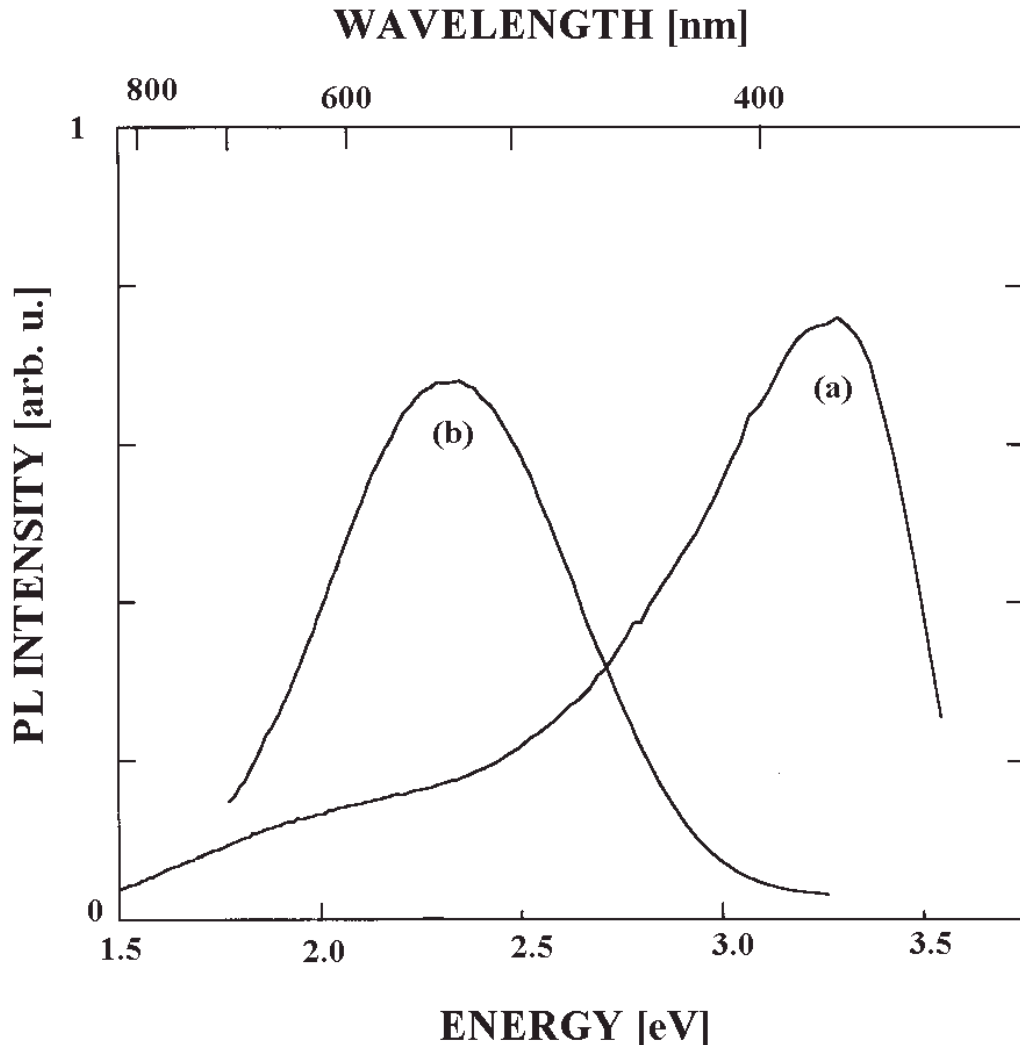


Figure 1-1. Room-temperature PL of (a) blue- (b) green-light emitting sp-Si.

Spectro-meter (XPS, Fig. 1-2). The material predominantly consists of four Si-based phases – amorphous SiO_2 , amorphous and crystalline Si and Si nitrides [3, 5]. Amorphous SiO_2 occupies most of the volume of the material. Crystalline Si and amorphous Si clusters predominate in the areas, close to the Si substrate.

Earlier studies have shown that the presence of N in the ambient during spark processing is essential for the optical properties of sp-Si [3, 6]. Since the origin of the

optical properties of sp-Si is unknown, it is appropriate that all four phases are studied by examining the optical properties of molecular clusters that represent each phase.

To achieve this goal, quantum mechanical calculations have been used in the present work to provide the geometry and optical spectra of the studied molecules. Compared with first-principles calculations, these methods are faster, which allows a large number of molecular clusters to be studied and the average trend of the change of their physical properties to be identified. The calculated spectra of oxygenated Si molecules in the present work are not applicable to sp-Si only; the optical characteristics of any Si- or silica-based light-emitting material can be compared to the present results. The clusters in this work can be related to OH-terminated, Si particles on the surface of materials, or in the bulk when Si particles are buried in amorphous silica; likewise they can describe Si particles, nucleating in the gas phase in the presence of oxygen during laser ablation of Si or related growth processes of Si-based materials from the gas phase. Our results are also applicable to the investigation and characterization of nebulae and interstellar silicate dust clouds. Similar studies have been published in the literature [7 - 11].

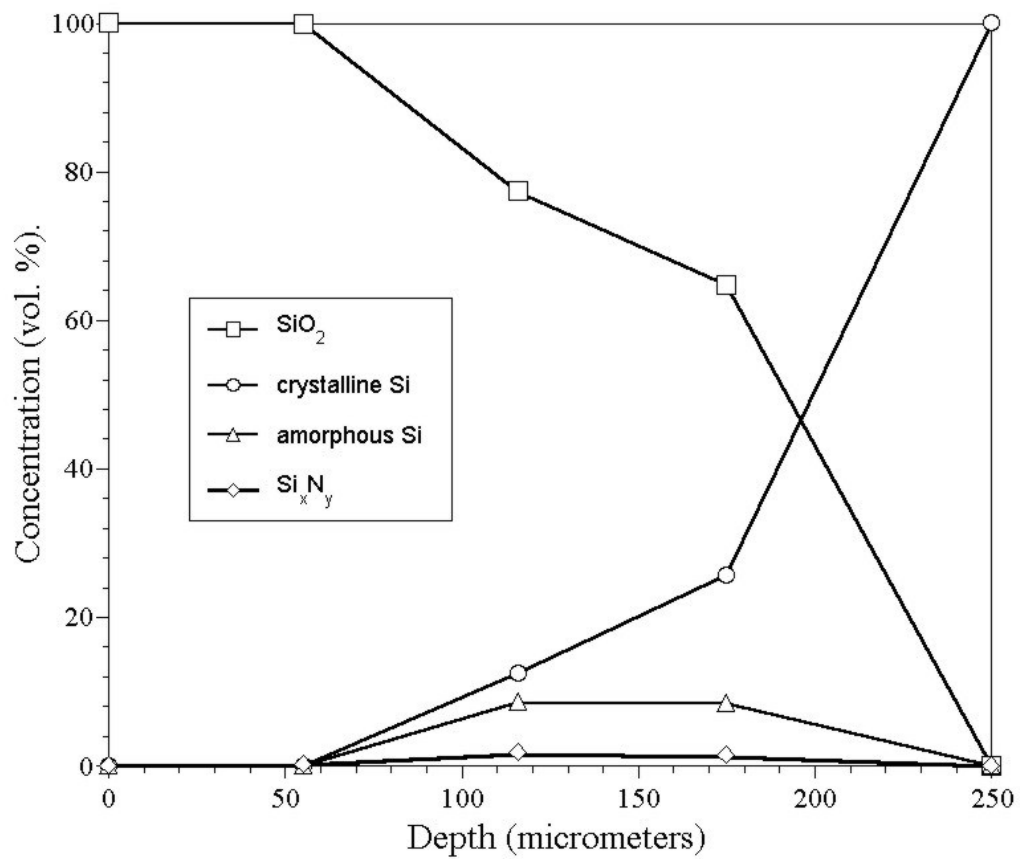


Figure 1-2. Small-spot XPS data for sp-Si. (Adapted from Ludwig [3], Hummel and Ludwig [4], and Ludwig *et al.* [5]).

CHAPTER 2

THE MOLECULAR ORBITAL THEORY

The Hartree-Fock Approximation

Our understanding of the nature of the electronic wave functions in a molecule is based on the understanding of the electronic wave functions in an atom. The theory of the methods used in the present work, treats such systems by considering the valence electrons only; the core electrons and the nucleus of the atom are considered to form an ion, which interacts with the valence electrons. Thus, in all our studies the term “electronic wave function” will be used to describe a wave function of a valence electron.

The problem for the electronic structure of a H-similar atom is commonly treated in the general courses of Quantum Mechanics. It provides knowledge about the appropriate mathematical form of an electronic wave function in an atom:

$$\phi_{nlm} = B \rho^{l+1} e^{-\alpha\rho} L_{n+l}^{2l+1}(\rho) Y_{lm}(\vartheta, \varphi) \quad (2-1)$$

where B and α are constants; n, l and m are the quantum numbers, L is a Laguerre polynomial and Y is a spherical function. The general result is that the radial part of the wave function of an electron in an atom can be approximated as an exponential function:

$$\phi(r) \approx C e^{-Ar}, \quad (2-2)$$

where C and A are constants. Sometimes, $\phi(r)$ is approximated as a sum of Gaussians. In chemistry, the electronic wave functions (2-2) for the atom are called Atomic Orbitals (AO). The Molecular Orbital (MO) Theory has the goal to explain the properties of the electronic wave functions in a molecule. Such wave function in a molecule with n

valence electrons is accepted to be approximately equal to a linear combination of AO's of the type (2-2):

$$\psi_i \approx \sum_{j=1}^n C_{ij} \phi_j \quad (2-3)$$

with coefficients C_{ij} . In chemistry, the above wave function is called a Molecular Orbital (MO).

Since the electrons are Fermions (from the Pauli principle for a system of n undistinguishable particles), the total wave function Ψ of the electronic system in the molecule must be anti-symmetric. Then, it can be represented as a Slater determinant:

$$\Psi(r_1, r_2, \dots, r_n) = \frac{1}{\sqrt{n!}} \begin{vmatrix} \psi_1(r_1) & \psi_1(r_2) & \dots & \psi_1(r_n) \\ \psi_2(r_1) & \psi_2(r_2) & \dots & \psi_2(r_n) \\ \dots & \dots & \dots & \dots \\ \psi_n(r_1) & \psi_n(r_2) & \dots & \psi_n(r_n) \end{vmatrix} \quad (2-4)$$

The Schrodinger equation for the molecule becomes:

$$\hat{H} \Psi(r_1, r_2, \dots, r_n) = E \Psi(r_1, r_2, \dots, r_n) \quad (2-5)$$

where the Hamiltonian operator H is non-relativistic and time-independent. It assumes fixed-ions and has the following form in atomic units ($\hbar = e = m = 1$) [12]:

$$\hat{H} = \frac{1}{2} \sum_k \Delta_k - \sum_i \sum_A \frac{Z_A}{R_{Ai}} + \sum_{i < j} \frac{1}{r_{ij}} + \sum_{A < B} \frac{Z_A}{R_{AB}} \quad (2-6)$$

A, B, 1, 2, ... designate ions; i, j, ... designate electrons and Z_K is the corresponding atomic number.

The equation (2-5) can be solved using the variational principle. A detailed solution has been published by C. C. J. Roothaan [13]. However, if the variational principle is applied over the MO's, this leads to a system of intractable differential equations. This is

the reason why the MO's are approximated as linear combinations of AO's (equation 2-3). Then the variational principle is applied over the AO's and the coefficients C_{ij} .

Substituting eq. (2-6) into (2-5) and multiplying both sides of the resulting equation by Ψ leads to

$$E = \frac{1}{2} \sum_i H_i + \sum_{i,j} (J_{ij} - K_{ij}) \quad (2-7)$$

where J and K are the two-electron Coulomb and exchange operator accordingly:

$$J_{ij} = \left\langle \phi_i(1)\phi_i(2) \left| \frac{1}{r_{12}} \right| \phi_j(1)\phi_j(2) \right\rangle, \quad K_{ij} = \left\langle \phi_i(1)\phi_j(2) \left| \frac{1}{r_{12}} \right| \phi_j(1)\phi_i(2) \right\rangle. \quad (2-8)$$

In the expression (2-7), the ion-related terms are missing, since the variational principle is imposed over a trial wave function Ψ , which contains the ion coordinates R_k as parameters.

Now we introduce another matrix, the so-called overlap matrix S as

$$S_{ij} = \left\langle \phi_i \left| \phi_j \right. \right\rangle. \quad (2-9)$$

Varying (2-7) and the condition for orthonormality of the MO's Ψ_k

$$\delta E = \frac{1}{2} \sum_i \delta H_i + \sum_{i,j} (\delta J_{ij} - \delta K_{ij}) \quad (2-10)$$

$$\delta \langle \psi_i | \psi_j \rangle = \delta (C_i^* S C_j) = (\delta C_i^*) S C_j + C_i^* S (\delta C_j) = 0$$

and using the method of the Lagrangian multipliers, we get

$$\begin{aligned} \left\{ H + \sum_j (J_j - K_j) \right\} C_i &= \sum_j S C_j \epsilon_{ji}, \\ \left\{ H^* + \sum_j (J_j^* - K_j^*) \right\} C_i^* &= \sum_j S C_j^* \epsilon_{ji} \end{aligned} \quad (2-11)$$

where $(-\epsilon_{ij})$ are the Lagrangian multipliers, J_j , K_j are the one-electron Coulomb and exchange operator accordingly:

$$J_j = \left\langle \phi_j(1) \left| \frac{1}{r_{12}} \right| \phi_j(1) \phi_i(2) \right\rangle, \quad K_j = \left\langle \phi_j(1) \left| \frac{1}{r_{12}} \right| \phi_i(1) \phi_j(2) \right\rangle, \quad (2-12)$$

and the matrices C_i are the coefficients for the MO ψ_i from eq. (2-3). It can be shown, that the equations in (2-11) are equivalent, since the participating operators are Hermitian.

Then, if we define the total electron interaction operator G as

$$G = \sum_j (J_j - K_j), \quad (2-13)$$

the one-electron operator H as

$$H_{ij} = \left\langle \phi_i \left| -\frac{\Delta}{2} \right| \phi_j \right\rangle - \sum_B Z_B \left\langle \phi_i \left| \frac{1}{R_B} \right| \phi_j \right\rangle \quad (2-14)$$

and the Fock operator as

$$F = H + G, \quad (2-15)$$

the equations (2-11) become

$$\hat{F} C = S C \epsilon \quad (2-16)$$

in matrix notation. This system of equations is known as Roothaan equations. Here one needs to determine the MO energies, which are in the matrix ϵ ; the matrix C also needs to be calculated as it contains the coefficients of the MO's from eq. (2-3).

We shall then proceed as follows – first, the S matrix will be diagonalized via the transformation

$$W^+ S W = S_{diag} = \begin{vmatrix} s_1 & 0 & \dots & 0 \\ 0 & s_2 & \dots & 0 \\ \dots & \dots & \dots & \dots \\ 0 & 0 & \dots & s_n \end{vmatrix}, \quad (2-17)$$

where W is the transformation matrix. Second, we define the matrix $S^{(-1/2)}$ as

$$S^{(-1/2)} = W S_{diag}^{(-1/2)} W^+ \quad (2-18)$$

in which the matrix

$$S_{diag}^{(-1/2)} = \begin{vmatrix} \sqrt{s_1} & 0 & \dots & 0 \\ 0 & \sqrt{s_2} & \dots & 0 \\ \dots & \dots & \dots & \dots \\ 0 & 0 & \dots & \sqrt{s_n} \end{vmatrix}. \quad (2-19)$$

Now we return to the Roothaan equations (2-16) and proceed to calculating ϵ and C :

$$\begin{aligned} F C &= S C \epsilon \\ S^{(-1/2)} F C &= S^{(-1/2)} C \epsilon \\ S^{(-1/2)} F S^{(-1/2)} S^{(1/2)} C &= S^{(-1/2)} C \epsilon \\ F' C' &= C' \epsilon \\ (C')^+ F' C' &= \epsilon \end{aligned} \quad (2-20)$$

In the last equation, F is in diagonal form and the MO energies ϵ_i can be determined. The coefficients matrix C is calculated as

$$C = S^{(-1/2)} C' \quad (2-21)$$

As a criterion for achievement of self-consistent field (SCF), we shall use the so-called first-order Fock-Dirac density matrix P :

$$P_{ij} = \sum_k C_{ik} C_{jk} n_k, \quad (2-22)$$

where $n = \text{diag}\{n_1, n_2, \dots, n_n\}$; n_k are electron occupation numbers which are 0 or 2 in the case of a closed-shell (zero magnetic moment) molecule. After a number of the described

above consecutive approximations, the matrix elements P_{ij} will reach convergence. Then we can say that a self-consistent field (SCF) has been obtained and the Hartree-Fock approximation is complete.

Computational Implementation of the Hartree-Fock Approximation

The SCF-based computer routines normally follow the following procedure [12]:

- Calculate the integrals necessary to form the Fock matrix F (equation 2-15).
- Calculate the overlap operator's matrix S (2-9).
- Perform diagonalization of S (equation 2-17).
- Calculate $S_{diag}^{(-1/2)}$ and form $S^{(-1/2)}$ (equation 2-18).
- Form the Fock matrix F as:

$$F_{ij} = \left\langle \phi_i \left| -\frac{\Delta}{2} \right| \phi_j \right\rangle - \sum_B Z_B \left\langle \phi_i \left| \frac{1}{R_B} \right| \phi_j \right\rangle + \sum_{k,l} P_{kl} \left\{ \left\langle \phi_i(1) \phi_k(2) \left| \frac{1}{r_{12}} \right| \phi_j(1) \phi_l(2) \right\rangle - \frac{1}{2} \left\langle \phi_i(1) \phi_k(2) \left| \frac{1}{r_{12}} \right| \phi_l(1) \phi_j(2) \right\rangle \right\} \quad (2-23)$$

- Calculate F' (equation 2-20).
- Diagonalize F' (the last equation in 2-20) and obtain the energy eigenvalues ϵ_k .
- Calculate the coefficients C_{ij} (equation 2-21).
- Calculate the density matrix P (equation 2-22).
- Check P for convergence. If the desired convergence tolerance has been reached, then stop.
- If convergence has not been reached, extrapolate a new density matrix and repeat steps 5 – 10 until SCF is reached.
- Output the results it a text format.
- Plot the calculated absorption spectra
- Optional: calculate the electron transition amplitudes for all excitations

Further Approximations within Hartree-Fock

Intermediate Neglect of Differential Overlap (INDO)

The INDO approximation represents further simplification of the Hartree-Fock method. Certain approximations are being accepted with the goal to increase calculation efficiency. Detailed treatment of the INDO method has been published [12, 14 - 17].

Generally, S_{ij} is the overlap matrix (equation 2-9). It is approximated so that products $\phi_i(1) \phi_j(1)$ are retained only in one-center integrals. However, the computational efficiency of INDO is achieved mainly due to the approximations of the total electron interaction operator G (equation 2-13). G_{ij} is a sum of two-, three-, and four-center integrals of the type

$$\int \phi_i(1) \phi_j(1) \frac{1}{r_{12}} \phi_k(2) \phi_l(2) dv_1 dv_2 , \quad (2-24)$$

which are set to zero unless $i = l$ and $j = k$. Those that remain are set as parameters and their values determined from atomic spectroscopy.

H is approximated as follows:

$$H_{ii}^{AA} \approx \langle \phi_i | -\frac{\Delta}{2} - \frac{Z_A}{R_A} | \phi_i \rangle - \sum_{B \neq A} \langle \phi_i | \frac{Z_B}{R_B} | \phi_i \rangle \quad (2-25)$$

$$H_{ij}^{AA} \approx \langle \phi_i | -\frac{\Delta}{2} - \frac{Z_A}{R_A} | \phi_j \rangle \quad (2-26)$$

$$H_{ij}^{AB} = \beta_{ij} \approx \beta_{AB}^0 S_{ij} \approx \frac{1}{2} (\beta_A^0 + \beta_B^0) S_{ij} \quad (2-27)$$

where Δ is the Laplacian operator, Z_A is the core charge of atom A, R_A is the distance between the i-th electron and ion A. β_{ij} is referred to as a “resonance integral” and is approximated via the parameters β_{AB}^0 , β_A^0 and β_B^0 .

Neglect of Diatomic Differential Overlap (NDDO)

NDDO is defined by the substitution

$$\phi_i^A(r) \phi_j^B(r) d^3r \rightarrow \delta_{AB} \phi_i^A(r) \phi_j^B(r) d^3r, \quad (2-28)$$

where A and B denote two different atoms (sometimes referred to as centers) and δ is the Kronecker symbol. In this situation, the Fock matrix will have the following elements [12]: One-atom diagonal elements

$$\begin{aligned} F_{ii}^{AA} = & \left\langle \phi_i^A \left| -\frac{\Delta}{2} - \frac{Z_A}{R} \right| \phi_i^A \right\rangle + V_{AA} + \\ & + \sum_{\substack{k,l \\ B \neq A}} P_{kl} \left[\left\langle \phi_i^B \phi_k^B \left| \phi_i^B \phi_l^B \right. \right\rangle - \frac{\left\langle \phi_i^B \phi_k^B \left| \phi_l^B \phi_i^B \right. \right\rangle}{2} \right] - \\ & - \sum_{B \neq A} Z_B \left\langle \phi_i^B \left| \frac{1}{R_B} \right| \phi_i^B \right\rangle \end{aligned} \quad (2-29)$$

where V_{AA} is the so-called effective ion potential, being determined from experimental measurements. V_{AA} prevents the valence electrons of atom A from penetration into its inner orbitals. One-atom off-diagonal elements

$$\begin{aligned} F_{ij}^{AA} = & \sum_{B \neq A} \sum_{k,l} P_{kl} \left\langle \phi_i^B \phi_k^B \left| \phi_j^B \phi_l^B \right. \right\rangle - \sum_{\substack{k,l \\ A}} P_{kl} \frac{\left\langle \phi_i^B \phi_k^B \left| \phi_l^B \phi_j^B \right. \right\rangle}{2} - \\ & - \sum_{B \neq A} Z_B \left\langle \phi_i^B \left| \frac{1}{R_B} \right| \phi_i^B \right\rangle \end{aligned} \quad (2-30)$$

Two-atom off-diagonal elements

$$F_{ij}^{AB} = H_{ij}^{AB} - \sum_k^A \sum_l^B P_{kl} \frac{\left\langle \phi_i^A \phi_l^B \left| \phi_k^A \phi_j^B \right. \right\rangle}{2} \quad (2-31)$$

where H_{ij}^{AB} is given by equation (2-14). It is also important to note that NDDO includes orbital anisotropies.

Configuration Interaction

The Hartree-Fock approximation enables us to solve the Schrödinger equation for a molecule and provides us with the molecular wave function $\Psi(r_1, r_2, \dots, r_n)$ (equation 2-5) of the ground state and its energy ε_0 . This energy is an upper bound to the true ground state energy E_0 . The difference between these two values is called correlation energy η_{corr} :

$$\eta_{corr} = E_0 - \varepsilon_0. \quad (2-32)$$

The correlation energy accounts for interactions between valence electrons in the molecule and amounts up to 1% of E_0 . Despite that the percentage is small, it is equivalent to a few eV. Therefore, the Hartree-Fock approximation can be further improved. The improvement will provide the value of η_{corr} (or at least part of it) as well as improved ground-state wave function of the molecule Φ . In addition, it will allow us to calculate the energies and wave functions of the excited states and thus enable us to predict the optical absorption spectrum of the molecule.

The correction of the Hartree-Fock approximation can be achieved via the so-called configuration interaction (CI), also known as configuration mixing. It has been shown in perturbation theory [18] that the molecular wave function contains contributions from various electronic configurations. We shall express this dependence as a linear combination [19]

$$\Phi = \Psi + \sum_{a,r} C_a^r \Psi_a^r + \sum_{\substack{a < b \\ r < s}} C_{ab}^{rs} \Psi_{ab}^{rs} + \sum_{\substack{a < b < c \\ r < s < t}} C_{abc}^{rst} \Psi_{abc}^{rst} + \sum_{\substack{a < b < c < d \\ r < s < t < u}} C_{rstu}^{abcd} \Psi_{abcd}^{rstu} + \dots, \quad (2-33)$$

where Ψ is the Hartree-Fock wave function of the ground state, Φ is the improved ground state function, C_a^r are coefficients and Ψ_a^r are called “excited determinants”. The excited determinants are built from the function Ψ , as its a-th and the r-th row have

exchanged places (which is, electron from a-th MO has been excited into the r-th virtual MO). Each of these Slater determinants represents a different configuration. The first sum in equation (2-33) represents single excitations; the second, double excitations; the third, triple excitations, and so on. Usually, the above equation is truncated and only single excitations are calculated:

$$\Phi \approx \Psi + \sum_{a,r} C_a^r \Psi_a^r, \quad (2-34)$$

known as CI-S (CI-singles). For a Si-based molecule with 10 – 15 atoms, the number of the excited determinants in the above sum (also known as CI size) is set to be around 65, in order to provide good approximation. If the CI size is increased above this number, the calculated energies do not improve.

The application of the variational principle to the coefficients C_a^r leads to the secular equation

$$\det(H - ES) = 0, \quad (2-35)$$

where H is the CI matrix, written in a block form

$$\begin{bmatrix} \langle \Psi | \hat{H} | \Psi \rangle & \hat{0} \\ \hat{0} & \langle \Psi_a^r | \hat{H} | \Psi_a^r \rangle \end{bmatrix}, \quad (2-36)$$

\hat{H} is the hamiltonian of the system, E is a column of the energies of the CI excited states, and S is the overlap matrix for the CI wavefunctions. The energies E are the eigenvalues of H , while its eigenfunctions

$$\Psi_{CI} = \sum_{a,r} C_a^r \Psi_a^r \quad (2-37)$$

are also called CI vectors. The zero parts in the CI matrix are due to integrals of the type

$$\langle \Psi | \hat{H} | \Psi_a^r \rangle, \text{ which are equal to zero according to the Brillouin's theorem [19].}$$

If Ψ is the wave function of the ground state, Ψ_{EXC} is the wave function of the excited state (one of the CI vectors) and \hat{r} is the operator of distance, then the probability of transition (also known as oscillator strength) is proportional to the square of

$$\langle \Psi_{EXC} | e\hat{r} | \Psi \rangle \langle \psi_v | \psi_\mu \rangle, \quad (2-38)$$

where $\Psi_{v,\mu}$ are the vibrational wave functions and their overlap is called a Frank-Condon factor. The first term (or rather, its square) determines the transition intensity, while the second term gives the overlap of the two vibrational functions and determines the shape of the line.

In order to justify the use of the calculated excited state energies from equation (2-35), one needs to apply the Frank-Condon principle, which states that the excitation (absorption) transitions are vertical, that is, the electrons move faster than the nuclei in the molecule.

The calculated absorption spectrum $f(E)$ containing a total of N transitions, has the form

$$f(E) = \frac{2.355}{\Delta\sqrt{2\pi}} \sum_{k=1}^N p_k e^{-2.773\left(\frac{E-E_{0k}}{\Delta}\right)^2}. \quad (2-39)$$

In this work, each individual spectral line is assumed to have a Gaussian shape with adopted full width at half maximum Δ equal to 0.4 eV and a height p_k , called an oscillator strength (calculated as the square of equation 2-38).

CHAPTER 3

COMPUTATIONAL METHODS

Background

There are several different methods available for studying chemical and physical properties of materials at the atomic level. The most accurate is based entirely on quantum mechanics without inclusion of adjustable parameters other than the quality of the basis set expansion of the wave functions. The other extreme is classical molecular dynamics, based on empirically determined interaction potentials between the atoms that constitute the material or molecule under investigation. There are also various tight-binding schemes (TB) that are quantum mechanical but rely heavily on empirical fitting and therefore lack transferability to other systems, and bonding situations and so on, for which they have not been parameterized.

Since the goal of the present work is to describe the optical properties of a real material, one needs a fast and efficient method that allows a large variety of molecular structures to be investigated. The most accurate methods are quite insufficient in that respect, while the semi-empirical quantum-mechanical methods provide the efficiency of calculation and acceptable accuracy. As it has already been described in Chapter 2, the various semi-empirical methods use the approximation of Hartree-Fock for calculation of the ground state energy of the molecule and the energy levels of its electrons. The difference between the various methods is in the Hamiltonian they use, namely:

- The Hamiltonian operator is approximated in various ways within the different methods;

- The Hamiltonian operator is parameterized with semi-empirical parameters, which are specific for the given Zero Differential Overlap (ZDO) method.

ZINDO

This method is known also as INDO/S or INDO/CI [16, 17] and has been developed by Prof. Michael C. Zerner at the Quantum Theory Project at the University of Florida. The method is based on the Hartree-Fock approximation and uses CI for calculation of optical spectra. The accuracy of prediction of the optical transition energies is 2000 cm^{-1} , or 0.25 eV [12, 20].

The method has been successfully used in numerous studies of organic and organo-metallic compounds and the parameters for H, C, N and O in particular have been previously optimized to reproduce optical absorption spectra. Theoretical parameters for Si, as well as those taken from atomic spectroscopy, have been implemented in the program code.

In ZINDO, 31 theoretical/empirical parameters are used [21]. The following is a list of the ZINDO parameters and their applicability for calculations of Si molecular systems:

- 1, 2: ζ_s , ζ_p : Slater orbital exponents—according to Zerner [12, 22, 23], these are taken from Santry and Segal [24] for Si atoms;
- 3-6: ζ_{d1} , its coefficient C_1 , ζ_{d2} and its coefficient C_2 . It is important to note that d-orbitals are not used in the calculation for Si atoms;
- 7-9: I_s , I_p , and I_d —ionization potentials for Si published by Santry and Segal [24] (atomic data for Si);
- 10-12: β_s , β_p and β_d (resonance integrals). In the case of Si, β_d is neglected, $\beta_{sp} = -9\text{ eV}$ [25];
- 13-20: $F_{2(p,p)}$, $G_{1(s,p)}$, $F_{2(p,d)}$, $F_{2(d,d)}$, $F_{4(d,d)}$, $G_{1(p,d)}$, $G_{2(s,d)}$, $G_{3(p,d)}$ —Slater-Condon factors, published by Bacon and Zerner [23] for Si. These seven parameters are used in the module INDO/1 for geometry optimizations;

- 21, 22: Eatom–electronic energy of an isolated atom; Hatom - heat of formation of an isolated atom–these two parameters are known from experimental atomic data;
- 23-25: Is,a, Ip,a, Id,a–second set of ionization potentials, involving transitions to d orbitals and are thus neglected in the case of Si;
- 25-28: C1, C2 and C3,a–fractional contributions of d-configurations to the core integral–neglected in the case of Si;
- 29-31: γ_{ss} , $\gamma_{\sigma\delta}$, γ_{dd} –two-electron one-center Coulomb integrals–calculated from the Slater orbitals for Si, taken from Santry and Segal [24].
- Other parameters are set to be constants, such as $f_\pi=0.585$, $f_\sigma=1.267$, for singlets excitations. The two-center, one-electron integrals are used to calculate some of the overlap matrix elements S_{ij} and are treated as parameters.

Before INDO/S was used in this study, there was a need to re-optimize the β parameter for Si (Eq. (2-27)). In the literature, there are a number of papers that provide experimentally measured IR spectra as well a UV/visible absorption spectra for molecules containing Si [26 - 33]. Only molecules that contain Si and atoms, for which the INDO/S has been previously parameterized, were selected. In the chosen structures, Si participated with both π - (for instance, in the cases of silabenzene and H_2SiCH_2) and σ -bonding (for instance, in the cases of Me_6Si_2 , $(Me_2Si)_5$ and $(Me_2Si)_6$). The geometry of these molecules was optimized with the Austin Method 1 (AM1), predicting bond length within a few percent of the corresponding experimental values. The absorption spectra were calculated with the INDO/S for each molecule for various values of β .

Let us consider a total of N Si-containing compounds. The experimentally measured absorption spectrum of each compound will exhibit electronic transitions with energies E_1, E_2, \dots, E_{M_k} where M_k is the total number of transitions for a given compound. If the calculated prediction of a transition energy is denoted as $e_k(\beta)$, then

$$Err(\beta) = \sqrt{\frac{\sum_{k=1}^N \sum_{j=1}^{M_k} (e_k(\beta) - E_j)^2}{\sum_{k=1}^N M_k}} \quad (3-1)$$

is the average error, associated with a given value of β .

The smallest average deviation was found to be 0.24 eV, which is achieved at $\beta(\text{Si}) = -9$ eV. Table 3-1 shows a comparison between theoretical and experimental values for a variety of transitions of ten different Si-containing compounds. It has to be emphasized, that the error of 0.24 eV in the calculated transition energies, comes as a result of both MOPAC geometry optimization and INDO/S spectroscopic calculation.

In conclusion, ZINDO is an INDO-based FORTRAN code, which allows one to calculate optical absorption spectra (electronic structure) of molecules, containing the elements H, Li, B, C, N, O, F, Si, P, S, Sc, Ti, V, Cr, Mn, Fe, Co, Ni, Cu and Zn with a precision of 0.25 eV. Other elements have also been parameterized by research groups.

MOPAC: AM1 and PM3

In the 1970s, the MINDO/3 and MNDO codes (Zerner [12] and the references therein) have been introduced. They represent a “Modified version of INDO”, specifically parameterized for prediction of geometries and heats of formation of molecules. A brief explanation of the Fock matrix elements within MINDO/3 and MNDO as well as a discussion on their parameterization can be found in the literature [12].

Both MINDO/3 and MNDO are NDDO-based. The first practical program that contained both approximations was the code MOPAC [34, 35]. It has been parameterized for geometry optimization of molecules, vibrational frequency spectra, heats of

formations and other properties [12]. However, the inability of MNDO to successfully model hydrogen bonding has led to the development of the Austin Model 1 (AM1) and the Parametric Method 3 (PM3), the last being the third parameterization of MNDO.

Table 3-1. Comparison between experimentally measured and theoretically calculated transition energies and wavelengths for various Si-containing molecules

Compound	Experiment [eV]	INDO/S [eV]
$(CH)_5SiH$ [26]	3.88	4.28
	4.56	4.59
	5.85	5.56
H_2SiCH_2 [28]	4.68	4.68
$MeSi(CH)_5$ [29]	4.00	4.20
	3.85	4.20
$(CH)_6(CH_2)_2MeSi$ [29]	4.72	4.96
$Me_2Si(CH)_2$ [30]	4.53	4.46
	5.12	5.06
$Me(H)SiCH_2$ [31]	4.77	5.15
Me_6Si_2 [32]	6.43	6.60
	7.52	7.90
Me_2Si [33]	2.76	2.95
Me_2Si_5 [33]	4.68	4.83
Me_2Si_6 [33]	5.17	5.10

It is important to note that since AM1 and PM3 are both NDDO-based, they are therefore founded on the Hartree-Fock approximation. In AM1 and PM3, the variational principle is applied to the AOs and the molecular wave function, as described in Chapter 2. However, the coordinates $\{R_k\}$ of the atoms in the molecule are also varied until the condition

$$\frac{\partial U}{\partial R_k} = \text{grad } U = -\vec{F}_k = 0 \quad (3-2)$$

is satisfied, that is, until the forces acting on the different atoms are reduced to zero. U represents the potential of interaction between the atoms in the molecule.

The Hartree-Fock method and the variational principle are applied multiple times, while the coordinates $\{r_k\}$ are being varied at each step, searching for a minimum of the norm of the gradient in equation (3-2). The common mathematical procedures for searching of the potential energy minimum are the method of the steepest descent, the method of the conjugate gradient, Newton-Raphson and eigenvector following [21]. Detailed description of these methods can be found in any textbook of numerical methods.

During the Hartree-Fock NDDO calculation, various empirical parameters are used, many of which have been listed in Section 2.2. Other parameters, specifically introduced in MNDO, and their influence on the geometry calculations are described in the literature [12, 34].

MOPAC can calculate 32 different molecular properties [34]. The study of sp-Si did not require the use of all 32 and therefore attention will be given only to the quantities, applicable to the present research work.

The heat of formation ΔH_f of a molecule is calculated as follows: the Hartree-Fock approximation applied to a system of n valence electrons in a molecule results in a density, P , and Fock matrix, F . The one-electron matrix H , together with the matrices P and F , participate in the expression for the total electronic energy

$$E_{electron} = \frac{1}{2} \sum_{\mu=1}^n \sum_{\nu=1}^n P_{\mu\nu} (H_{\mu\nu} + F_{\mu\nu}). \quad (3-3)$$

If the energy of repulsion between two nuclei is E_n^{pair} , then the total energy of repulsion between nuclei in the molecule will be given by

$$E_{nuclear} = \sum_A \sum_{B < A} E_{nucl}^{pair}(A, B). \quad (3-4)$$

The energy necessary to strip all the valence electrons off atom A will be denoted as $E_{ioniz}(A)$ and the total energy necessary to take all atoms from the whole molecule to infinity will be E_{atomiz} . Then the heat of formation of a molecule, calculated by the semi-empirical methods AM1 and PM3 at a temperature of 298 K in the gas phase is given by the expression [35]

$$\Delta H_f = E_{electron} + E_{nuclear} + \sum_{all\ atoms} E_{ioniz}(A) + E_{atomiz}. \quad (3-5)$$

$E_{ioniz}(A)$ is calculated using empirical parameters. A detailed procedure and description of these parameters has already been published. [34, 35]. The atomization energy for the atoms in the molecule is

$$E_{atomiz} = E^{SCF} - \sum_{all\ atoms} E^{(0)SCF}(A), \quad (3-6)$$

$E^{(0)SCF}(A)$ being the lowest total energy for an isolated atom A in the self-consistent field (SCF) approximation. For a cluster, containing a total of n_a atoms, one can define average atomization energy per atom as

$$\langle E_{atomiz} \rangle = \frac{1}{n_a} \left[E_{SCF} - \sum_{k=1}^{n_a} E_k^{(0)SCF} \right]. \quad (3-7)$$

It determines how strongly an atom is bound to the other atoms and therefore could be used as a measure of the stability of the molecule.

In conclusion, MOPAC allows one to calculate 32 different molecular properties, between which are the optimal atomic coordinates of a molecule (optimized geometry), its heat of formation and ground state energy. ΔH_f , being a result of the above semi-empirical methods, is useful when two molecules are compared. The relative difference

of the heats shows the energy expenditure necessary for the transformation of one molecule to another.

CHAPTER 4 CALCULATIONS AND RESULTS

Known Facts About Spark-processed Silicon

Spark-processed Si (sp-Si) has been thoroughly studied since 1992, when found to have visible PL at room temperature [1]. However, a large set of its properties have technological importance only and as such will not be considered here. Some of the characteristics of the material yield important information about the light-emitting centers as follows:

- Sp-Si grown in air has PL spectra, which exhibit consistently three peaks: blue, green and red (peaking around 385, 525 and 650 nm respectively). This fact suggests that *similar light-emitting centers are being formed always, when crystalline Si (c-Si) is spark-processed in air.*
- Temperature behavior of the PL suggests that quantum confinement is not the mechanism of emission [3]. Therefore, *c-Si or c-Si particles are not required in the modeling of the light-emitting centers.* However, the present study includes a limited number of c-Si clusters for the sake of completeness.
- The PL of sp-Si is highly resistant against etching in hydrofluoric acid, aging, UV irradiation and thermal annealing up to 1100°C . This fact suggests that *the emitting centers occupy stable molecular geometries up to 1100°C .*
- X-ray diffraction studies [3, 36] show that sp-Si contains amorphous phases. This fact suggests that the emitting centers, although similar throughout the bulk, are positioned in different atomic surroundings. In other words, *the emitting centers belong to the same family of molecular clusters and have similar characteristics, but do not have identical molecular geometries.*
- Small-spot X-ray electronic spectroscopy (XPS) studies of sp-Si show that the material consists of four phases: amorphous SiO_2 (a- SiO_2), a-Si, c-Si and SiN_x or Si oxynitrides [3, 5]. This fact suggests that *the luminescent centers are located in one of these phases or at an interface between them.*
- Earlier studies [4] on sp-Si show that its PL does not originate from SiO_2 . Therefore, *the emitting centers do not originate from the SiO_2 .*

- An earlier study [3, 37] states that the PL decay time of sp-Si is in the order of nanoseconds. A more recent study suggests decay times in the order of picoseconds [6]. In either case, the decay times are fast and it seems therefore that charge or energy transfer mechanisms in PL are not likely. *The absorption and emission of a photon occur on the same center.* This fact is also confirmed by preliminary PLE (photoluminescence excitation, Figure 4-1) and absorption spectra of sp-Si, both showing identical peaks [38]. The absorption spectrum of sp-Si was measured by a differential technique, called differential reflectometry. Line-shape analysis of the differential reflectogram (DR) is presented in Appendix A.
- Sp-Si is a diluted magnetic semiconductor and exhibits ferromagnetic properties. They are annealed out at around 600°C . The PL properties are observed after thermal annealing until at least 1100°C . This fact suggests that the two phenomena are not related and *the light emitting centers are probably non-magnetic, having singlet ground states (zero spin).*

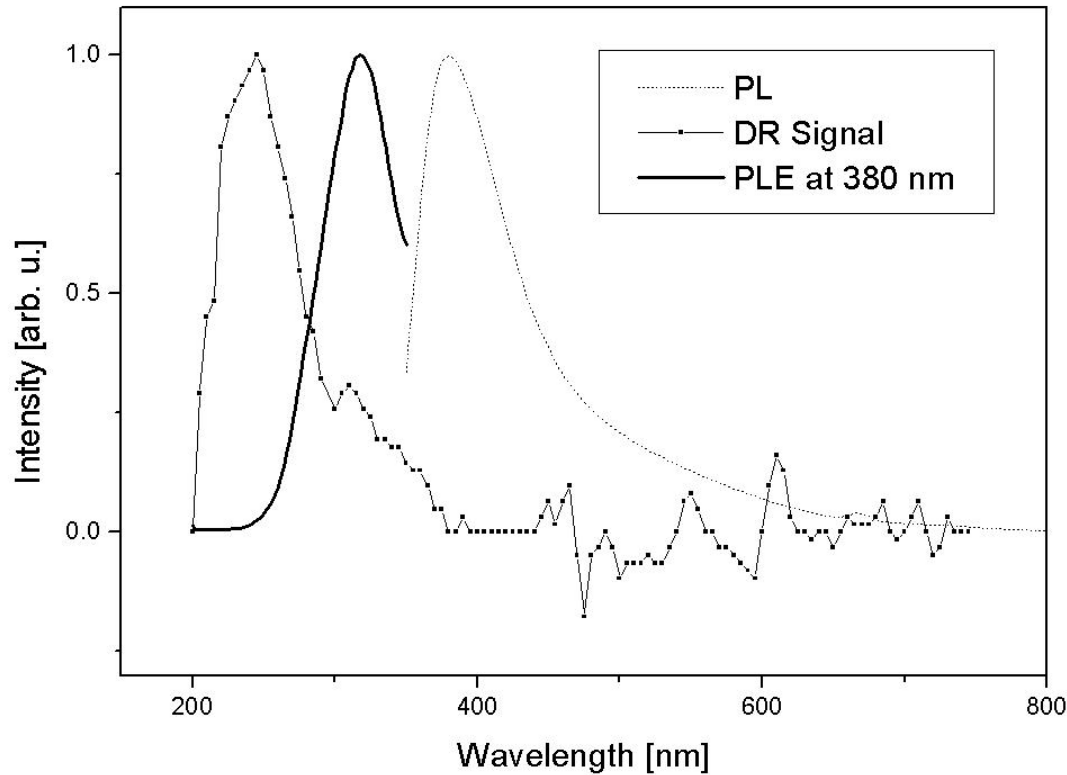


Figure 4-1. PLE, PL and DR (e.g., absorptivity, see Appendix A) characteristics of Sispark-processed in air.

The surface area of sp-Si constitutes mainly of a-SiO₂. However, there is a population of Si particles in the matrix of a-SiO₂ [3, 36]. *The emitting centers could be related to Si particles in a matrix of a-SiO₂.*

The optical absorption spectra of sp-Si processed in air and sp-Si processed in pure oxygen show similar bands between 200 and 300 nm. However in one of the cases (in pure O) the bands are resolved (Figure 4-2), while they are convoluted in the other case (in air). This fact suggests that *the light-absorbing centers in both materials might be related, but will have important differences.*

Research Procedure

Since sp-Si consists of a-SiO₂, a-Si, c-Si and Si nitrides/oxynitrides, the light-emitting centers will be modeled as

- Amorphous SiO₂ – based clusters with and without participation of N atoms;
- Amorphous Si – based clusters with and without participation of N atoms;
- Si nitride and oxynitride clusters;
- Clusters of the type a-SiO₂/a-SiN_xO_y or a-SiO₂/a-SiN_x;
- Clusters of the type a-SiN_xO_y/a-Si or a-SiN_x/a-Si;
- C-Si clusters will be included for completeness: a-SiN_xO_y/c-Si, a-SiN_x/c-Si;
- Clusters of the type a-SiO₂/a-Si and a-SiO₂/c-Si.

For all 7 families of molecular clusters the following procedure was applied:

- Without exception, the cluster geometries were based on previously published studies, showing sufficient experimental and/or theoretical support for their existence;
- Modification of the above geometries was done strictly following the rules of bonding for O, N, Si and H;
- All dangling bonds were terminated with H atoms;
- The structures of all clusters were optimized with AM1/PM3;
- ZINDO/S spectroscopic calculation was performed for all clusters, resulting in a calculated optical absorption spectrum;
- The calculated spectrum was compared with the spectrum of sp-Si.

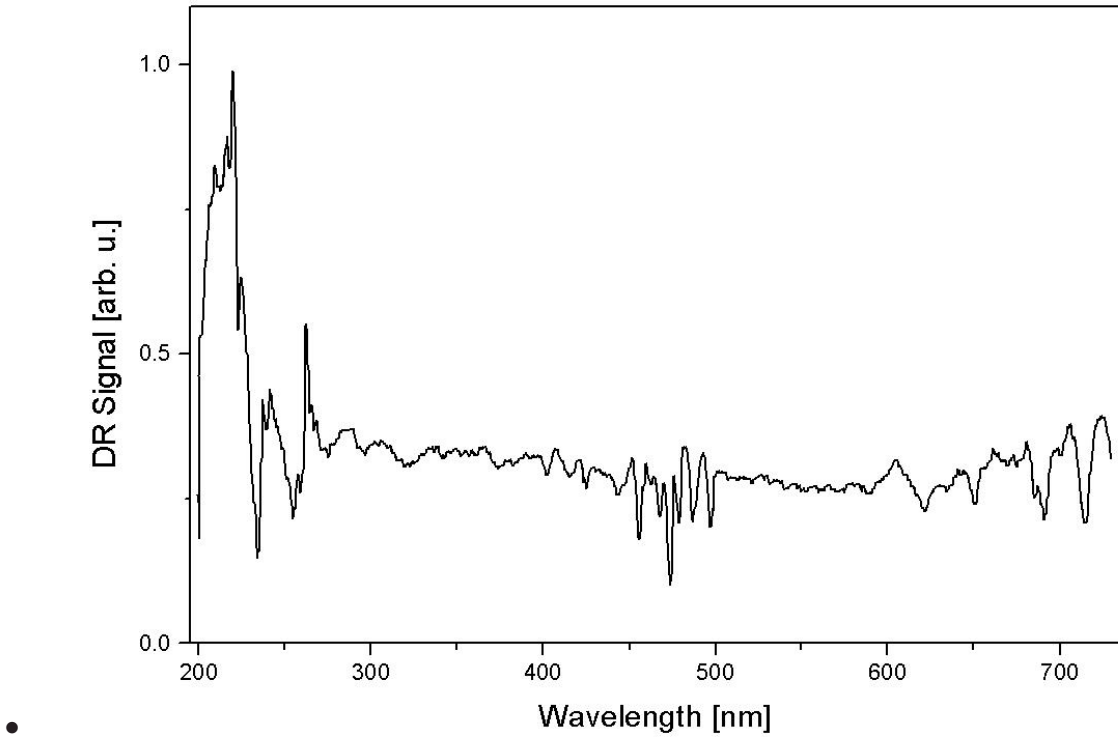


Figure 4-2. Differential reflectogram (e.g., absorption spectrum, see appendix A) of Silicon spark-processed in O atmosphere. The material does not show PL, when excited with a He-Cd laser (325 nm) [39].

Many of the studied complexes were tested for spin state contamination by projecting the molecular Slater-type wave function Ψ over wave functions, representing the pure multiplicities (the eigenfunctions of the spin operator S^2). In the case of Unrestricted Hartree-Fock (UHF) type of field, all molecules studied in this work satisfy the condition

$$\hat{S}^2 \Psi_{UHF} \approx \sigma \Psi_{UHF}, \quad (4-1)$$

where σ is a scalar quantity. Therefore, the clusters studied in the present work have been considered to have singlet ground states (closed shell configurations) and the Restricted Hartree-Fock (RHF) implementation of the INDO code was used.

The high temperature stability of the PL in sp-Si suggests the emitting centers occupy equilibrium molecular geometries, which excludes defects from consideration. Certain defects in the sp-Si bulk are responsible for its magnetic properties, which are annealed out at $\sim 600^{\circ}\text{C}$ [40], while the PL properties remain at this temperature. To add more weight to this argument, one can also point to the fact that N atoms in Si-rich silica are proven to improve the properties of the dielectric by reducing the density of charged and neutral defects [41 - 50] and at the same time it has been established that N is of key importance for the PL in sp-Si. Still, some high-strain structures and clusters with hypercoordinated atoms were included systematically in the calculations, but did not provide acceptable predictions of the properties of sp-Si.

The calculations with clusters from the various cluster families led to consecutive approximations to the spectrum of sp-Si with increasing accuracy. They are presented below in the order the original research was conducted.

Optical Properties of a-SiO₂ – based Clusters

Nearly 100 silica ring clusters (Fig. 4-3) were optimized with the AM1 and modified by substitution of O atoms with N atoms [25]. Various schemes of attachment of clusters were also applied with the goal to invoke a change in the optical properties of the resulting structure. After the geometry optimization, INDO/S spectroscopic calculations were performed for each individual cluster. The optical transitions of the majority of the studied clusters occur at energies, higher than 6.2 eV (lower than 200 nm). Some of the structures though, allow optical transitions that are in close resemblance of those in sp-Si. The two-member ring is a planar structure having two double bonds Si=O [15, 51 - 55]. The ring was modified by

- Substitution of an O atom with a N atom;

- Substitution of Si=O with Si-(NH₂);
- Replacing of all double bonds with single bonds, concomitant with the addition of a H atom.

If an N atom takes the place of an O atom and if a double bond Si=O is present then the resulting absorption spectra exhibit a single peak near 245 nm (5.05 eV, Fig. 4-4). If all of the O atoms in the cluster are substituted with N atoms, or no N atoms are present, the peak vanishes.

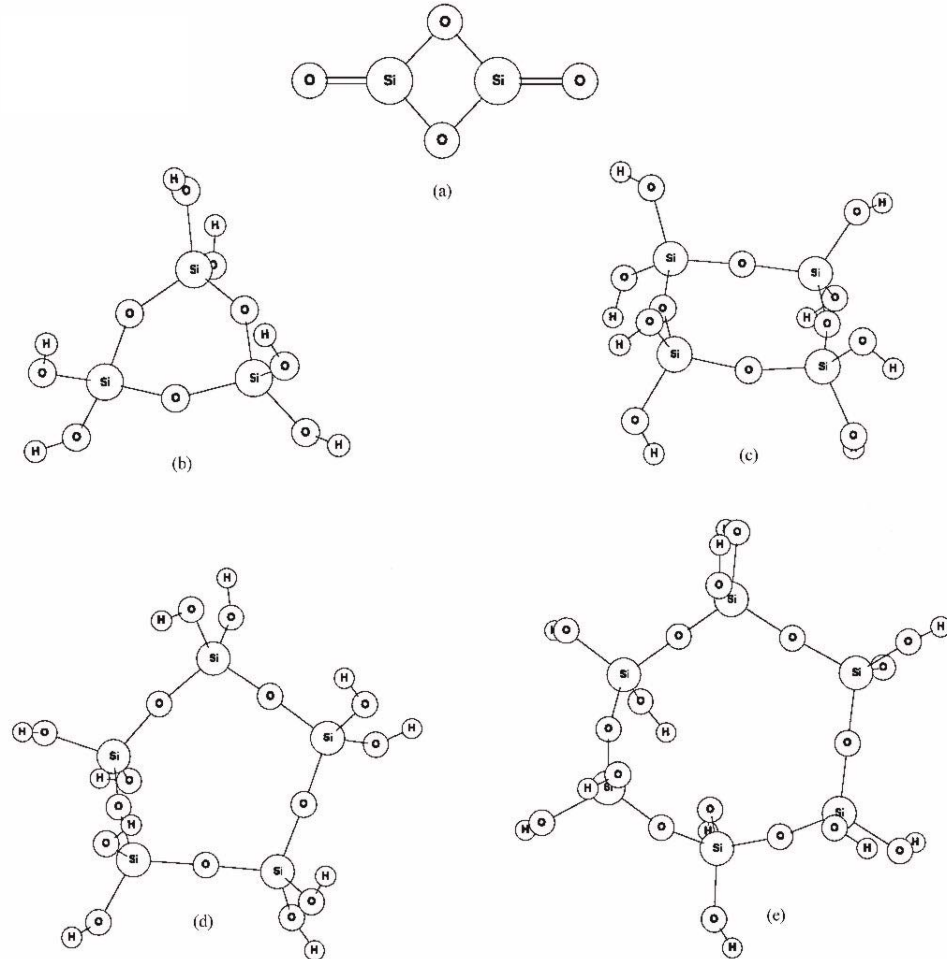


Figure 4-3. Silica ring-shaped clusters. (a) Two-member ring; (b) three-member ring; (c) four-member ring; (d) five-member ring and (e) six-member ring.

The three-, four-, five- and six-member silica rings are non-planar structures [56] that do not contain double bonds. Substitution of O atoms with N atoms does not result in absorption peaks that are close to those of sp-Si. However, attachment of a modified two-member ring may result in alteration of the optical properties. For instance, if a two-member ring is attached to a six-member ring, an electron transition near 245 nm (Fig. 4-5) emerges in its absorption spectrum. A similar trend can be observed for some clusters that are structured as a combination of an extended two-member ring and a six-member ring (Figs. 4-6 and 4-7).

Further understanding about the process of absorption can be obtained by considering some specific features of the molecular orbitals in a given cluster. In CI, the absorption spectrum is calculated from the transitions between CI vectors, which are mathematically represented by linear combinations of Slater-type determinantal wave functions. If a transition is possible for a pair of CI vectors, then the energy of the transition can be identified. The Tabulator program within the CAChe code [57] builds a three-dimensional coordinate grid and calculates at each point, the value of the electron probability amplitude for the HOMO and the LUMO. Electron isosurfaces are constructed, using all points, at which the above calculated amplitude is equal to 0.07 atomic units (a. u.). The occupied and unoccupied orbital surfaces are displayed in different colors.

Fig. 4-8 is a three-dimensional image of silicon oxynitride molecules and the orbital isosurfaces for the transition at 245 nm and its vicinity. Similar plots were done for structures with different sizes. If these exhibit an absorption peak near 245 nm, then always the HOMO and the LUMO at this excited configuration (which is, the electron

transition amplitude) are located over the small ring structures with participation of the oxygen atom in the Si=O bond.

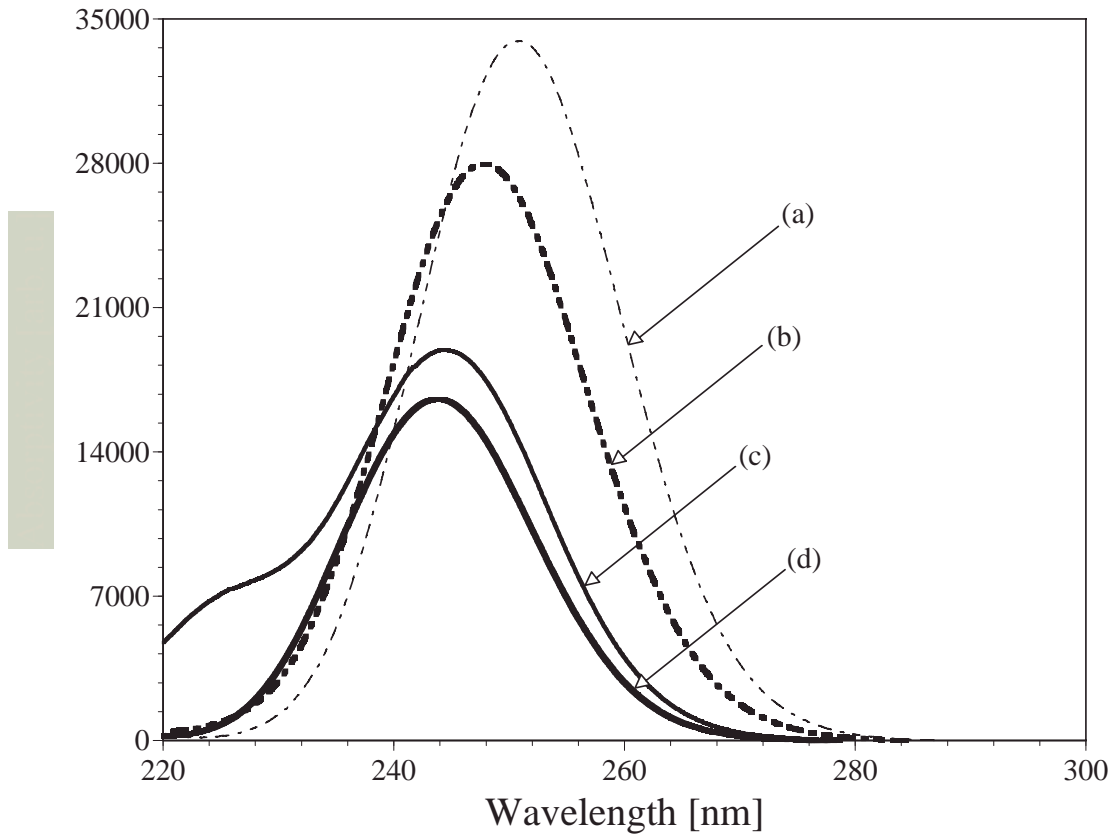
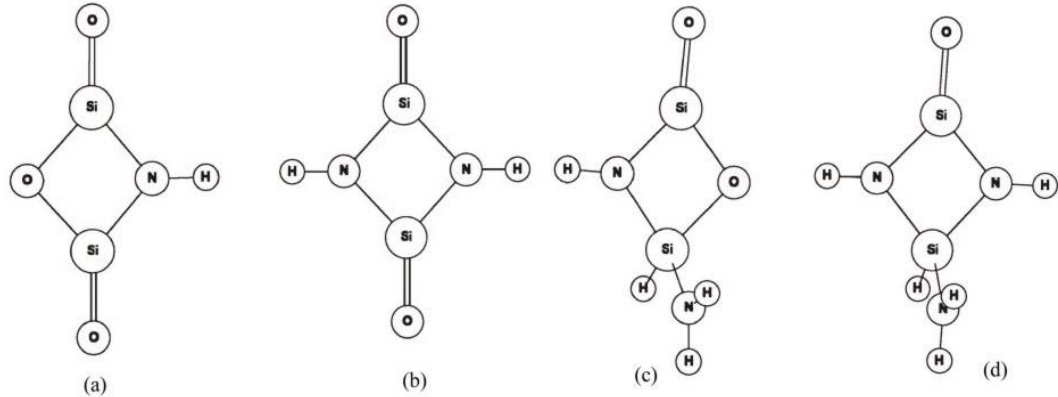


Figure 4-4. Equilibrium geometries and spectra of modified two-member silica ring clusters.

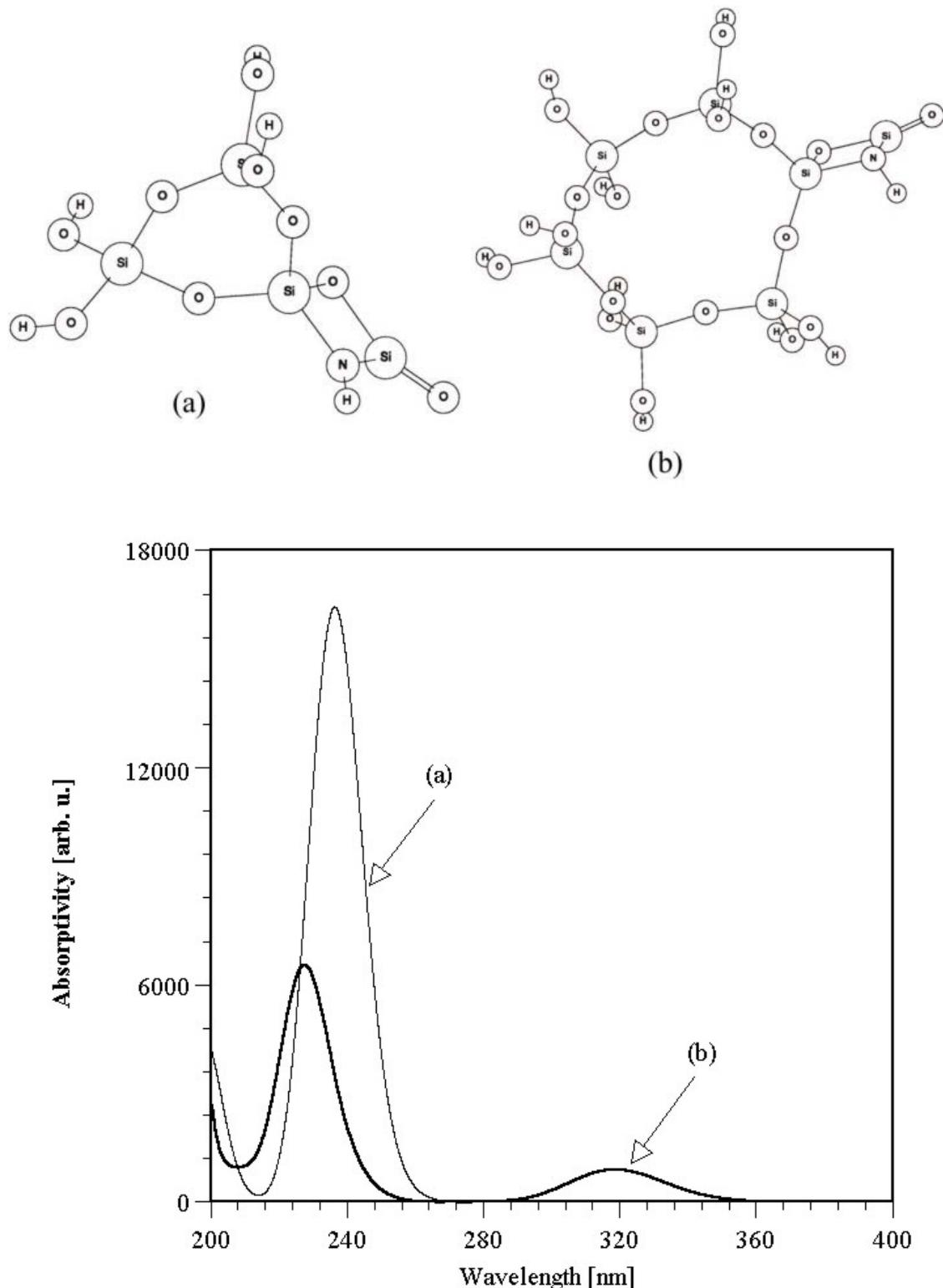


Figure 4-5. Equilibrium geometries and spectra of modified three- and six-member rings via attachment of two-member silica ring.

If the desired peaks were preserved in the spectra of the two-member rings only and nowhere else, then such structures cannot be used to model the properties of a real solid-state material. The above facts show, however, that it is possible to incorporate the strained two-member rings into larger structures and to impart their optical properties to the whole molecule. Thus, the size of the cluster can be increased without alteration of the desired properties.

However, the process of attachment does not always retain the transition of the small rings. As can be seen from the above results, modified two-member ring clusters turn out to be always inactive when attached to a four or five-member ring. This is also true in many cases where three- and six-member silica rings are attached. Mere substitution of O with N in the case of three-, four- and five-member silica ring-chains does not result in the alteration of optical properties either.

These observations demonstrate that there are many possibilities for incorporation of N atoms into amorphous SiO₂, but only a limited number of them will result in an optical excitation near 245 nm. The active centers are always dependent on the availability of a modified two-member silica ring and a double Si=O bond.

The process of sp-Si growth randomly incorporates N and O atoms into an inhomogeneous, disordered solid phase. It is virtually impossible to control the microstructure of the material during the spark processing. In this situation, the cluster structures that contain N atoms, will have dissimilar geometries accordingly. Thus, a large number of N atoms will participate in the composition of various clusters, not being able to contribute to the optical properties. A finite number of them are possible to take part in the formation of modified two-member silica rings. In certain cases, such

structures will invoke alteration of the optical properties of the material, lowering the optical absorption threshold energy to 5.05 eV, which corresponds to a wavelength of 245 nm.

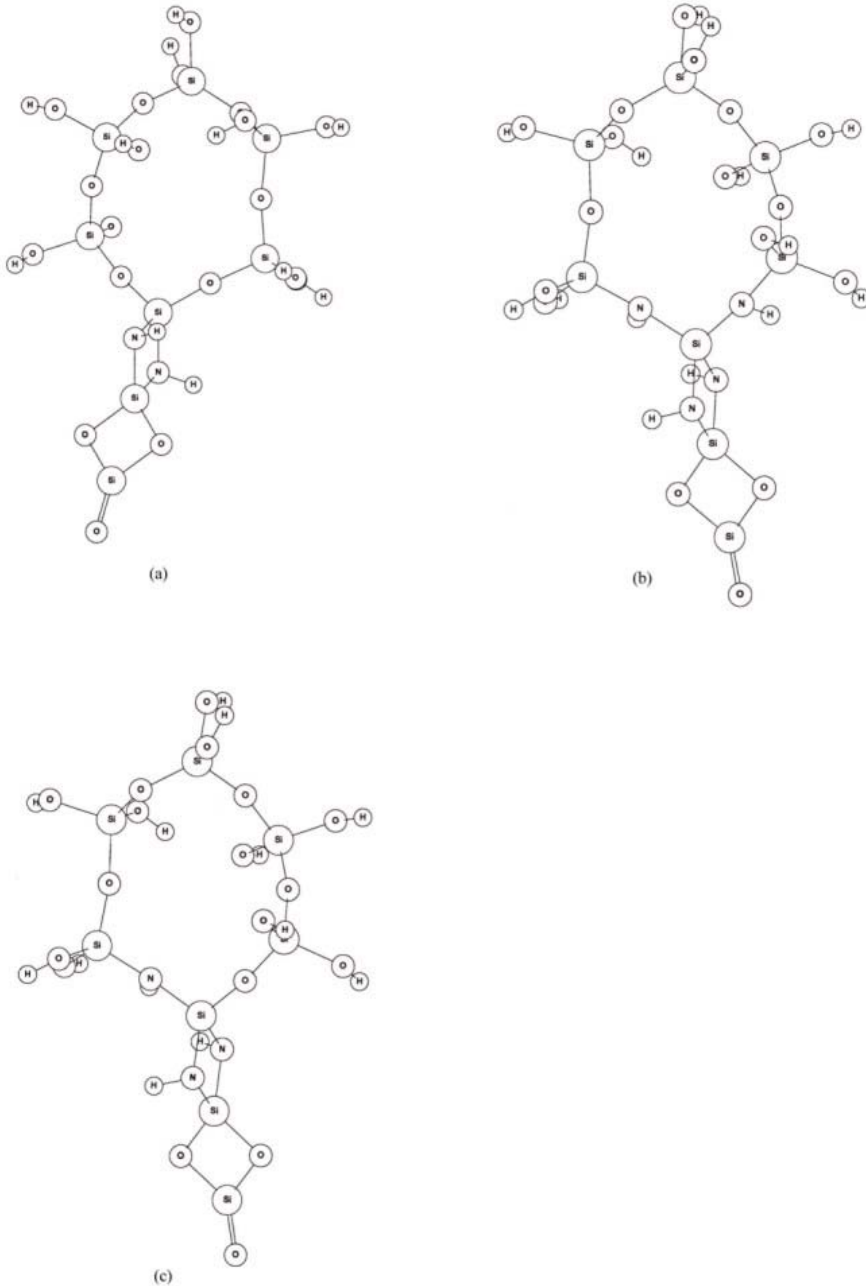


Figure 4-6. Attachment of two-member ring to six-member rings.

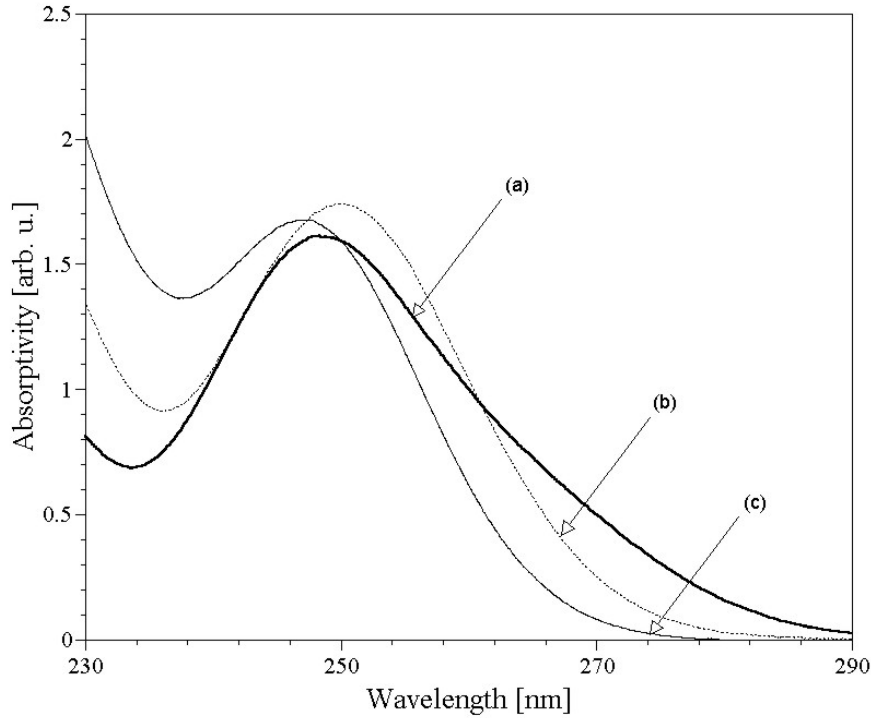


Figure 4-7. Calculated absorption spectra of modified six-member rings via attachment of two-member silica ring. (a), (b) and (c) correspond to the clusters on Figure 4-6 respectively.

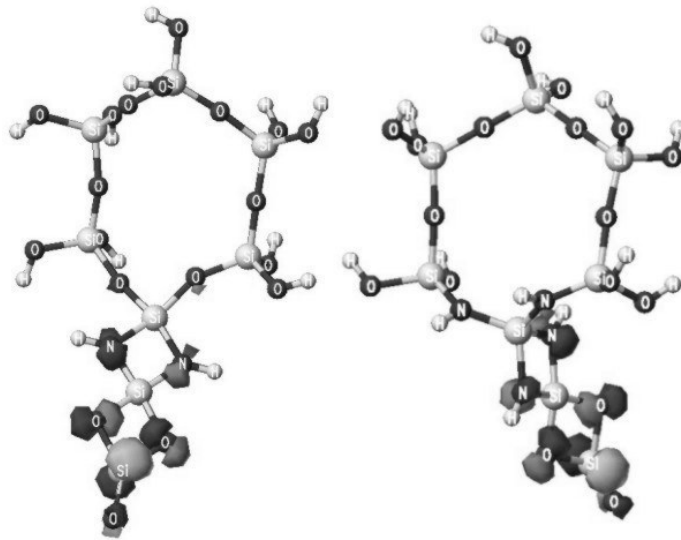


Figure 4-8. Three-dimensional molecular orbital surfaces, corresponding to the electron transition at 245 nm.

In summary, silica rings alone cannot account for the optical properties of sp-Si, since they reproduce only one peak of the sp-Si spectrum – the peak at 245 nm. However, by replacing O atoms by N, a remarkable alteration of the optical properties of certain two-, three- and six-member silica rings is observed. These results suggest that silica clusters are potential participants in the process of light emission of sp-Si.

Optical Properties of Silicon Rings

Si and SiO₂ clusters of different sizes and geometries participate in the plasma-assisted vaporization process during spark processing and in the luminescent material as well [3]. The ring-shaped clusters are an important subset of the large family of these clusters (Figure 4-9). There is a substantial number of computational studies on Si ring networks, publications on which can be traced back to 1974 [58 - 70]. These publications show that theoretical modeling of a-Si with network of three to eight-membered Si rings successfully predicts experimentally measured properties of material (e. g. radial distribution function in X-ray diffraction, density of states, infrared spectra etc.).

Therefore, there is theoretical support for the existence of Si rings, which are the building blocks of the random network of a-Si. Si rings have also been observed experimentally in a-Si and oxygenated Si rings have been observed at Si/SiO₂ interfaces [71 - 73]. It is therefore relevant to study the optical properties of Si ring-shaped clusters and how they compare with the measured optical spectra of sp-Si and similar Si-containing materials.

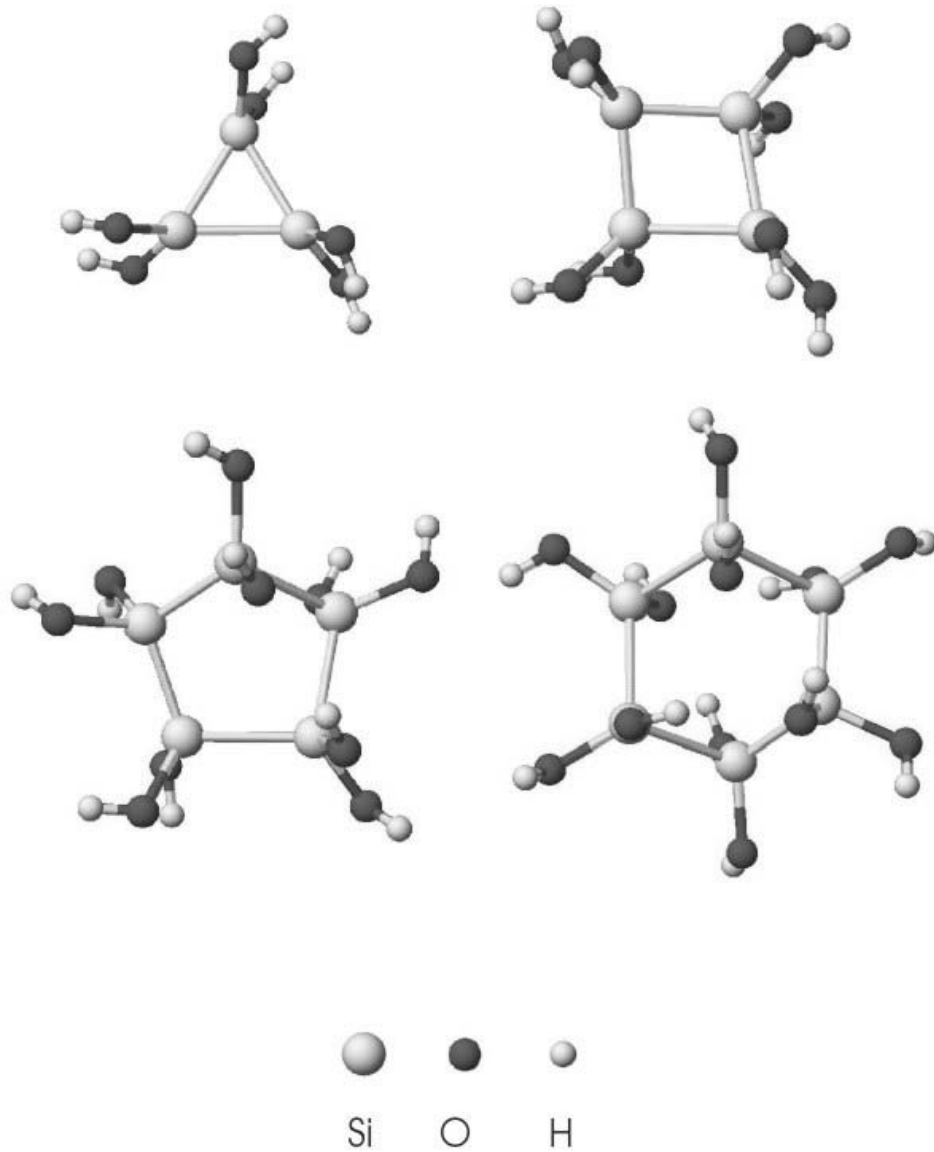


Figure 4-9. Optimized geometries of the OH-terminated Si rings.

Previously published quantum mechanical calculations indicate stable geometries of isolated three-, four-, five- and six-member Si ring-shaped clusters. At room temperature, they will normally react with oxygen, hydrogen or nitrogen. Our calculations indicate that this is energetically favorable. Table 4-1 contains data for the isolated three-member Si ring and shows the trend in energetics when the ring reacts with

oxygen and nitrogen. The same trend has been observed in the cases of four-, five- and six-member Si rings.

The AM1 semi-empirical calculations also reveal a definitive trend in the energetics of all studied Si rings, when a silica ring is attached to them. In all cases, an increase of the average atomization energy is observed when this type of attachment takes place. The results are shown in Table 4-2.

Another common trend in the behavior of all studied hydrogenated Si rings is observed when an O atom is substituted by an N atom. The average atomization energy $\langle E_a \rangle$ of such clusters decreases as the number of the substitute N atoms increase. However, if the heat of formation of the molecule is denoted as ΔH_f° , then the difference

$$|\Delta H_f^\circ(k) - \Delta H_f^\circ(\text{isolated } k\text{-member ring cluster})| \quad (4-2)$$

diminishes in all cases for $k = 3, 4, 5$ and 6 when a substitute N is present. In other words, it takes less energy to add the NH_2 group to an isolated Si ring, compared to adding an OH group. This fact is illustrated in Table 4-3, as well as in Table 4-1.

The optical absorption spectra of the Si ring-shaped clusters consistently show a number of distinctive features. All spectra exhibit three characteristic peaks, positioned

Table 4-1. The energetics of the three-member Si ring as calculated by the semi-empirical method AM1.

Compound	Calculated $\langle E_a \rangle$, eV	Calculated ΔH_f , kcal/mol
Isolated Si_3 ring	- 2.30	243.6
Hydrogenated Si_3 ring, Si_3H_6	- 3.20	49.1
$\text{Si}_3\text{H}_5(\text{OH})$	- 3.66	- 17.8
$\text{Si}_3\text{H}_4(\text{OH})_2$	- 4.06	- 90.2
$\text{Si}_3(\text{OH})_6$	- 5.07	- 365.2
$\text{Si}_3\text{H}_5(\text{NH}_2)$	- 3.63	22.7
$\text{Si}_3\text{H}_4(\text{NH}_2)_2$	- 3.94	- 7.0

Table 4-2. The energetics of the studied Si rings with attached four-member silica ring as calculated by the semi-empirical method AM1.

Compound	Calculated $\langle E_a \rangle$, eV	Calculated ΔH_f, kcal/mol
Oxygenated Si_3 ring, $Si_3(OH)_6$	- 5.07	- 365.2
Four member silica ring attached to Si_3 ring	- 5.40	- 508.4
Oxygenated Si_4 ring, $Si_4(OH)_8$	- 5.10	- 474.0
Four member silica ring attached to Si_4 ring	- 5.40	- 640.1
Oxygenated Si_5 ring, $Si_5(OH)_{10}$	- 5.10	- 603.9
Four member silica ring attached to Si_5 ring	- 5.33	- 769.1
Oxygenated Si_6 ring, $Si_6(OH)_{12}$	- 5.10	- 731.8
Four member silica ring attached to Si_6 ring	- 5.30	- 897.3

Table 4-3. The calculated energetics of the addition of NH_2 and OH groups to an isolated Si_5 ring cluster.

Compound	Calculated $\langle E_a \rangle$, eV	$\Delta H_f' - \Delta H_f(\text{isolated } Si_5 \text{ ring})$, kcal/mol
Oxygenated Si_5 ring, $Si_5(OH)_{10}$	- 5.10	924.4
$Si_5(NH_2)(OH)_9$	- 4.99	880.4
$Si_5(NH_2)_2(OH)_8$	- 4.93	837.4
$Si_5(NH_2)_3(OH)_7$	- 4.86	794.8
$Si_5(NH_2)_4(OH)_6$	- 4.81	751.2

between 200 nm and 350 nm. On average, the peak located in the neighborhood of 200 nm has the highest intensity, while the other two peaks at 260 nm and 320 nm have comparable magnitude and usually overlap. However, the peak at 260 nm could dominate in intensity mostly in the cases when larger clusters are studied. In many spectra, a low-intensity peak appears, positioned in the interval between 400 nm and 500 nm (Figures 4-10 and 4-11).

The substitution of an O atom by an N atom in a Si ring cluster does not substantially influence its optical properties. This has been the conclusion from a comparison of more than two hundred spectra of such clusters. Generally, the addition of an N atom causes a separation of the peaks at 260 nm and 320 nm, which may otherwise overlap.

The results in Table 4-2 indicate that the atomization energy $\langle E_a \rangle$ is further increased in magnitude when a silica ring is attached to the Si cluster. This increased stability suggests that Si ring-shaped clusters could be incorporated in an amorphous silica matrix without compromising the stability of the molecule. It should be noted however that this is a qualitative statement only, while the quantitative influence of $\Delta\langle E_a \rangle$ on the structural properties has not been studied.

The optical absorption spectra of the OH-terminated Si ring-shaped clusters consistently show three peaks in the neighborhood of 200, 260 and 320 nm (Figures 4-10 and 4-11). The attachment of small silica clusters does not change the optical properties. Unlike the case of a four-member strained silica clusters with double Si=O bond [25], substitution of an O atom with an N atom does not lead to alteration of the absorption spectra of oxygenated Si rings. Additionally, the oxygenated Si ring-shaped clusters exhibit a small peak in their absorption spectra, located between 400 and 500 nm. The presence or absence of N atoms in the cluster does not influence the peak position or its intensity. The positions of the peaks coincide with the positions of small peaks or shoulders in the spectrum of sp-Si. This fact suggests that Si rings could be contributing to the PL of sp-Si.

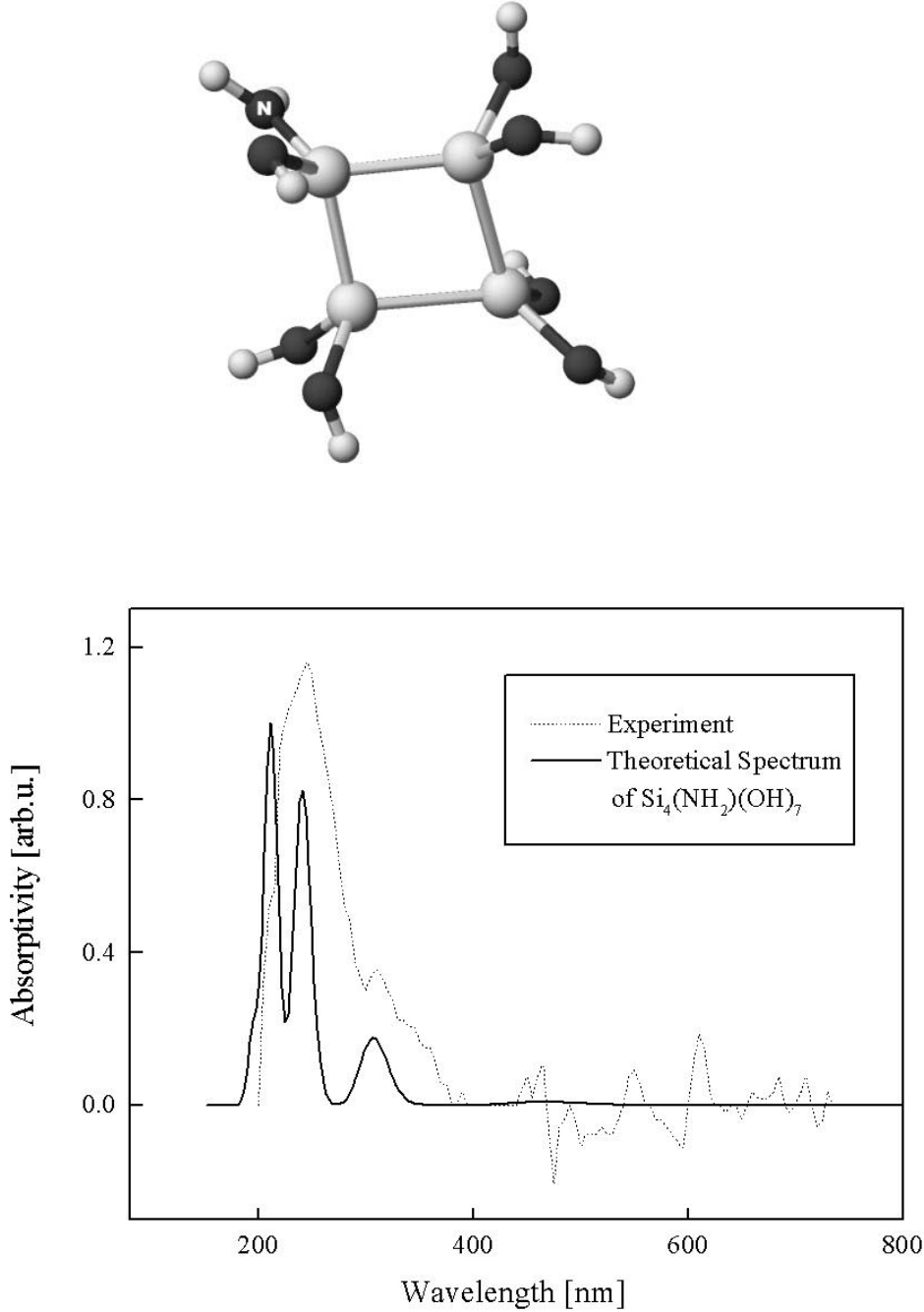


Figure 4-10. Comparison between an experimentally measured absorption spectrum of sp-Si (DR, see appendix A) and a calculated absorption spectrum of the oxygenated Si_4 ring $\text{Si}_4(\text{NH}_2)(\text{OH})_7$. The dark atoms represent O, the gray atoms represent Si, the small atoms represent H.

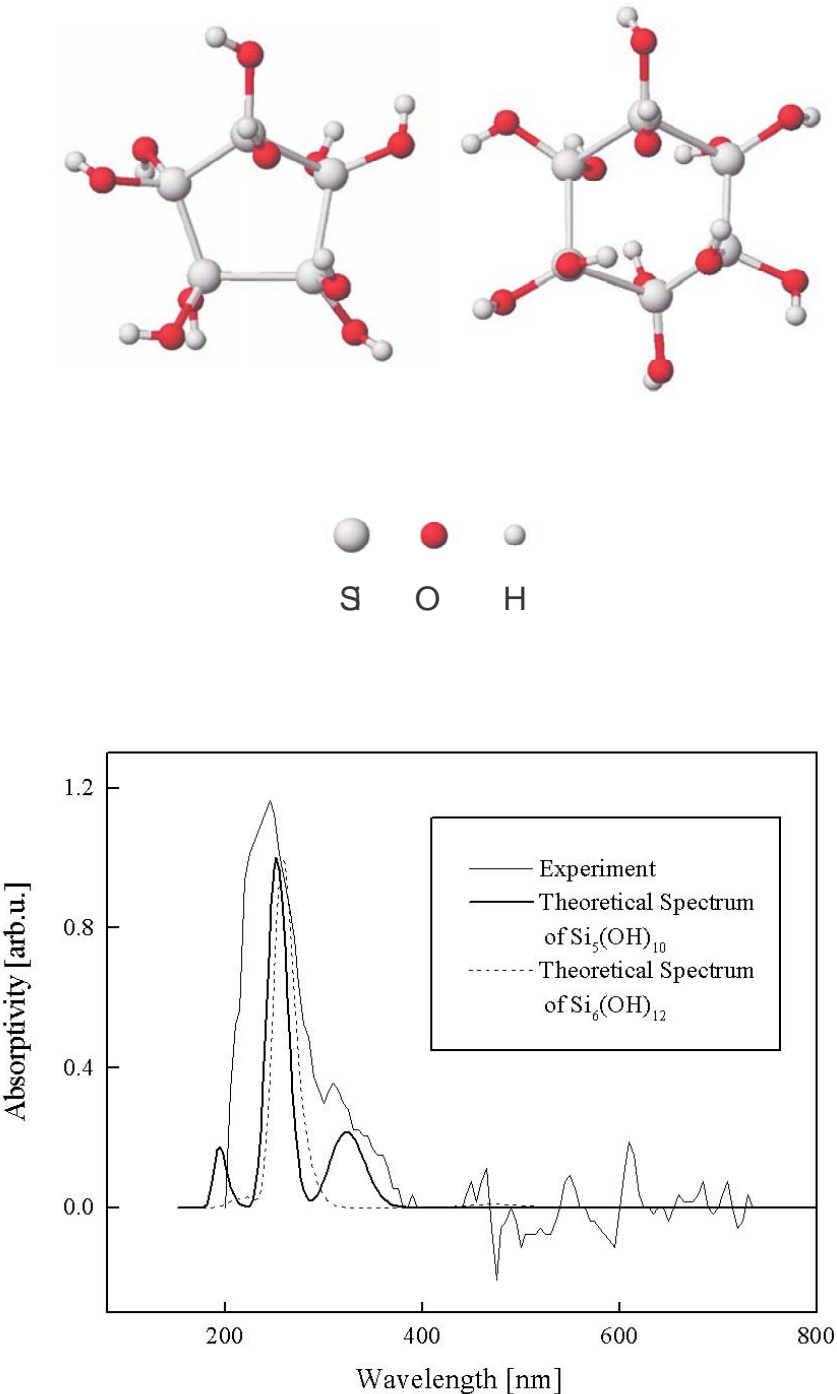


Figure 4-11. Comparison between an experimentally measured absorption spectrum of sp-Si (DR, see appendix A) and a calculated absorption spectrum of the oxygenated Si_5 and Si_6 ring-shaped clusters.

Optical Properties of Other Silicon Clusters

The Si ring-shaped clusters reproduce a number of features of the optical absorption spectrum of sp-Si. Compared to the spectra of silica clusters, they come much closer to the spectrum of sp-Si. Since this is a point of interest, the study of Si clusters was continued beyond the family of Si rings. The subject of the present section is focused on amorphous oxygenated Si clusters with 2 to 14 Si atoms.

The calculated spectra of oxygenated Si molecules are not applicable to sp-Si only; the optical characteristics of any Si- or silica-based light-emitting material can be compared to the results in this dissertation. The clusters in this work can be related to oxygenated, amorphous Si particles on the surface of materials, or in the bulk when amorphous Si particles are buried in amorphous silica, or can represent Si particles, nucleating in the gas phase in the presence of oxygen during laser ablation of Si or related growth processes of Si-based materials from the gas phase.

All molecular structures in this section are based on previously published geometries of isolated Si clusters, optimized with *ab initio* and DFT calculations and widely accepted as stable [12, 74 – 79]. In the sp-Si material, Si clusters do not exist as isolated molecules, but are rather bonded to oxygen and nitrogen atoms or to crystalline Si particles. We have studied the energetics of addition of the NH₂ and OH groups to the Si clusters. Figures 4-12 and 4-13 display the geometries of certain representative molecules - Si₃, Si₈, Si₁₀, Si₁₁ and Si₁₄. Table 4-4 contains data for the energetics of Si₃. The modulus of the average atomization energy $\langle E_a \rangle$ in the general case increases with the hydrogenation and always increases with OH-termination of an isolated Si cluster. It reaches its highest values when N atoms are absent. All of the studied structures in this work conform to this rule. Identical results have been achieved for a large variety of Si

ring-shaped clusters [80]. Therefore, the conclusion is imposed that in Si-based molecules the attachment of (OH) groups leads to structural stabilization which is most pronounced in the absence of (NH₂) groups. It should be noted however that this is a qualitative statement only, while the quantitative influence of $\Delta\langle E_a \rangle$ on the structural properties has not been studied.

Figure 4-14 displays calculated spectra of representative oxygenated Si molecules. The spectra always exhibit a triple-peak feature at or around 205 nm, 250 nm and 320 nm. The variation of the peak positions is within ± 5 nm for the first peak, within ± 20 nm for the middle peak and within ± 30 nm for the peak at 320 nm. Almost without exception, a weaker peak between 400 nm and 500 nm is also observed. In the general case the three peaks between 200 and 320 nm are resolved and still cannot reproduce a dominant peak at 250 nm, as it is in the spectrum of sp-Si.

The behavior of the triple peak is explained by the following:

Presence of N atoms in the molecule: If an OH group in an oxygenated Si cluster is replaced with a NH₂ group, this invokes small changes in the optical spectrum, which do not seem to follow a specific trend. In the majority of cases, upon such changes the agreement between the calculated spectrum of the cluster and the observed spectrum of sp-Si does not improve. The spectra of oxygenated Si molecules are far closer to the spectrum of sp-Si, when compared to spectra of SiO₂-based molecules and spectra of Si nitrides. This conclusion is based on comparison between more than one hundred silica and more than three hundred Si-based structures. Thus, the absorption of light in sp-Si is highly dependent on Si molecules rather than atomic impurities in the amorphous SiO₂ network. The study of the electronic transition amplitudes for the calculated high-

intensity transitions points towards Si particles within the amorphous SiO_2 as responsible for the light absorption of sp-Si.

Table 4-4. Energetics of the addition of the (OH) and (NH_2)₂ groups to Si_3 . The left column shows the values of the average atomization energy in eV.

Compound	Calculated $\langle E_a \rangle$, eV
Isolated Si_3 molecule	- 2.62
Hydrogenated Si_3 molecule, Si_3H_8	- 3.10
Oxygenated Si_3 molecule, $\text{Si}_3(\text{OH})_8$	- 5.18
$\text{Si}_3(\text{NH}_2)(\text{OH})_7$	- 5.10
$\text{Si}_3(\text{NH}_2)_2(\text{OH})_6$	- 4.96
$\text{Si}_3(\text{NH}_2)_3(\text{OH})_5$	- 4.90
$\text{Si}_3(\text{NH}_2)_4(\text{OH})_4$	- 4.81

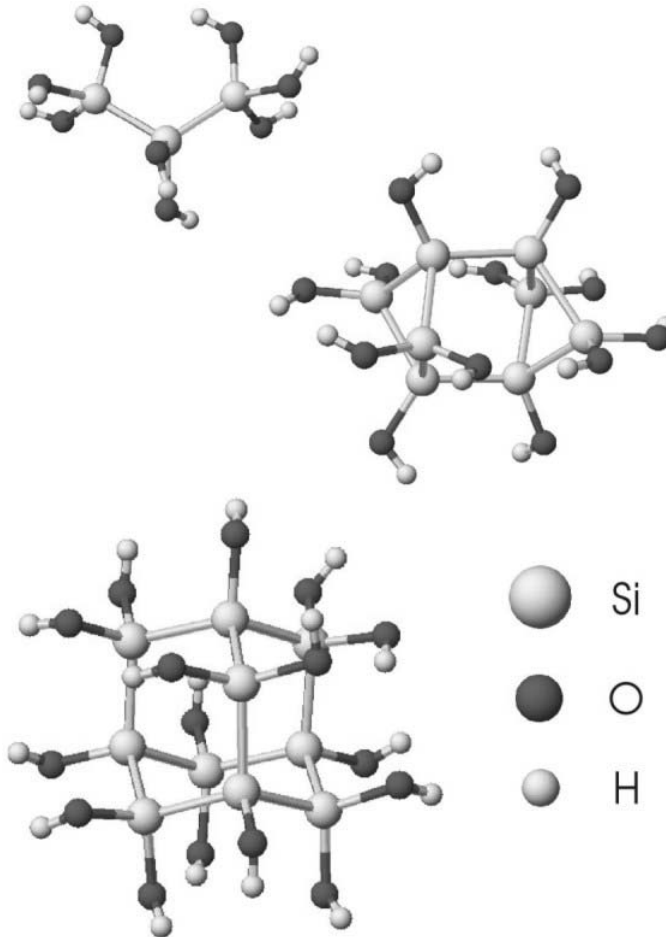


Figure 4-12. Geometries of OH-terminated Si_3 , Si_8 and Si_{10} molecules.

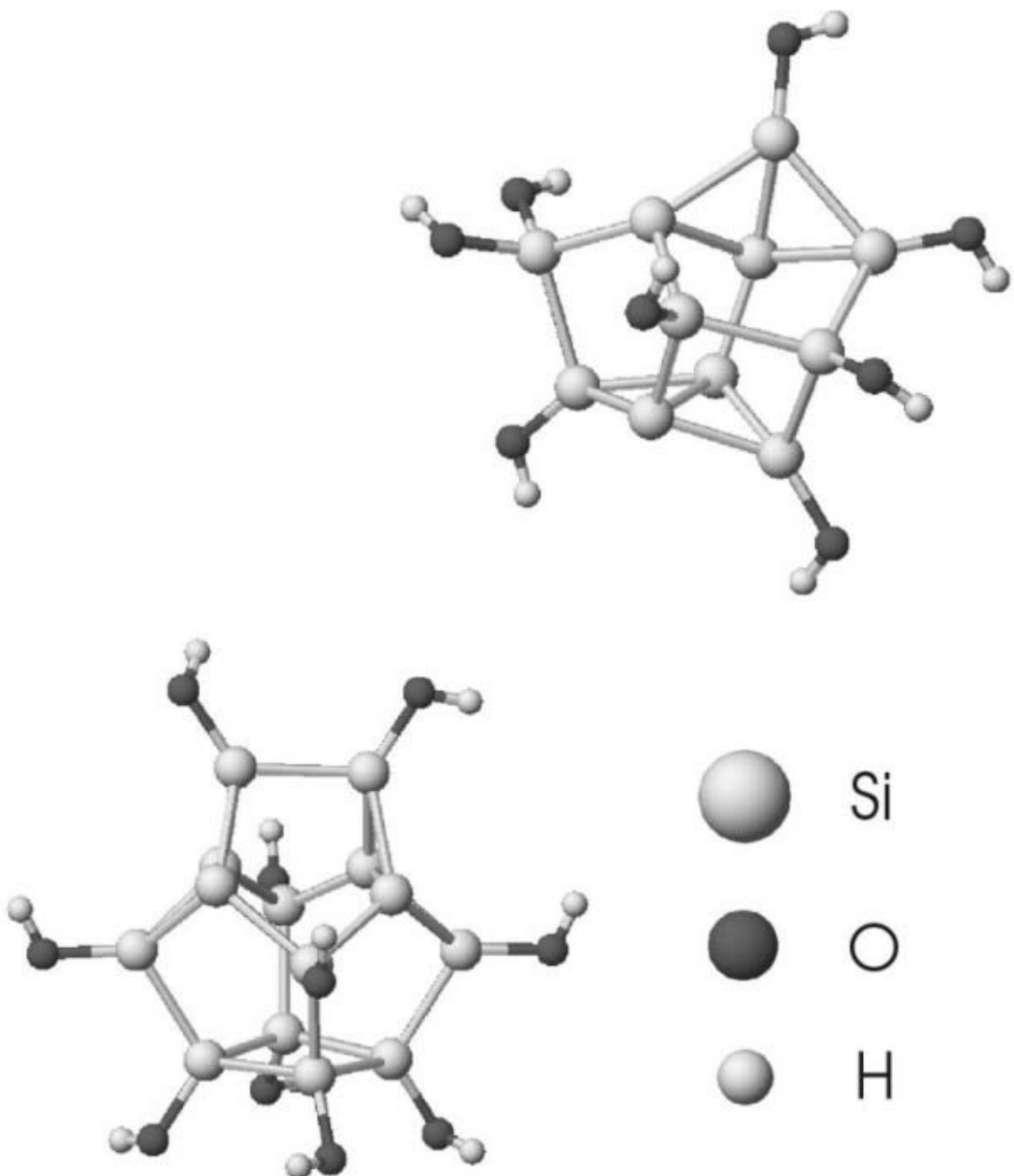


Figure 4-13. Geometries of the cage-shaped oxygenated Si_{11} and Si_{14} molecules.

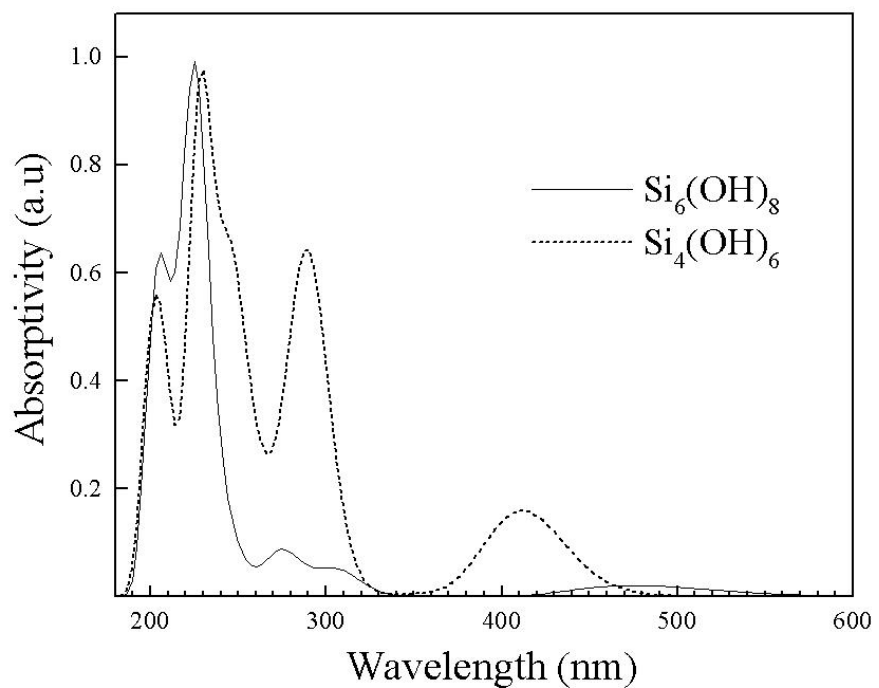
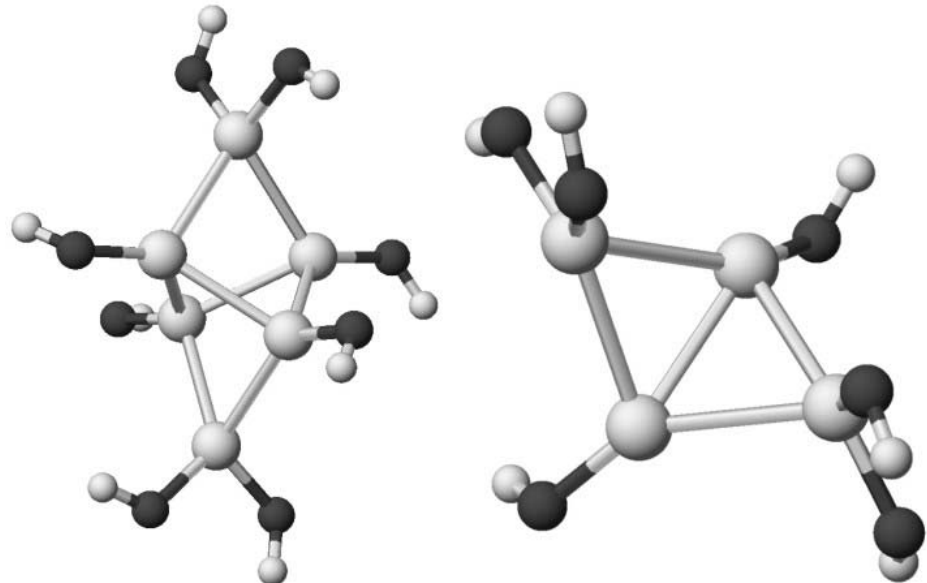


Figure 4-14. Calculated spectra of oxygenated Si_4 and Si_6 molecules. The dark atoms represent O, the gray atoms represent Si, the small atoms represent H.

- ***The role of the Si atoms:*** We have calculated the spectra of hydrogenated $\text{Si}_2 - \text{Si}_{14}$. Interestingly, the triple-peak feature of the spectrum is preserved in most of these cases. The peak at 205 nm is very strong, while the other two peaks overlap. The low-energy peak at 400 nm is absent in the spectra of small, hydrogenated Si molecules and reappears in the spectra of the larger ones (Si_{10} and up), together with neighboring smaller peaks. Despite that hydrogenated Si clusters are most probably not present in sp-Si, the specific features of their spectra suggest that the absorption of light in hydrogenated and oxygenated Si molecules occurs mainly over the Si atoms, while the H, O and participating N atoms have minor role, which could be related to a possible light emission in such molecules.

Within the set of calculated spectra of oxygenated Si clusters studied in this work, we have obtained a limited number of optical absorption curves, which show close agreement with the observed spectrum of sp-Si. Representative cage-shaped cluster structures associated with these spectra are shown on Figure 4-13, while Figure 4-15 displays a comparison between the calculated and observed absorption. These clusters have optical properties, which differ from the general trend of behavior of the studied oxygenated Si molecules, by exhibiting a large peak centered near 250 nm and reproducing the low-energy peaks of sp-Si between 500 and 700 nm.

Since sp-Si is inhomogeneous and amorphous, a small number of molecular structures, however close they may match the spectrum of sp-Si, cannot be expected to account for the properties of the material. This would be a deterministic approach, which disagrees with the random nature of sp-Si. Rather, a family of stable clusters with matching optical properties must be responsible for the PL of this material. Nevertheless, the achieved higher level of agreement with the observed spectra of sp-Si at this stage indicates that the present study has proceeded in the correct direction.

Optical Properties of Silicon Particles in an Amorphous SiO_xN_y matrix

As a next step, Si particles in an a- SiO_xN_y matrix were studied. In this case the calculated absorption spectra remarkably well reproduced the spectrum of sp-Si. Si cages

and clusters were modeled as bonded to silica rings. The agreement between theoretical prediction and experiment was achieved for any Si cluster, bonded to silica rings. The degree of similarity between calculated and measured spectra varies for the different Si particles, but the spectral features are similar (Figures 4-16 to Figure 4 - 25).

Our calculations suggest, that the Si particles in a-SiO_xN_y play a key role in the process of light absorption in sp-Si. Time-resolved PL measurements with sp-Si have shown PL decay times in the order of nanoseconds or even picoseconds [6]. This fact indicates that charge- or energy transfer mechanisms are unlikely prior to light emission in sp-Si, since such processes result in increased decay PL times. Photoluminescence Excitation (PLE) and optical absorption spectra of the material show identical peaks (Figure 4-1). This can be interpreted to mean that absorption is followed by emission on the same center.

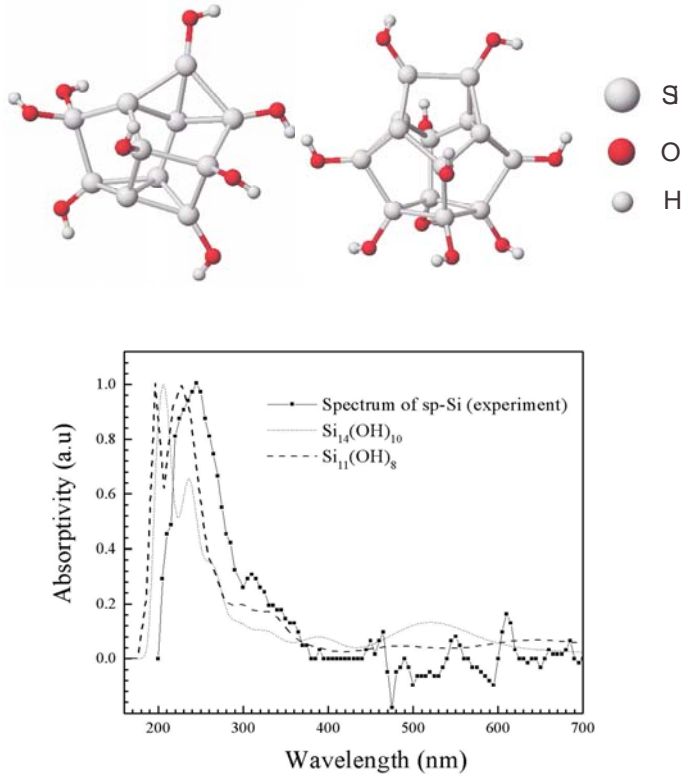


Figure 4-15. Calculated spectra of oxygenated Si_{11} and Si_{14} molecules.

The PLE spectrum shows that absorption around 320 nm most effectively results in emission of photons with a wavelength of 380 nm. The absorption at 245 nm is very high, but less efficient in producing blue emission. Still, laser excitation at 230 nm and lower energies results in emission of blue light [81]. At these wavelengths, the PLE exhibits a non-zero tail (Figure 4-1), consistent with the absorption measurements. It is therefore proposed, that both the absorption and emission of light in sp-Si occur over the Si particles, embedded in the amorphous insulator matrix of sp-Si.

The Role of N in the Optical Properties of Spark-processed Silicon

In the conducted experiments, the PL of sp-Si was excited by a He-Cd laser (325 nm). It is important to note that PL was observed only for sp-Si, processed in mixtures of O and N gases (e. g. air). Firstly, the He-Cd laser was not able to excite sp-Si, processed in pure O atmosphere, which suggests that such material either does not have an absorption band at the excitation wavelength, or the excited electrons lose energy along non-radiative pathways. Secondly, the absorption spectrum of sp-Si processed in air is different compared to the spectrum of sp-Si, processed in pure O atmospheres. For these reasons it has been inferred, that N plays a role in the optical properties of light-emitting sp-Si. A large number of studies consistently shows that in a-SiO_xN_y systems the N atoms pile up at the dielectric/Si interface [42, 44, 45, 47, 48, 82 - 91]. It has been suggested that in such situations, Si₂ – N – O bonding occurs at the interface [89, 90]. The application of these facts to our calculations has resulted in structures of the type, shown in Figures 4-19 to 4-24. Figures 4-16 to 4-18 and Figure 4-25 show good agreement as well.

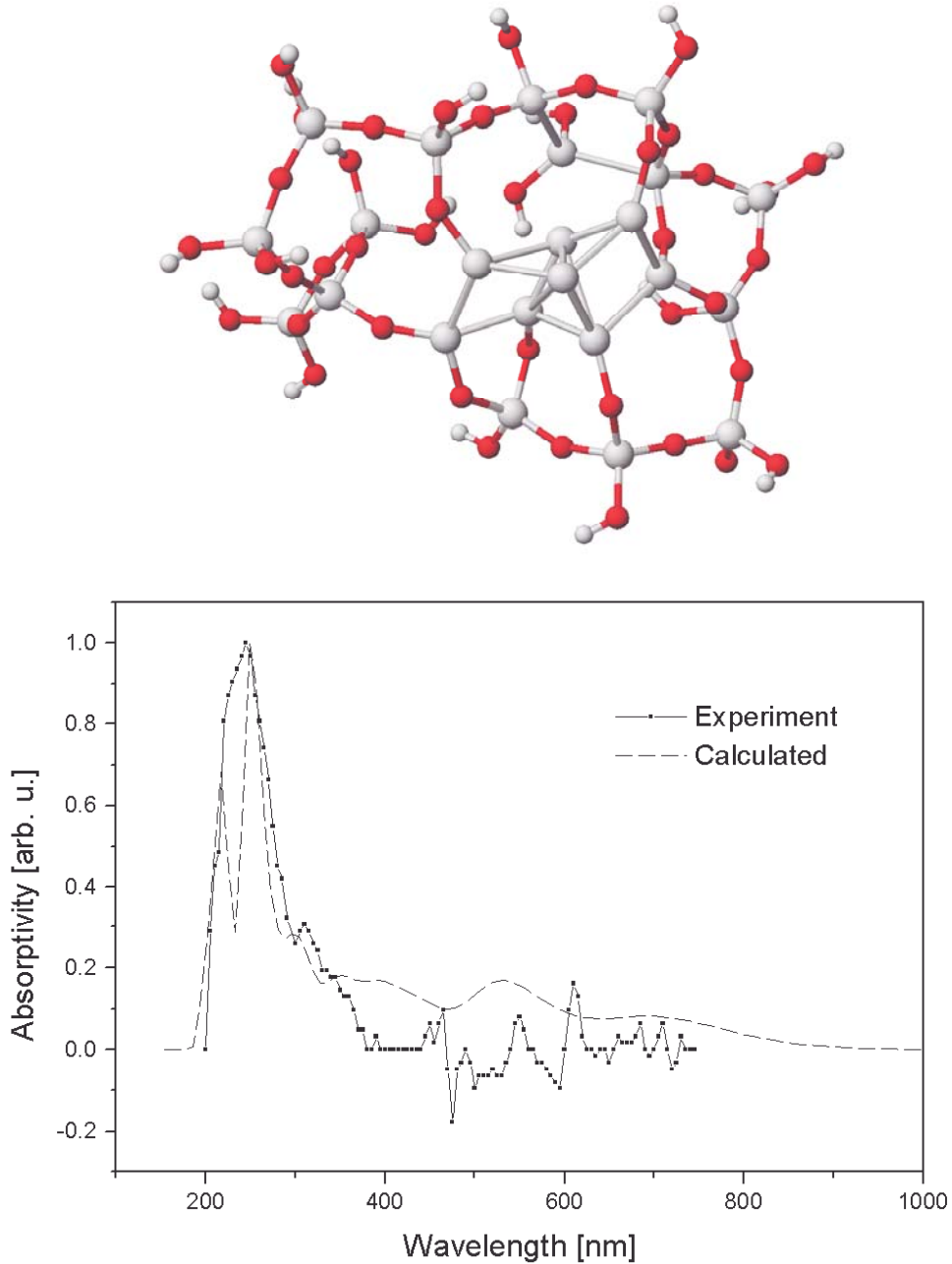


Figure 4-16. Si particle in amorphous silica matrix. The graph displays a comparison between the measured DR spectrum of sp- Si (appendix A) and the calculated spectrum of the cluster. The dark atoms represent O, the gray atoms represent Si, the small atoms represent H.

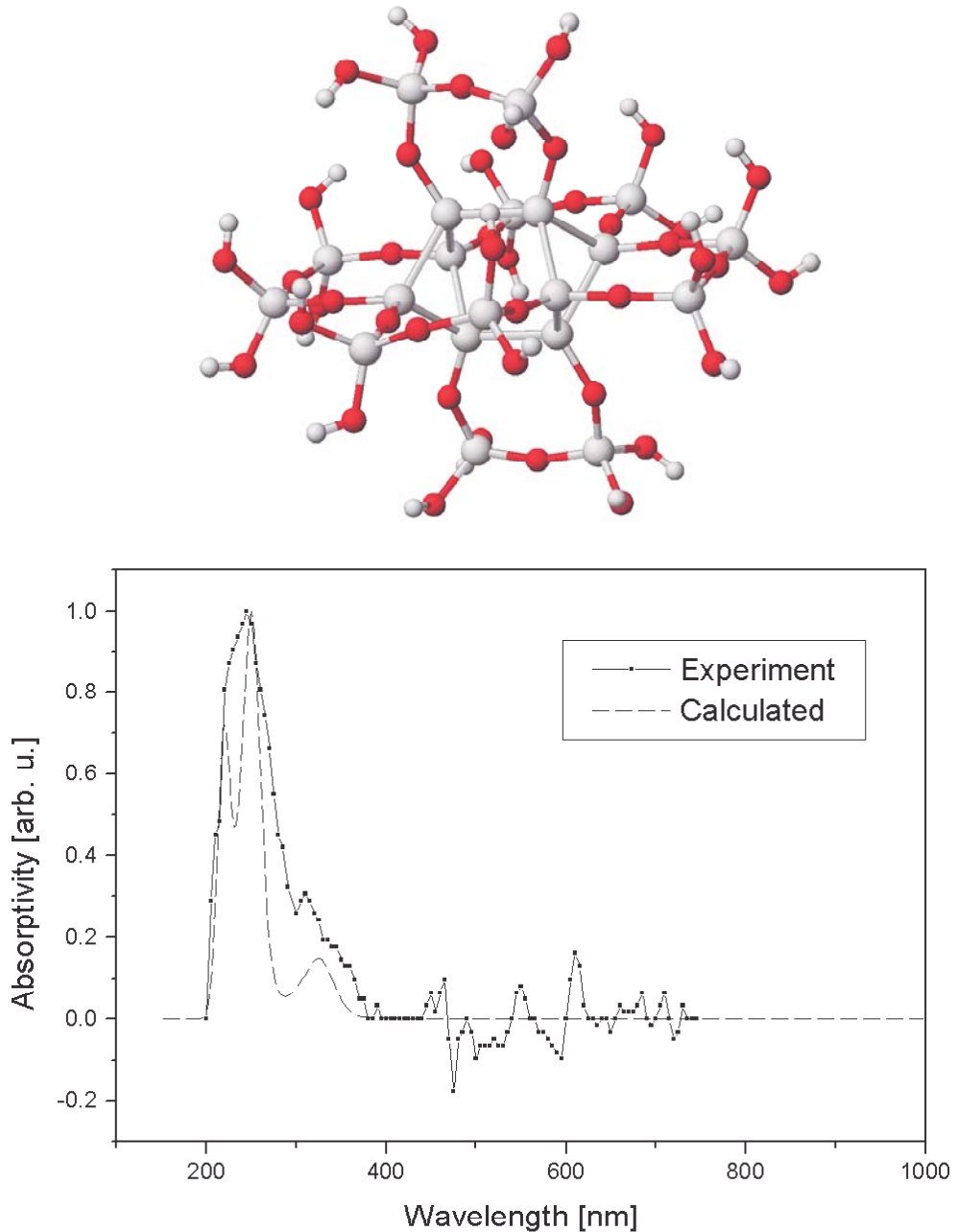


Figure 4-17. Si particle in amorphous silica matrix. The graph displays a comparison between the measured DR spectrum of sp- Si (appendix A) and the calculated spectrum of the cluster. The dark atoms represent O, the gray atoms represent Si, the small atoms represent H.

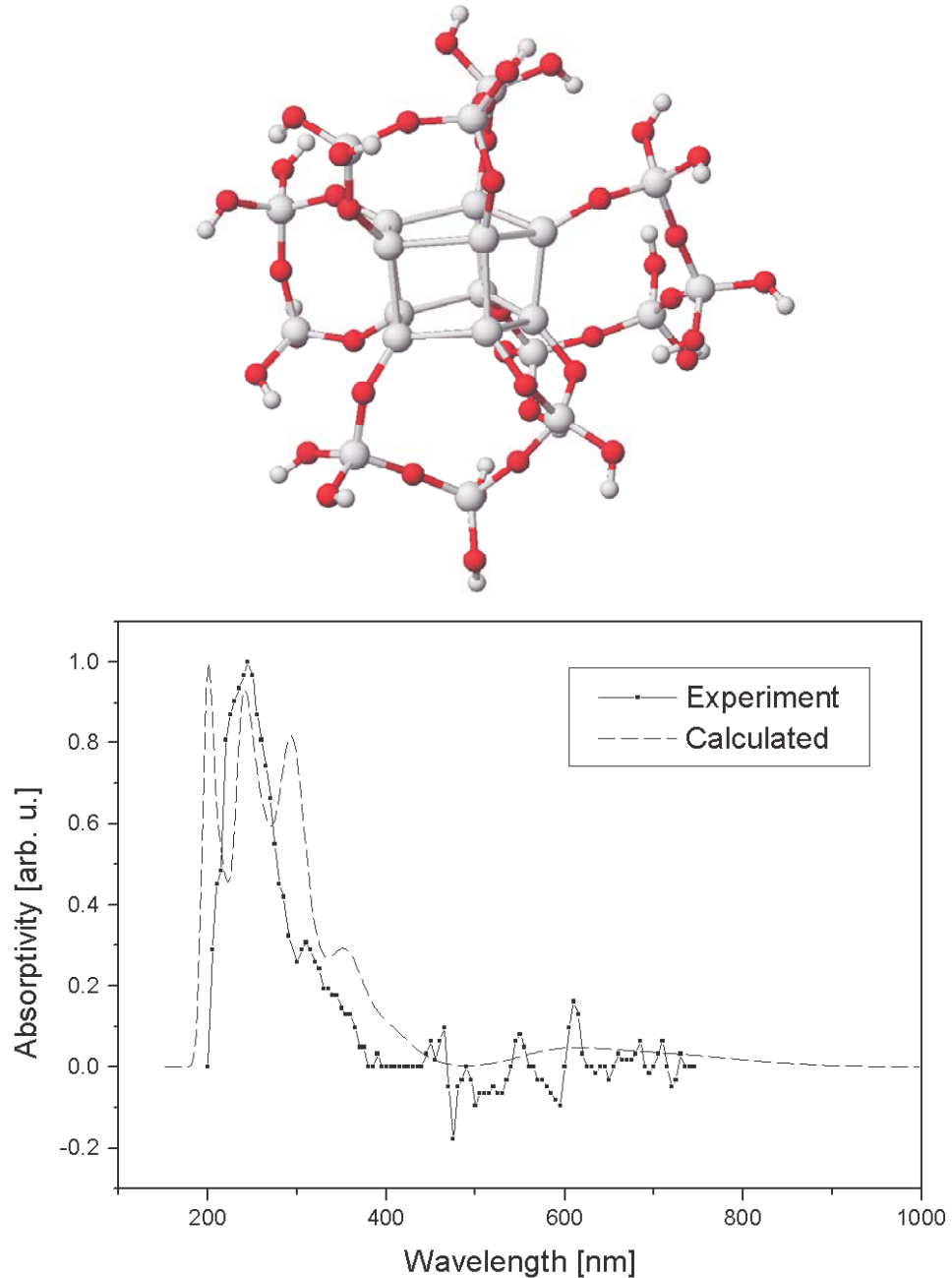


Figure 4-18. Si particle in amorphous silica matrix. The graph displays a comparison between the measured DR spectrum of sp- Si (appendix A) and the calculated spectrum of the cluster. The dark atoms represent O, the gray atoms represent Si, the small atoms represent H.

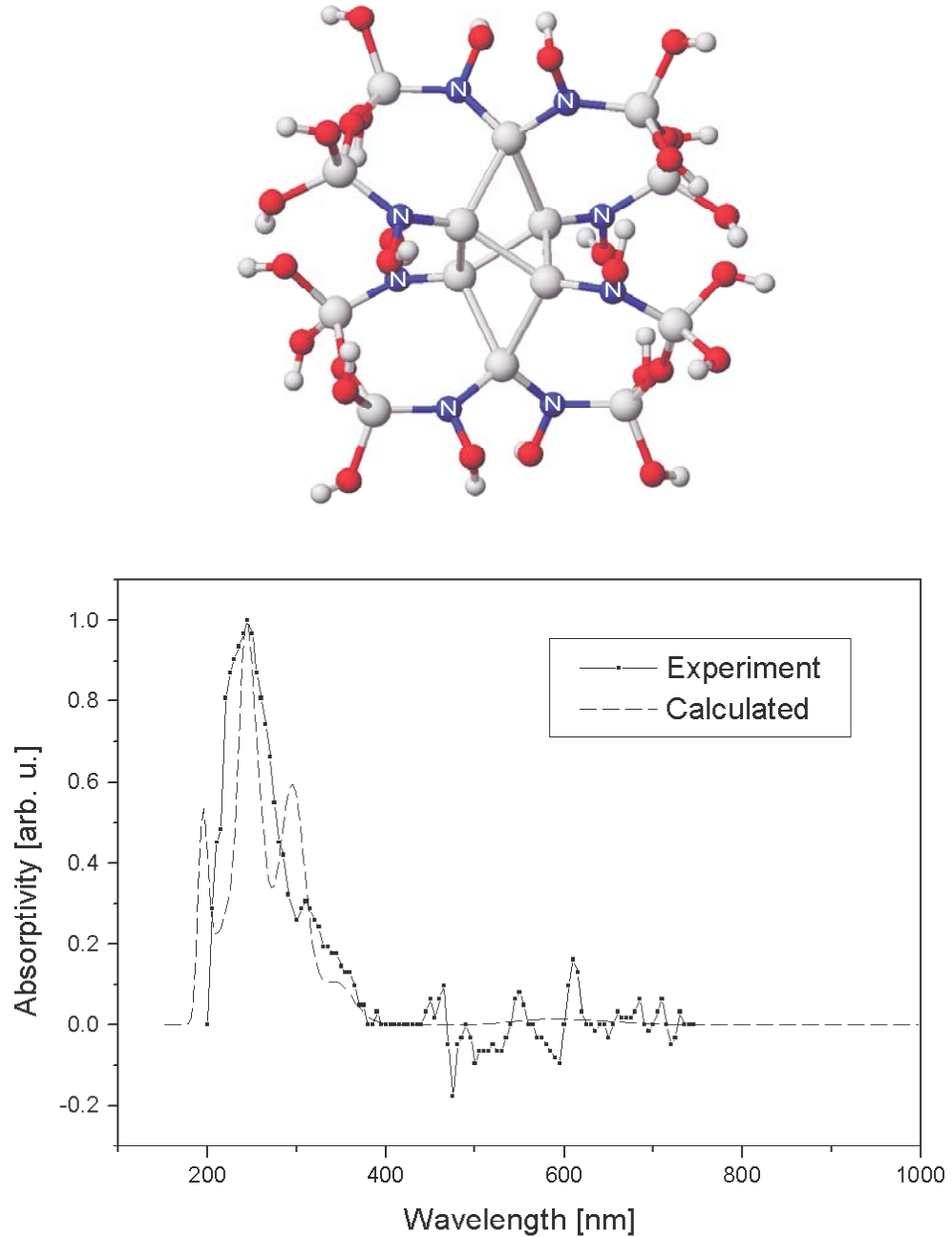


Figure 4-19. Si particle in amorphous silica matrix. The graph displays a comparison between the measured DR spectrum of sp- Si (appendix A) and the calculated spectrum of the cluster. The dark atoms represent O, the gray atoms represent Si, the small atoms represent H.

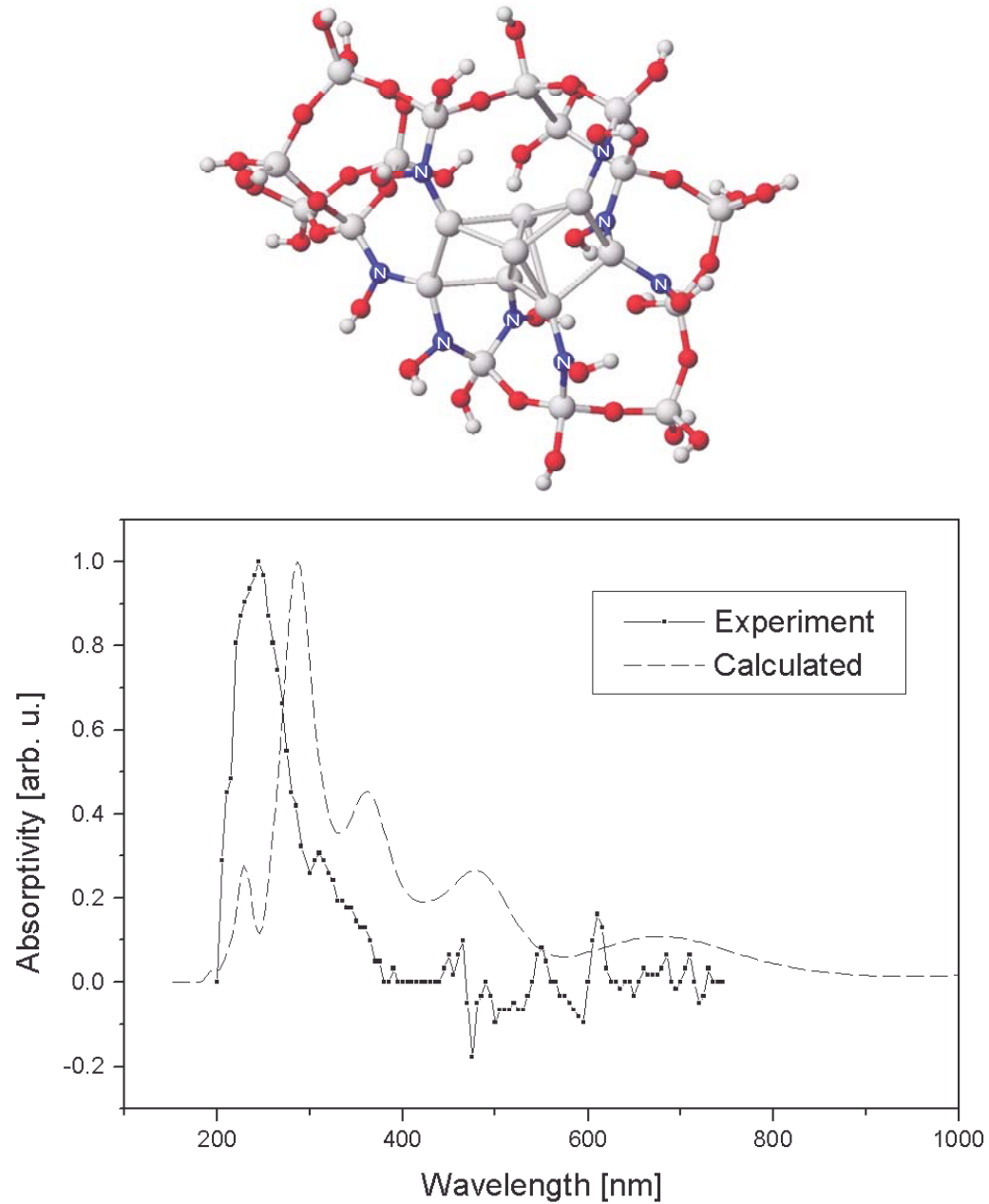


Figure 4-20. Si particle in amorphous silica matrix. The graph displays a comparison between the measured DR spectrum of sp-Si (appendix A) and the calculated spectrum of the cluster. The dark atoms represent O, the gray atoms represent Si, the small atoms represent H.

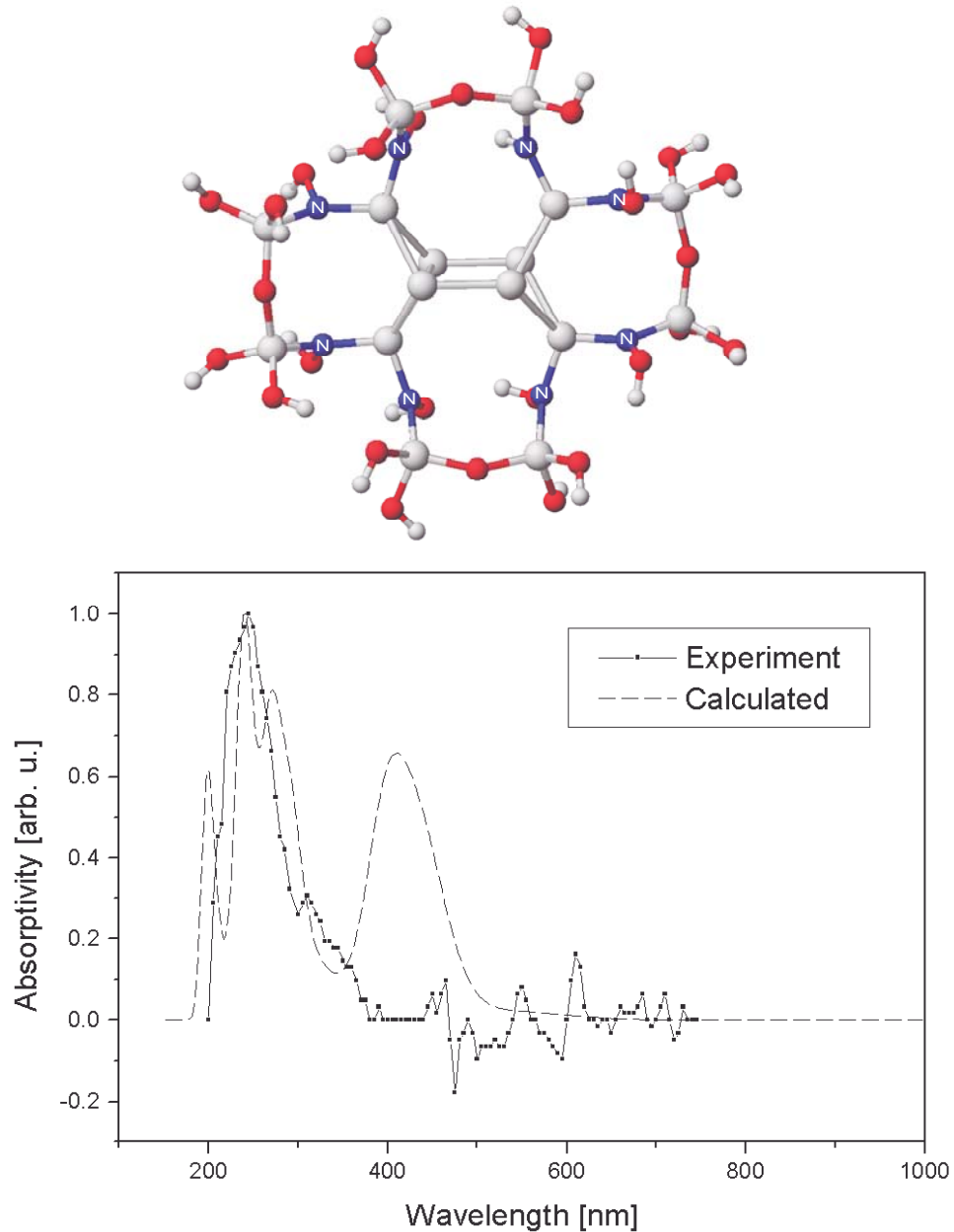


Figure 4-21. Si particle in amorphous silica matrix. The graph displays a comparison between the measured DR spectrum of sp- Si (appendix A) and the calculated spectrum of the cluster. The dark atoms represent O, the gray atoms represent Si, the small atoms represent H.

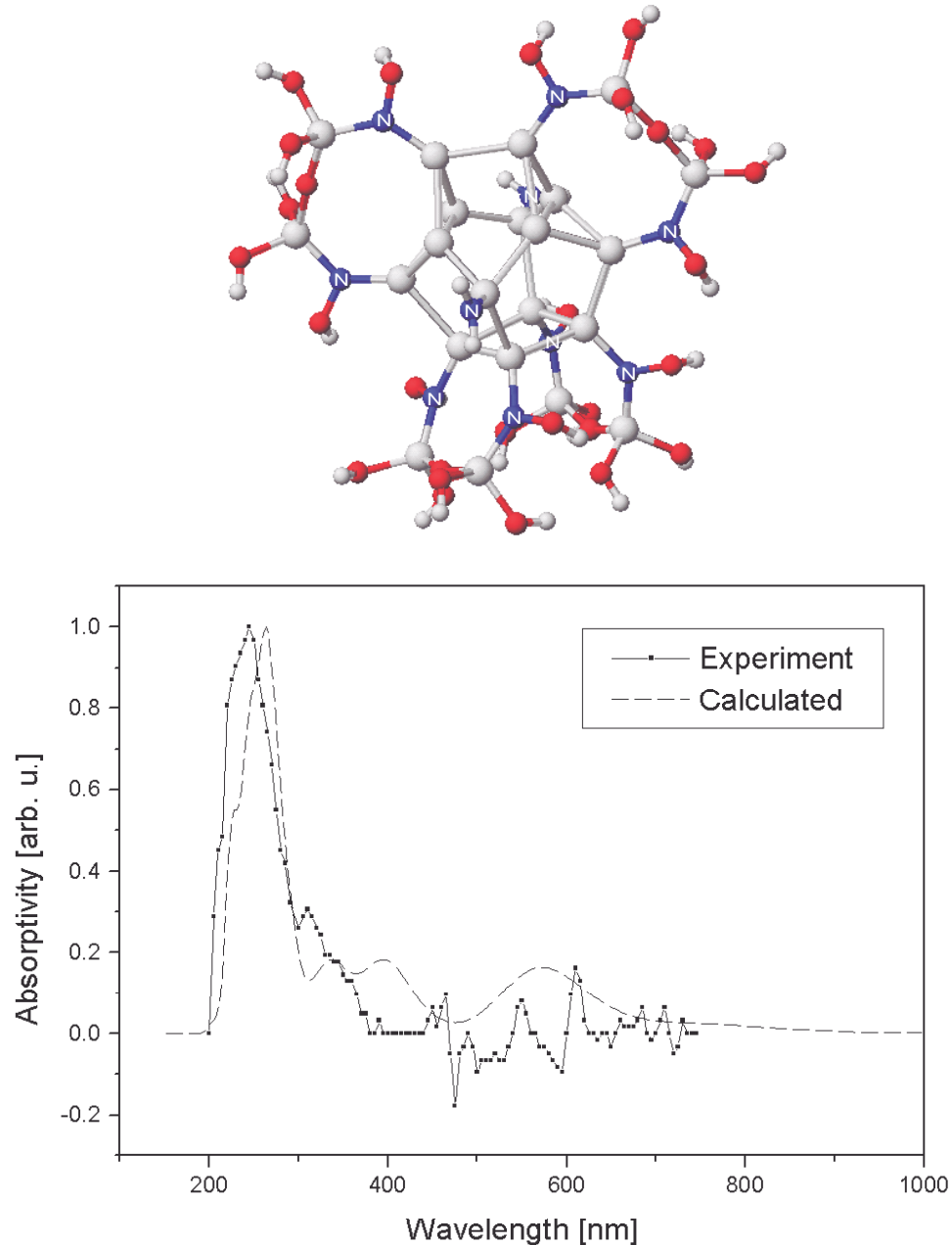


Figure 4-22. Si particle in amorphous silica matrix. The graph displays a comparison between the measured DR spectrum of sp- Si (appendix A) and the calculated spectrum of the cluster. The dark atoms represent O, the gray atoms represent Si, the small atoms represent H.

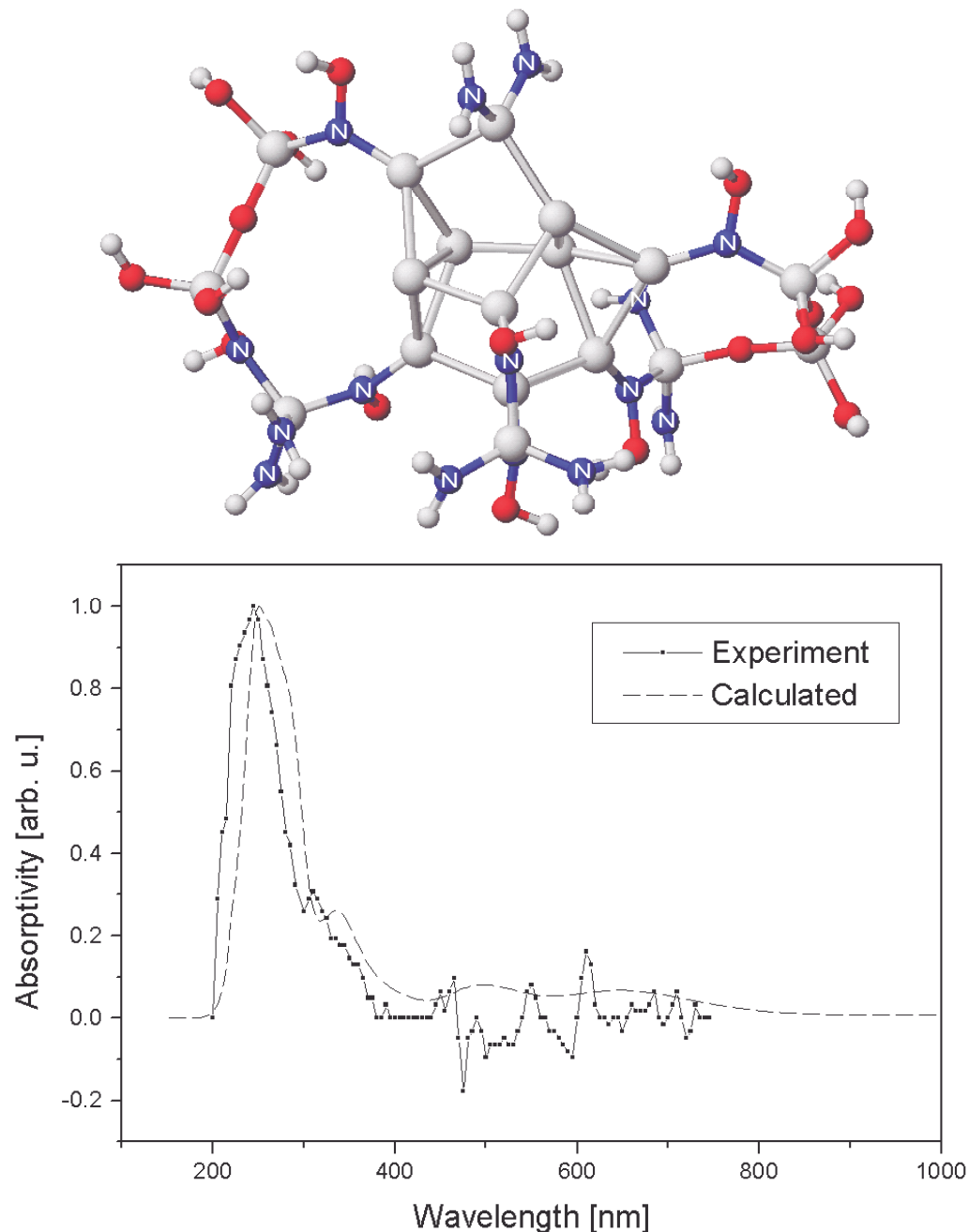


Figure 4-23. Si particle in amorphous silica matrix. The graph displays a comparison between the measured DR spectrum of sp- Si (appendix A) and the calculated spectrum of the cluster. The dark atoms represent O, the gray atoms represent Si, the small atoms represent H.

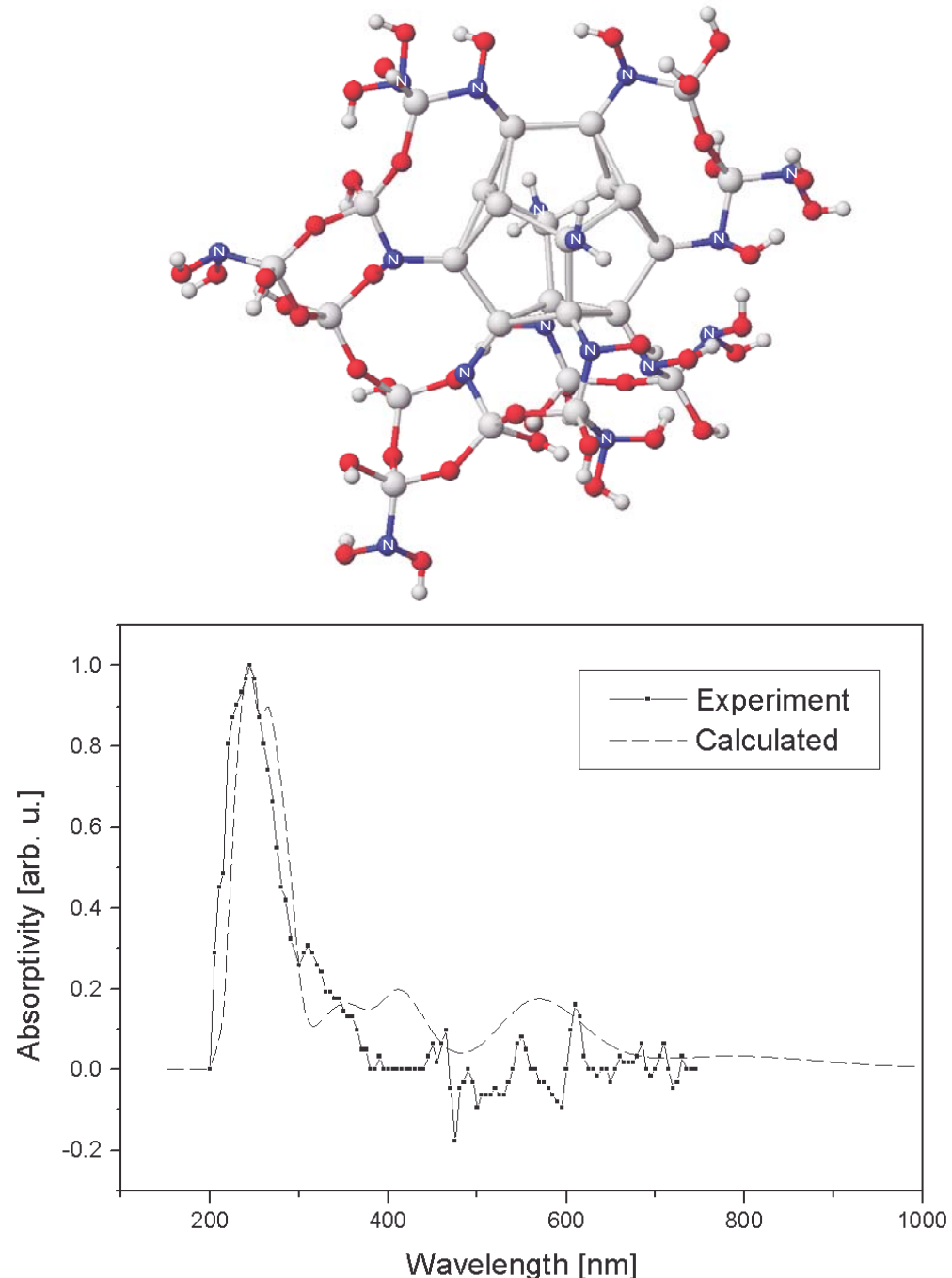


Figure 4-24. Si particle in amorphous silica matrix. The graph displays a comparison between the measured DR spectrum of sp-Si (appendix A) and the calculated spectrum of the cluster. The dark atoms represent O, the gray atoms represent Si, the small atoms represent H.

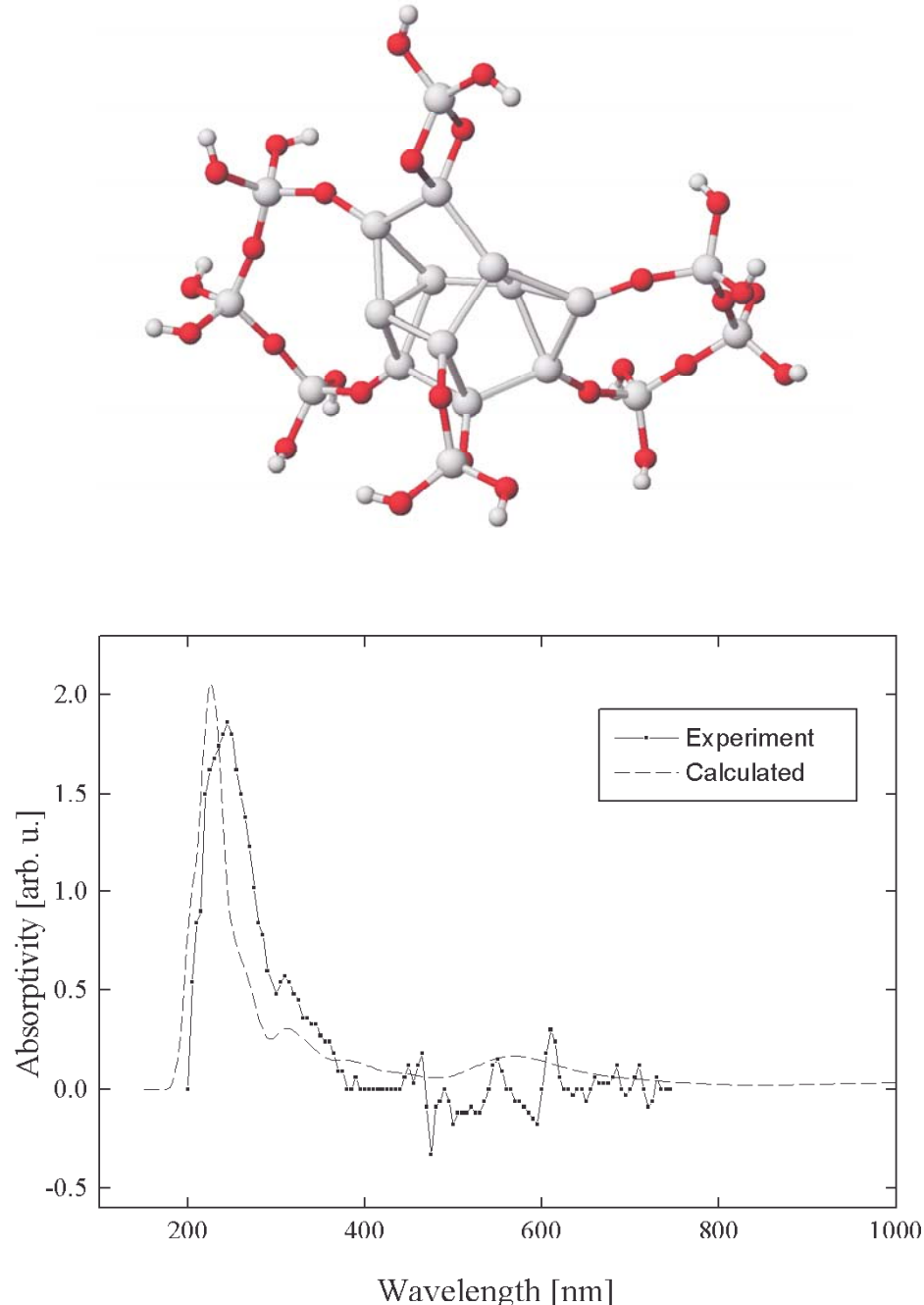


Figure 4-25. Si particle in amorphous silica matrix. The graph displays a comparison between the measured DR spectrum of sp- Si (appendix A) and the calculated spectrum of the cluster. The dark atoms represent O, the gray atoms represent Si, the small atoms represent H.

Since the calculated spectra of clusters with and without N atoms look similar (Figure 4-26), a χ^2 statistical analysis was performed in order to verify whether

calculated absorption spectra of structures with N would show improved agreement with the experimental spectrum of sp-Si. χ^2 was calculated as

$$\chi^2 = \frac{1}{n} \sum_k (E_k(\lambda) - T_k(\lambda))^2 \quad (4-3)$$

for a family of n clusters, each of them having a calculated absorption spectrum $E(\lambda)$. $T(\lambda)$ represents the absorption spectrum of sp-Si, processed in air. In this analysis, 5 different cluster families were studied:

- Si particles with 3, 4, 5, 6, 7, 8, 10 and 14 atoms, terminated with OH groups, without N atoms;
- Si rings with 3, 4, 5 and 6 atoms, terminated with OH groups, without N atoms;
- Si particles with 3, 4, 5, 6, 7, 8, 10 and 14 atoms, embedded in a-SiO₂ matrix without N atoms;
- Si particles with 3, 4, 5, 6, 7, 8, 10 and 14 atoms, embedded in a-SiO₂ matrix with high concentration of N atoms around the Si particle with bonding configuration Si₂ – N – H;
- Si particles with 3, 4, 5, 6, 7, 8, 10 and 14 atoms, embedded in a-SiO₂ matrix with high concentration of N atoms around the Si particle with bonding configuration Si₂ – N – O – H.

Each cluster group contained 17 different structures. The cluster families show different average χ^2 within 10⁻². (This is largely due to the fact, that all spectra were normalized to unity prior to the implementation of the statistical analysis). If χ^2 is plotted vs. Si cluster size (Figure 4-27), one can see that the agreement between theoretical prediction and experiment improves for larger Si clusters.

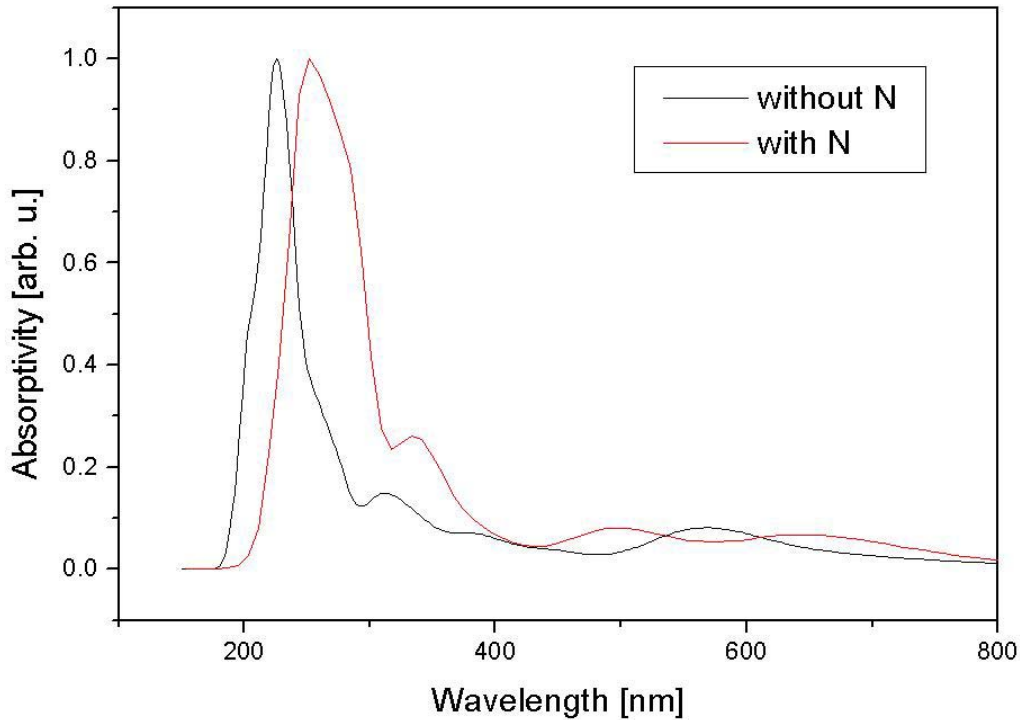


Figure 4-26. Calculated absorption spectra of a Si particle in an amorphous matrix with and without the participation of N atoms.

At a first glance, the obtained χ^2 values are nearly indistinguishable, because they are all very close to zero. It seems also, that there is no criterion, based on which some of the cluster families should be excluded as providing unsatisfactory χ^2 . To resolve this problem, we studied the differences between

- The experimental absorption spectrum of luminescent Si spark-processed in air;
- The experimental absorption spectrum of non-luminescent Si spark-processed in O atmospheres. (A detailed analysis of these two spectra is provided in Appendix A).

The optical properties of the two materials are substantially different. Their experimental absorption spectra are also qualitatively different. To quantify this

difference, we evaluated the χ^2 when the second spectrum is fitted to the first one. We achieved a χ^2 value of $\alpha = 0.1$. Therefore, any normalized calculated spectrum fitted to the experimental spectrum is considered to be unacceptable, if the χ^2 of the fit is in the order of 0.1 (this includes all χ^2 values between 0.05 and infinity). If the χ^2 of the fit lies below 0.05, there is no reason to treat the fit as unacceptable.

The plot of χ^2 vs. Si cluster size shows, that best agreement between theory and experiment is achieved for Si_{14} (Fig. 4-27). Let us consider for a moment a cluster size of 14 Si atoms only. In this case, a substantial difference is observed between clusters with and without N atoms. The clusters, where N is present, lie below the dividing line of 0.5. In general, for Si cluster sizes between 6 and 14, the complexes that contain N lie within the limit of acceptability. If the values of χ^2 for Si_{14} are extrapolated to infinity (the case of a large Si cluster), one can conclude that acceptable precision of the prediction is achieved in the cases when N atoms are present in the cluster.

Another issue that will be addressed here is the precision of the χ^2 estimate. The noise-to-signal ratio of the DR is 10^{-5} (Appendix A). Therefore, no appreciable error in the χ^2 will result from noise in the DR signal. The error of the calculation is ± 0.24 eV, coming from both the MOPAC geometry optimization and the INDO/S spectroscopic calculation. The error in the χ^2 values at Si_{14} were estimated by the following procedure:

- The DR and the calculated spectrum were plotted with respect to energy;
- The calculated spectrum was translated with ± 0.24 eV;
- The resulting χ^2 values were calculated.

The deviation in the χ^2 values at Si_{14} is estimated to be:

- (OH)-terminated Si clusters, no N: $\chi^2 = 0.08$; $\chi^2 \in [0.05, 0.1]$
- Si/SiO₂ clusters, no N: $\chi^2 = 0.07$; $\chi^2 \in [0.07, 0.1]$
- Si/SiO₂ clusters, with Si₂-N-O-H bonding: $\chi^2 = 0.03$; $\chi^2 \in [0.03, 0.09]$
- Si/SiO₂ clusters, with Si₂-N-H bonding: $\chi^2 = 0.01$; $\chi^2 \in [0.01, 0.04]$

The clusters that do not contain N have unacceptable χ^2 values (larger than 0.05). Si/SiO₂ clusters, with Si₂-N-O-H bonding provide an acceptable fit, but the χ^2 confidence interval is large and assumes values, beyond the acceptability limit of 0.05. Si/SiO₂ clusters with Si₂-N-H bonding have acceptable χ^2 values. Once again, the conclusion is that acceptable precision of the prediction is achieved in the cases when N atoms are present in the cluster. This trend will be further verified when more calculations are performed. It is expected that the clusters, containing N will have χ^2 that converges to zero when the size of the clusters increase to infinity. On the opposite, clusters that do not contain N atoms will have χ^2 that diverges from zero when the size of the clusters increases.

Silicon Spark-processed in Pure Oxygen

The experimental absorption spectrum of this material is shown in Figure 4-2. It shows three resolved peaks between 200 and 300 nm. Unlike sp-Si prepared in air, there is no absorption band at 320 nm in this case. Due to this reason, PL cannot be excited with a He-Cd laser (325 nm excitation wavelength). A χ^2 statistical analysis was performed for the same cluster families as above with the only difference that χ^2 was calculated with respect to the absorption spectrum of sp-Si, processed in pure O. Again, all cluster families show χ^2 within 10^{-2} and only those having $\chi^2 < 0.05$ can be preferred as a group that describes best the properties of sp-Si processed in O. The structures, containing N were included, since some N atoms may still exist in the processing atmosphere or can be attached after the sample preparation.

Some trends were observed when χ^2 was plotted vs. Si cluster size (Figure 4-28).

Again, agreement between theoretical prediction and experiment improves for larger Si clusters. When the values of χ^2 for Si₁₄ are extrapolated to infinity, one can conclude that acceptable precision of the prediction is achieved in the cases when N

atoms are absent (Figures 4-29 to 4-31). Si rings, terminated with OH groups, show poor (higher) χ^2 values.

Once again, the precision of the χ^2 estimate needs to be addressed. Since the noise-to-signal ratio of the DR is 10^{-5} (Appendix A), the χ^2 will not be influenced by the noise in the DR signal. The error of the calculation is ± 0.24 eV, coming from both the MOPAC geometry optimization and the INDO/S spectroscopic calculation. Once again, the error in the χ^2 values at Si_{14} were estimated by the following procedure:

- The DR and the calculated spectrum were plotted with respect to energy;
- The calculated spectrum was translated with ± 0.24 eV;
- The resulting χ^2 values were calculated.

The deviation in the χ^2 values at Si_{14} is estimated to be:

- (OH)-terminated Si clusters, no N: $\chi^2 = 0.05$; $\chi^2 \in [0.03, 0.05]$
- Si/SiO_2 clusters, no N: $\chi^2 = 0.03$; $\chi^2 \in [0.03, 0.07]$
- Si/SiO_2 clusters, with $\text{Si}_2\text{-N-O-H}$ bonding: $\chi^2 = 0.11$; $\chi^2 \in [0.07, 0.14]$
- Si/SiO_2 clusters, with $\text{Si}_2\text{-N-H}$ bonding: $\chi^2 = 0.13$; $\chi^2 \in [0.07, 0.18]$

The clusters that contain N atoms have unacceptable χ^2 values (larger than 0.05). (OH)-terminated Si clusters provide an acceptable fit, while the χ^2 confidence interval assumes the value of 0.05, being the only one unacceptable value. Si/SiO_2 clusters without N have χ^2 that occupies both acceptable and unacceptable values.

In conclusion one can say that better precision of the prediction can be achieved in the cases when N atoms are absent. Again, this trend can be further verified when more calculations are performed. It is expected that the clusters, containing N will have χ^2 that diverges from zero when the size of the clusters increase to infinity. On the opposite, clusters that do not contain N atoms will have χ^2 that converges to zero when the size of the clusters increases.

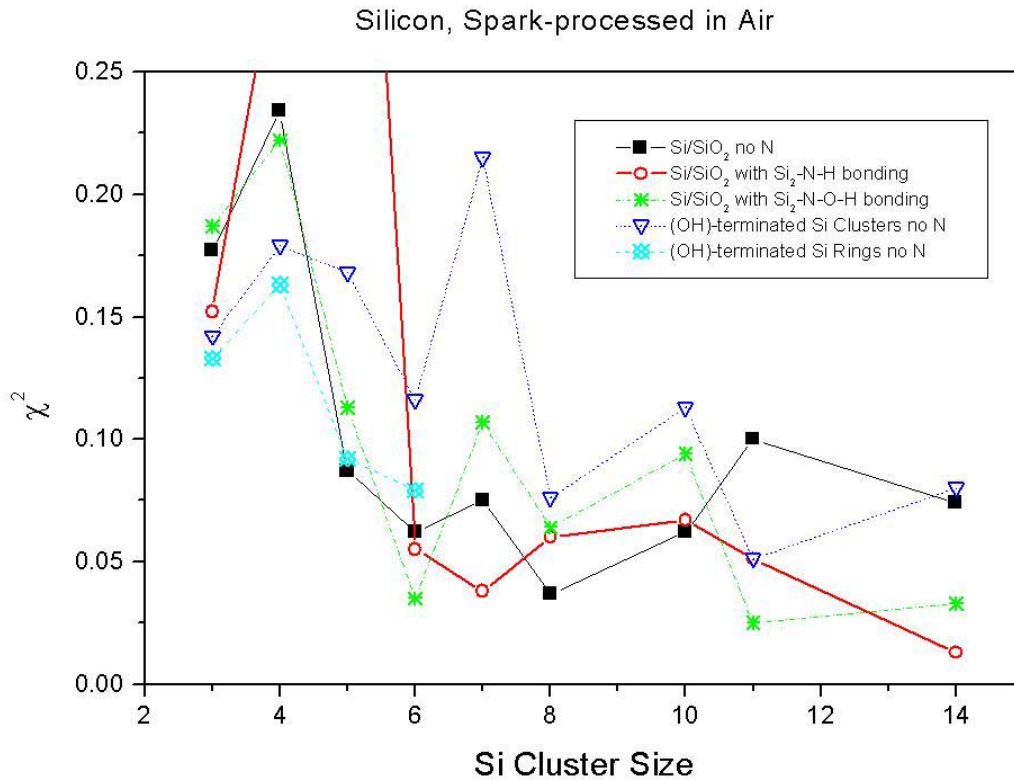


Figure 4-27. Silicon spark-processed in air. Statistical analysis for five different cluster families.

Si₆ Clusters in Spark-processed Silicon

The plot of χ^2 vs. Si cluster size (Figure 4-27) gives further insights about the difference between sp-Si processed in air and pure O at the molecular level:

- When the number of Si atoms is extrapolated to infinity, the agreement is expected to improve depending on the presence or absence of N atoms;
- χ^2 exhibits minima over certain Si cluster sizes. This can be interpreted to mean that the probability of the existence of such clusters is higher.

The cases of air and pure O are distinctly different with respect to these two features. For sp-Si, processed in air, Si₆ is a favored structure irrespective of bonding situation. This is no longer true for sp-Si, processed in O. Similar is the case of Si₈. This structure is again, favored in sp-Si processed in air. Such conclusion is not true for sp-Si, processed in O.

One of the Si_6 geometries is a cage structure [74 – 79]. It could be inferred that other cage structures might be preferentially created in the air atmosphere during spark processing. As seen above, processing in pure O seems to no longer favor the Si_6 clusters. It has to be noted also that further and extensive computational results are needed to obtain a much larger variety of Si cluster sizes. After such a study is accomplished, a possible trend in the minima of χ^2 may be more clearly visible.

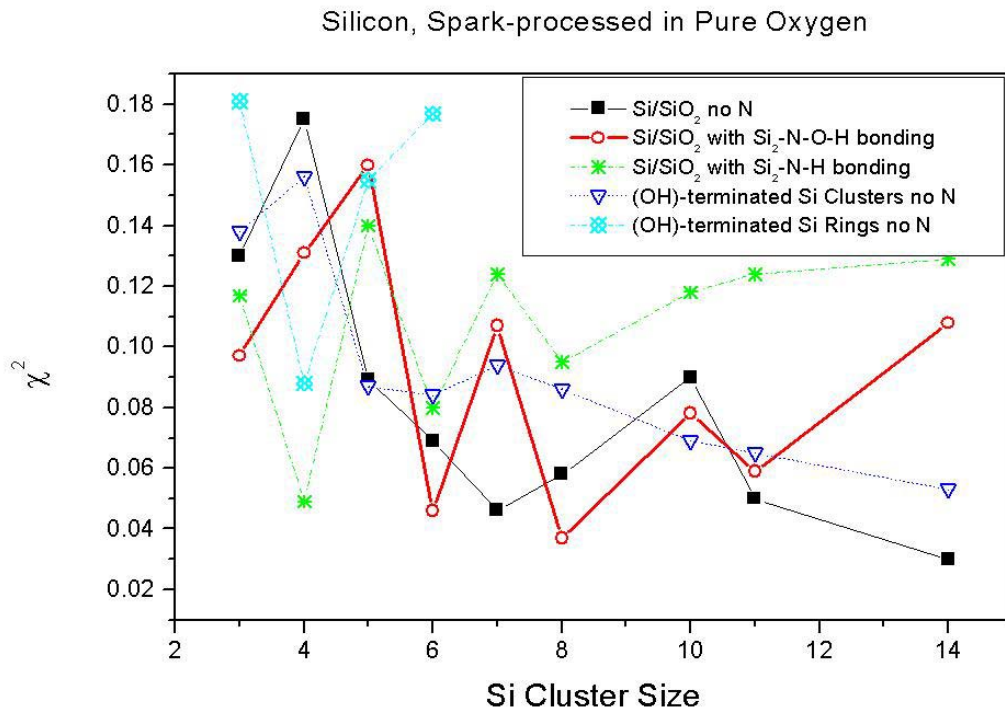


Figure 4-28. Silicon spark-processed in pure O. Statistical analysis for five different cluster families.

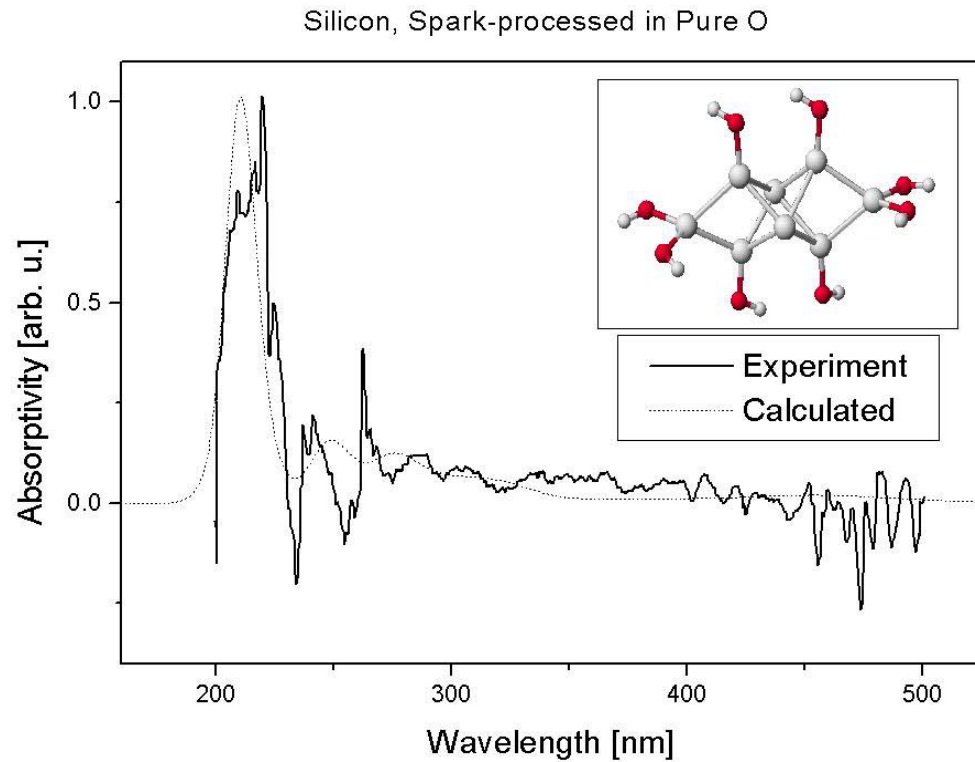


Figure 4-29. Si spark-processed in pure O atmospheres. The graph displays a comparison between the measured spectrum and the calculated spectrum of the cluster, shown in inset. Dark atoms represent O, small atoms represent H.

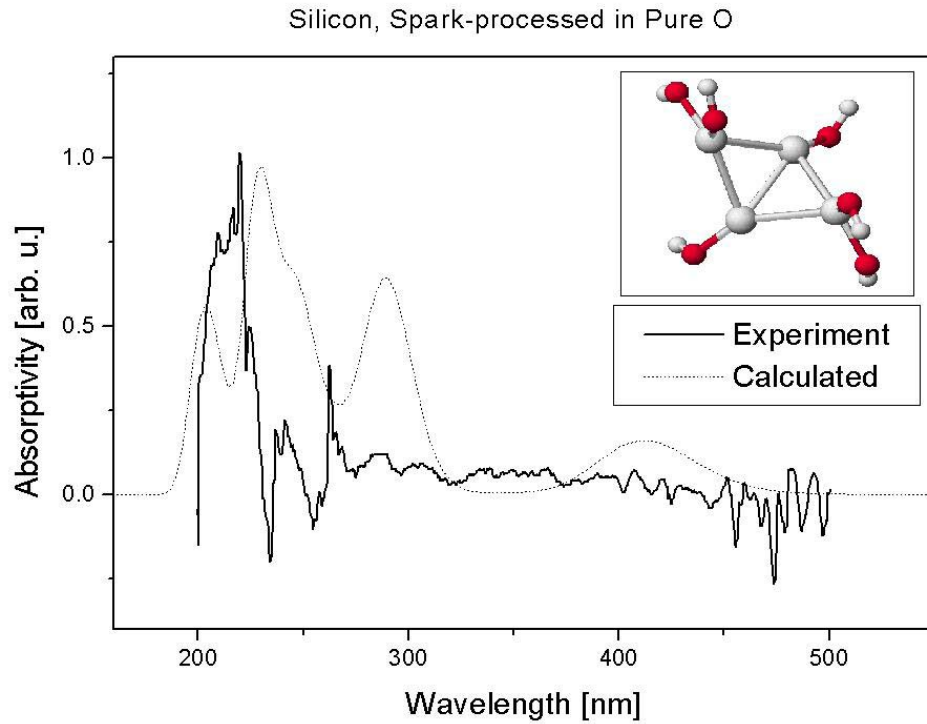


Figure 4-30. Si spark-processed in pure O atmospheres. The graph displays a comparison between the measured spectrum and the calculated spectrum of the cluster, shown in inset. Dark atoms represent O, small atoms represent H.

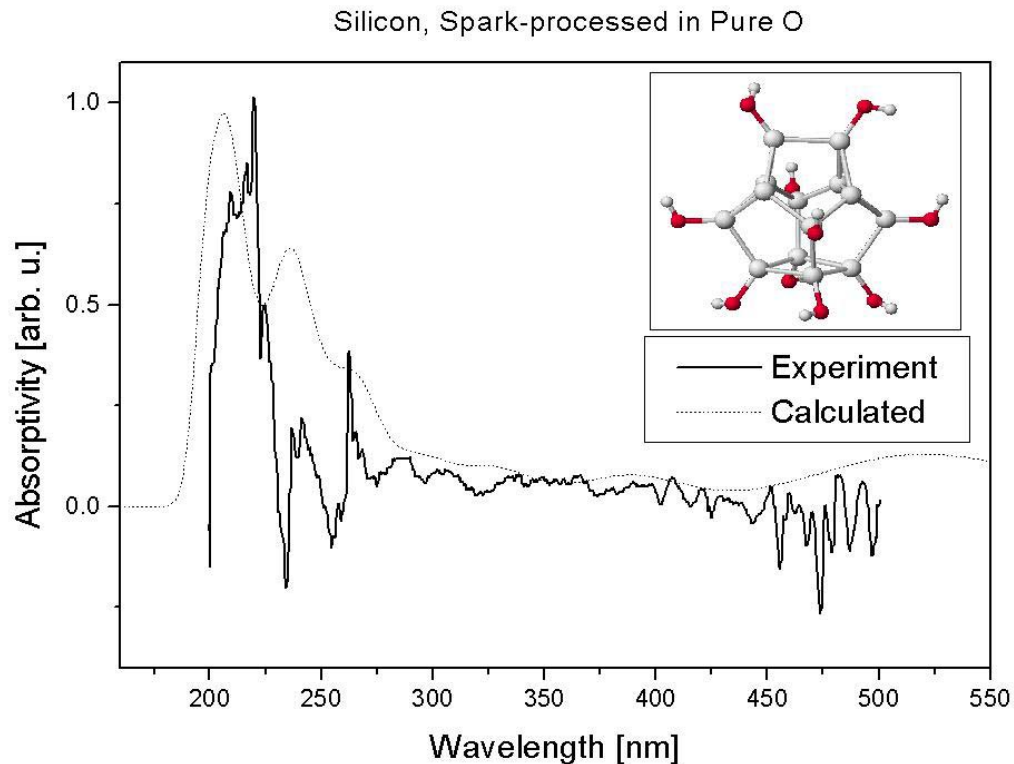


Figure 4-31. Si spark-processed in pure O atmospheres. The graph displays a comparison between the measured spectrum and the calculated spectrum of the cluster, shown in inset. Dark atoms represent O, small atoms represent H.

CHAPTER 5 SUMMARY OF RESULTS

The results of the present work can be summarized as follows:

- The calculated absorption spectra of Si particles in a-SiO_xN_y matrix reproduce remarkably well the experimental absorption spectrum of sp-Si. Further, the similarities between the PLE and the absorption spectra of light-emitting sp-Si, as well as the pico-second PL lifetimes, are interpreted to suggest that both the absorption and emission of light in sp-Si involve the same centers. The calculated absorption spectra strongly suggest that Si particles embedded in the amorphous insulating matrix of sp-Si play a key role in the process of light absorption and emission in this material.
- Si spark-processed in air: χ^2 statistical analysis with a large number of Si-based clusters shows that agreement between theoretical prediction and experiment improves for larger Si clusters. If the values of χ^2 for the largest Si cluster in this study are extrapolated to infinity, one can conclude that acceptable precision ($\chi^2 < 0.05$) of the prediction is achieved in the cases when N atoms are present.
- Si spark-processed in pure O atmospheres: Again, χ^2 statistical analysis with a large number of Si-based clusters shows that agreement between theoretical prediction and experiment improves for larger Si clusters. If the values of χ^2 for the largest Si cluster in this study are extrapolated to infinity, one can conclude that acceptable precision of the prediction ($\chi^2 < 0.05$) is achieved in the cases when N atoms are absent.
- The role of N in the optical properties of sp-Si: The computer models of the optical properties of sp-Si show best agreement between theory and experiment for molecular clusters with participation of N atoms. The N atoms pile up at the dielectric/Si interface with bonding configurations Si₂ – N – O.
- Si₆ clusters in sp-Si: the plot of χ^2 vs. Si cluster size (Si spark-processed in air) consistently exhibits minima at Si₆, irrespective of bonding configurations. Similar behavior is observed in the case of Si₈. It can be concluded, therefore, that Si clusters with sizes 6 and 8 are preferentially created during sp-Si growth. The distinctive minima in the plot of χ^2 are no longer observed for Si spark-processed in O. It has to be noted, though, that further extensive computational results are needed for a much larger variety of Si cluster sizes. After such a study is accomplished, the trend in the minima of χ^2 may be more clearly visible.

- Amorphous SiO₂ was modeled with 2-, 3-, 4-, 5- and 6-member silica rings. In general, silica clusters do not exhibit absorption bands below 6.2 eV (200 nm). Upon substitution of O atoms with N in the structure, electronic excitations with lower energies are possible. Such substitutions in the small 2-member silica ring with double Si=O bond result in absorption peak at 5.05 eV (245 nm). This property can be retained with attachment of the small ring to a larger one. The electronic transition amplitude at 245 nm is located over the N atoms in the 2-member silica ring.
- Amorphous Si was modeled with 3-, 4-, 5-, 6-member rings and with small Si clusters having between 2 and 14 Si atoms, terminated with OH groups. All spectra of Si rings exhibit three characteristic peaks, positioned between 200 nm and 350 nm. On average, the peak located in the neighborhood of 200 nm has the highest intensity, while the other two peaks at 260 nm and 320 nm have comparable magnitude and usually overlap. In many spectra, a low-intensity peak appears in the interval between 400 nm and 500 nm.

The substitution of an O atom by an N atom in a Si ring cluster does not substantially influence its optical properties. However, it has a certain influence on its structure. The average atomization energy $\langle E_a \rangle$ of such clusters decreases as the number of the substitute N atoms increase. The atomization energy $\langle E_a \rangle$ increases when a silica ring is attached to the Si ring cluster. The degree of importance of the variations of $\langle E_a \rangle$ has not been studied.

OH-terminated Si₂ – Si₁₄ have properties very similar to those of OH-terminated Si rings. The spectra always exhibit a triple-peak feature at or around 205 nm, 250 nm and 320 nm. The variation of the peak positions is within ± 5 nm for the first peak, within ± 20 nm for the middle peak and within ± 30 nm for the peak at 320 nm. Almost without exception, a weaker peak between 400 nm and 500 nm is also observed. In the studied Si-based molecules, the attachment of (OH) groups leads to structural stabilization, which is most pronounced in the absence of (NH₂) groups. The degree of importance of the variations of $\langle E_a \rangle$ has not been studied. The presence or absence of N atoms does not influence substantially the optical properties of this cluster group.

The properties of sp-Si strongly depend on the chemical content of the processing atmosphere. When N is present in the gas, certain Si geometries are created and embedded in an amorphous solid phase material. The N atoms pile up around the Si particles and exert influence on their structural and optical properties. Spark-processing of Si in air is a technique that creates stable, light-emitting Si particles embedded in an amorphous SiO_xN_y matrix.

The calculated spectra of silica ring-, Si ring-, Si cage-shaped clusters and their combinations can be compared with the measured spectra of Si- or silica-based light-emitting materials. The results of the present work can be used to provide further insights about the role of Si particles in the optical properties of such materials.

CHAPTER 6 FUTURE WORK

The graph χ^2 vs. Si cluster size (Figure 4-26, Section 4) has a defined minimum at Si_6 in the case of Si spark-processed in air. Further calculations with clusters $\text{Si}_{15} - \text{Si}_{60}$ are necessary, since they can reveal similar minima, positioned over the magic numbers Si_{20} , Si_{33} , Si_{45} and Si_{60} . Also, the general trend of

$$\chi^2(\text{Si}_n) \rightarrow 0 \quad \text{when} \quad n \rightarrow \infty \quad (6-1)$$

will be further verified.

The optical properties of the sp-Si material depend on the geometry of the light-emitting clusters in its bulk. Further work on the structural properties can reveal whether this dependence is valid on higher dimensional scales. Part of this study has already been accomplished with the stereological study of the porosity and density of sp-Si (Appendix B). It is currently being continued with fractal analysis of sp-Si and other spark-processed materials. The accomplished stereological analysis (Appendix B) may prove helpful in the calculation of the fractal dimension of spark-processed surfaces. So far, it has been visually established that such surfaces exhibit fractal behavior in the case of sp-Si, since they show repetitive structural features at various scales (Figure 6-1).

It has been shown by experiment [6], that N atoms play an important role in the optical properties of various spark-processed materials. Further calculations can provide models for the light-emitting centers in these substances and give clues about the importance of N in the process of light emission.

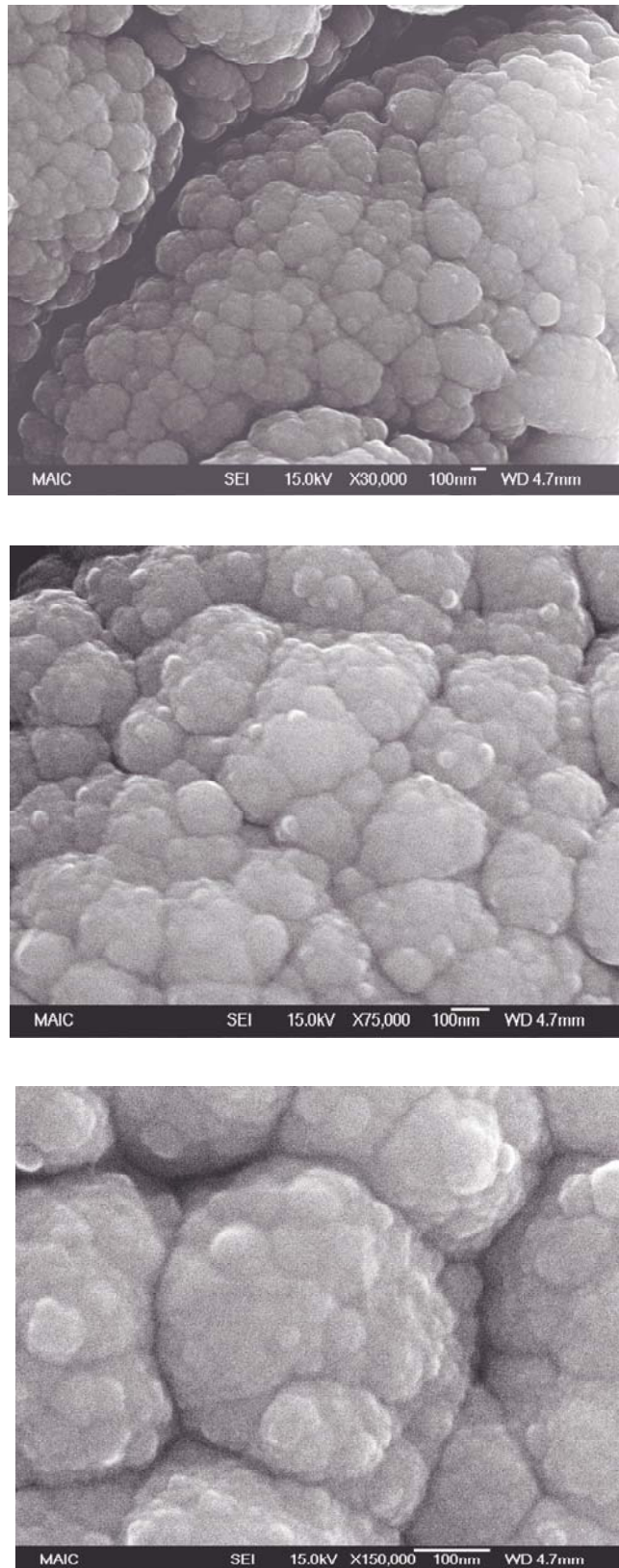


Figure 6-1. The fractal nature of the sp-Si surface.

APPENDIX A SHORT INTRODUCTION INTO DIFFERENTIAL REFLECTOMETRY

Differential reflectometry is an analytical technique, which uses UV/visible/IR monochromatic light for the measurement of the optical absorption spectra of metals and semiconductors. The incoming beam scans the surface of two adjacent samples with reflectivities R_1 and R_2 (50 – 100 monolayers) and having a small difference in composition X. A schematic representation of the experimental setup is shown on Figure 7-1. The output signal from a differential reflectometer is called a differential reflectogram (DR) and has the form [92]

$$\frac{\Delta R}{\langle R \rangle} = A \left[\left(\frac{d \omega_T}{dX} \right)^2 + \left(\frac{d \Gamma}{dX} \right)^2 \right]^{1/2} F \left(\frac{\omega - \omega_T}{\Gamma}, \vartheta \right), \quad (7-1)$$

where

$$F(s, \vartheta) = \sin \phi(s) \cos [\phi(s) - \vartheta]$$

$$\phi(s) = \operatorname{Arc sin} \frac{1}{\sqrt{1+s^2}}.$$

$$\langle R \rangle = \frac{R_1 + R_2}{2}$$

Γ is used to denote the lifetime broadening frequency, ω_T is the electronic transition frequency, A, s and θ are parameters and X denotes the chemical composition of the studied material. Detailed treatment on the DR experimental procedure and description of the DR line-shape analysis has been published [93–95]. The signal-to-noise ratio of the DR is 10^{-5} . The line shape of the DR spectrum is determined by the function F .

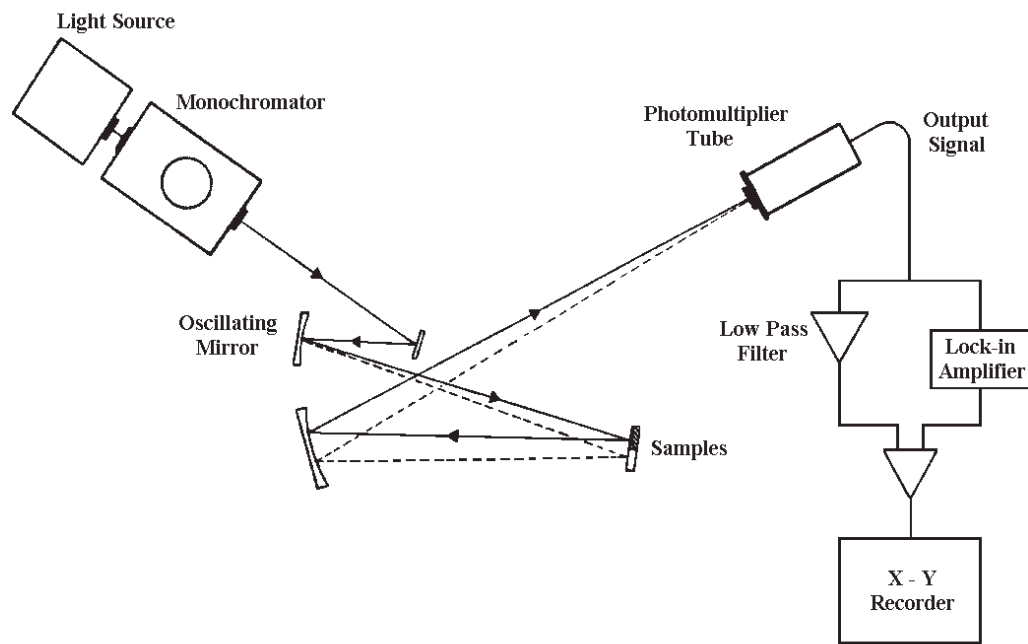


Figure A-1. A schematic representation of a differential reflectometer's instrumentation setup.

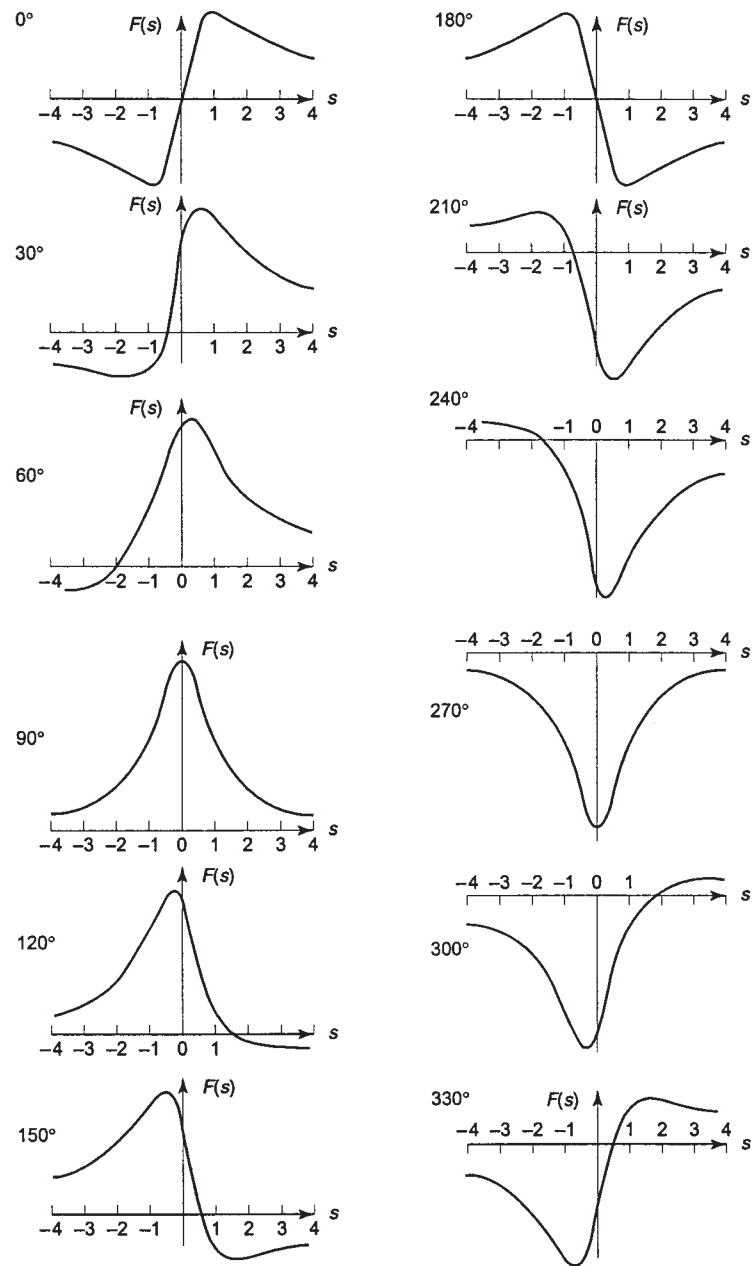


Figure A-2. $F(s, \theta)$ for selected values of θ [94].

Depending on the values of the θ parameter, the different peaks in the DR spectrum will have shapes, as shown on Figure 7-2.

Since in the crystalline material the electronic transitions occur between well-defined energy bands, the DR spectrum in this case can be thoroughly analyzed, by fitting a limited number of F functions to it. Each of the functions is analyzed, the value of θ is determined and finally, the precise transition energy is calculated.

In the case of amorphous materials, a variety of electronic transitions take place. Only in one of the calculated spectra in this work, tens of electronic transitions are observed. The experimental DR of sp-Si is a result of all the excitations from the variety of clusters in the material and will therefore contain a very large number of transitions. In such situations, a precise line-shape analysis of the DR spectrum is impossible.

Therefore, the analysis of the DR characteristic of sp-Si (Figure 7-3) will be based on certain assumptions. First, the DR bands positioned between 200 and 450 nm will be considered to have a θ parameter = 90° . Therefore, the electronic transition energies within these bands do not need to be corrected. The bands between 450 and 800 nm obviously have components with $\theta \neq 90^\circ$. They were not corrected, but it was rather assumed that energy bands do exist in this region in the vicinity of the observed peaks (the correction factors are usually around 10^{-2} eV).

The DR signal can be expressed in terms of the real and imaginary components of the dielectric constant ϵ [92]:

$$\frac{\Delta R}{\langle R \rangle} \propto \sum \frac{d\epsilon_k}{dX}, \quad (7-2)$$

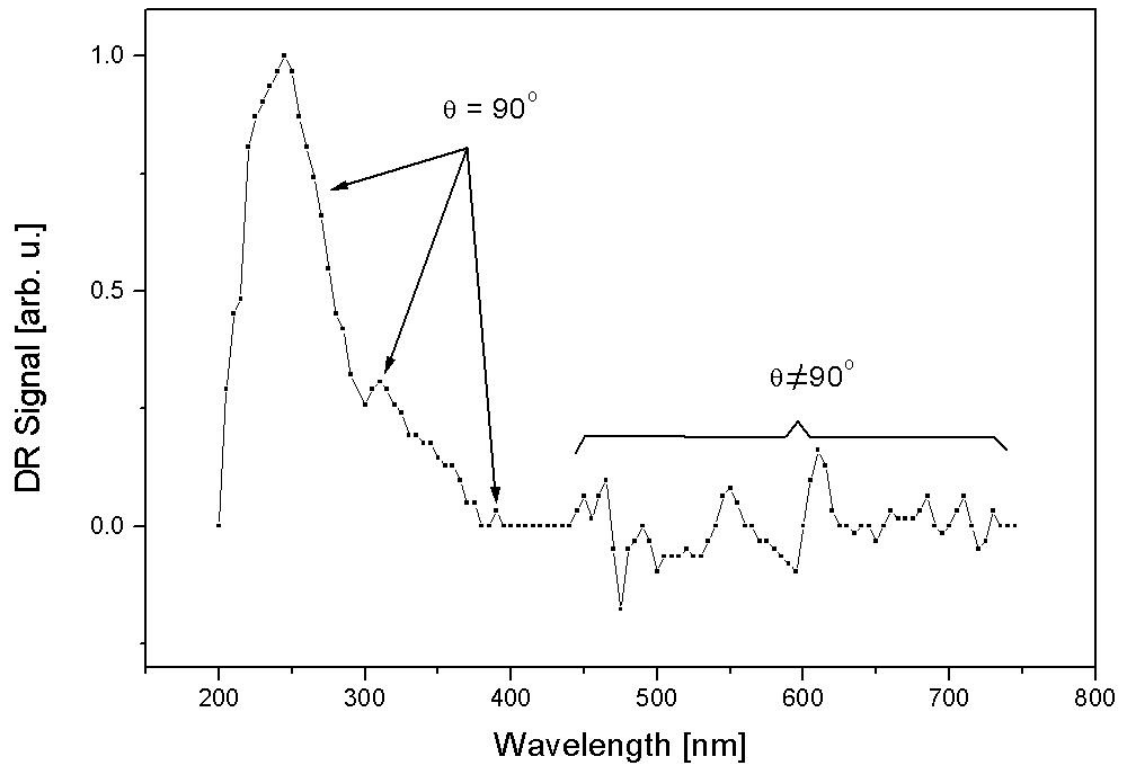


Figure A-3. Differential Reflectogram of Si spark-processed in air.

where ε_k is either $\text{Re}(\varepsilon)$ or $\text{Im}(\varepsilon)$. Therefore, the DR spectrum in fact represents the absorption spectrum of the studied material since ε is proportional to the absorption coefficient.

In the present work, the DR spectrum of sp-Si was compared to calculated absorption spectra of various Si-based clusters. The comparison was done visually and a good fit was considered to be one, which reproduced closely the DR envelope. The χ^2 analysis, described in Section 4 was performed always between 200 and 450 nm, since the rest of the DR spectrum was not corrected. The peaks between 450 and 800 nm do not show negative absorption, but correspond to DR absorption peaks with $\theta \neq 90^\circ$, see Figure 7-2.

The DR spectrum of Si spark-processed in pure O is plotted in Figure 7-4. As shown above, it represents the absorption spectrum of the material. Again, similarly to the above case, this spectrum was analyzed based on the assumption that the energy bands between 200 and 450 nm have $\theta \approx 90^\circ$, while the bands between 450 and 800 nm have components with $\theta \neq 90^\circ$. The latter were not corrected, but it was assumed that energy bands do exist in this region in the vicinity of the observed peaks. The χ^2 analysis to this spectrum (Section 4) was performed always between 200 and 450 nm, where $\theta \approx 90^\circ$.

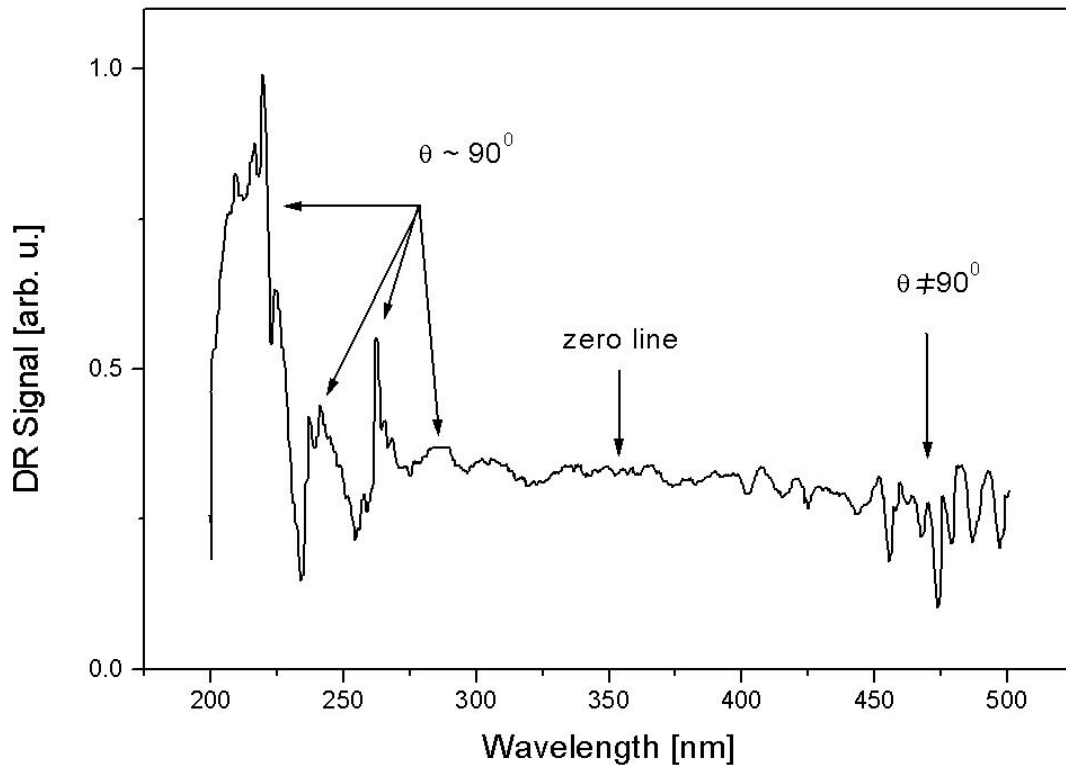


Figure A-4. Differential Reflectogram of Si spark-processed in pure O atmospheres.

APPENDIX B POROSITY AND DENSITY OF SPARK-PROCESSED SILICON [96]

Abstract

Spark-processed Si (sp-Si) is a porous solid-state material. Due to the nature of its structure and morphology, the traditional methods for porosity measurements are not applicable. Using the Measure Theory and the expected value theorems of stereology, we have calculated the porosity of sp-Si to be 43%. Stereological analysis was applied to sp-Si specimen, prepared within a fixed set of growth parameters. Over 60 cross-sectional scanning electron micrographs of the specimen were utilized in this work. The sp-Si sample has a characteristic cylindrical symmetry due to the uniform surface resistance of the Si substrate and to the random nature of spark processing. However sp-Si is not isotropic, uniform and random (IUR), but rather exhibits radial and axial anisotropy of porosity. To avoid bias in the calculation, we chose random areas of the cross-sectional surface of sp-Si and calculated their porosities. The calculated values entered into a weighted statistical distribution, in which the statistical weights were determined from the symmetry properties of the sample. The statistical approach and the fact that volume is an additive quantity, allowed us to use a 2-dimensional population of points in the calculation of the 3-dimensional pore volume fraction and to satisfy the requirement for IUR sample. Small-spot X-ray photoelectron spectroscopy studies of sp-Si were used in the calculation of its density. In the case of inhomogeneous materials, the density is a weighted (with respect to volume) average of the densities of all participating phases.

Taking into account the already calculated porosity, we have estimated the density of sp-Si to be 1.36 g/cm^3 . The main contribution to this value comes from amorphous SiO_2 , which occupies most of the volume of sp-Si.

Introduction

There are a variety of Si-based materials, which offer a variety of physical properties ranging from insulating to highly conductive. A subclass of these materials has light-emitting properties and has been an object of increasing interest in the past decade. However, the physical nature of the light emitting Si-based materials has presented some challenges in the attempts to study their local atomic structure and other physical properties closely related to it. The reason for that is the inhomogeneous structure of such materials. Light-emitting Si achieved by laser ablation [97], porous Si [98] and a variety of porous silica [99 – 104] have light-emitting properties and are inhomogeneous in most cases. The bulk of these materials usually contains mixtures of phases - crystalline, amorphous, surface oxide layers and the frequently present voids (pores).

Technological application of the above materials requires deposition of metal contacts or other thin films on their surface. In such procedures, surface and volume porosity of the underlying material is quite important, since it can allow or disallow smooth and continuous surface coverage. Thus, structural characterization and understanding of morphology are vital if one is to develop a successful contact deposition process.

The present work represents a study of light-emitting, spark-processed Si (sp-Si, Figure 8-1) and its topological and structural properties. Sp-Si has stable photoluminescence (PL) [1], which is highly resistant against aging, UV irradiation and thermal annealing up to 1100°C [3]. In addition, sp-Si based electroluminescent devices

have successfully been built [105 – 107] and are currently undergoing a process of optimization. Electroluminescent sp-Si devices are usually prepared in air, utilizing short spark processing times (10 – 20 seconds). The material used in the present work was prepared under identical conditions.

The bulk of sp-Si is highly inhomogeneous and porous. Its morphology and structure have not been studied so far. Understanding of these properties has value from a physical point of view; it can be also used to provide further insights for improved metal contact deposition techniques.

Method

The study of sp-Si porosity presents a serious challenge. The traditional methods for porosity measurements cannot be applied due to the nature of sp-Si growth and morphology. Surface atom adsorption techniques are not applicable, since sp-Si contains a large portion of internally embedded, closed pores (Figure 8-2). The techniques that involve pore filling are excluded for the same reason. In addition, the bulk contains pores with dimensions in the order of nanometers. Filling of such pores with liquid may not be complete and would introduce an unpredictable error in the measurement. Calculation of the porosity through mass measurements is possible, however this method requires also precise volume measurements. There were a number of attempts to utilize this technique, but these efforts did not yield useful results. The main obstacle was the porous surface of sp-Si, which contains features varying in dimensions from the micrometer scale to the nanoscale. The volume could not be measured with sufficient precision since the upper surface could not be mapped correctly (illustrated on Figure 8-3). Additional difficulties arise from the fact that the sp-Si material is not simply deposited on a Si substrate but

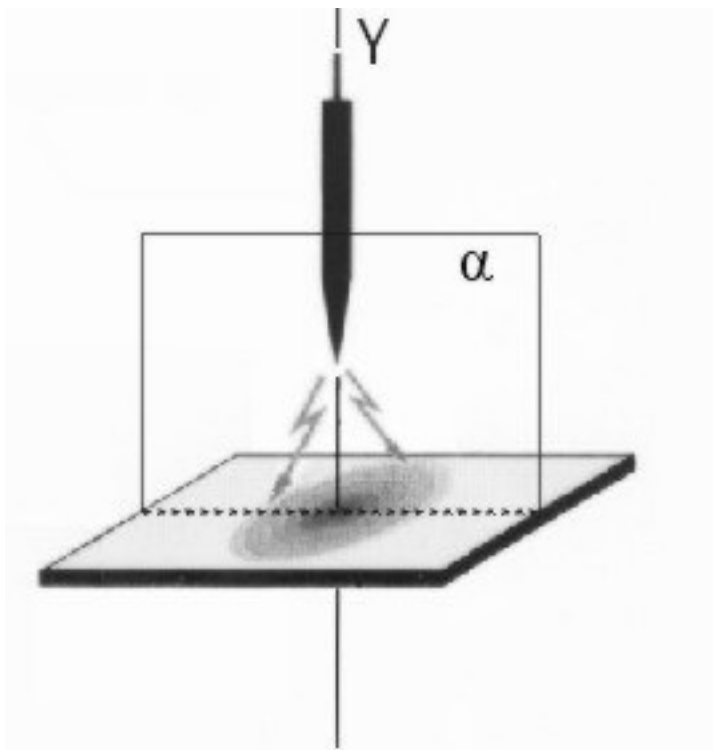


Figure A-1. Spark-processing of Si. Plasma discharges are directed from a tungsten tip to a Si substrate. Y is an axis of symmetry, while α is the plane of cross-sectional cut in Figure 8-2.

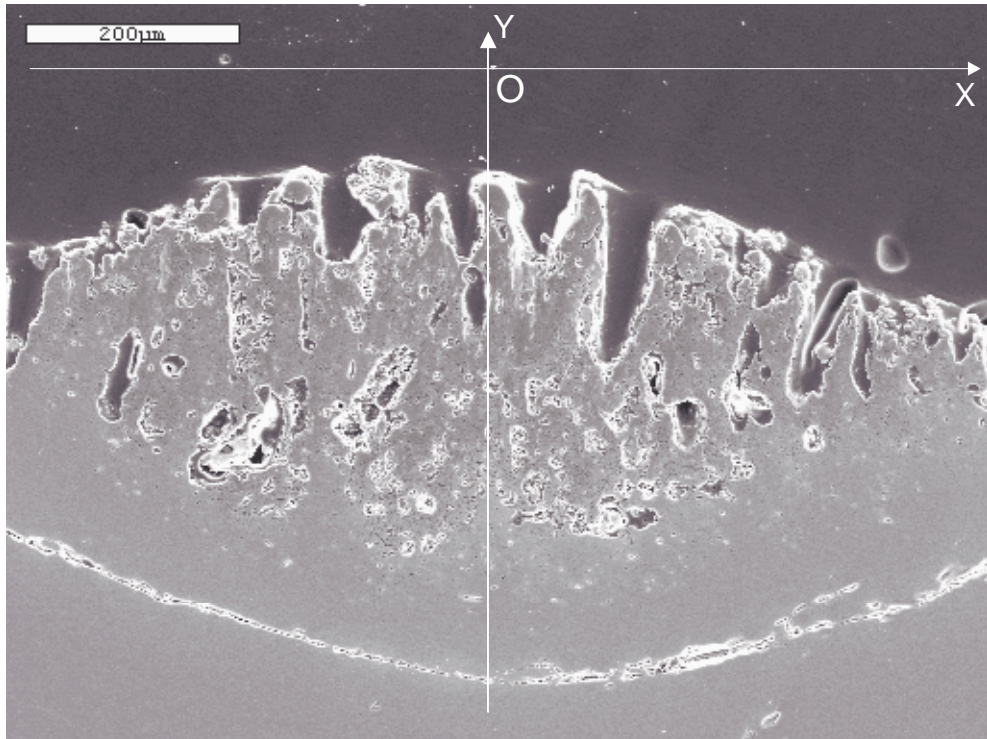


Figure A-2. Cross-sectional SEM micrograph of sp-Si at a magnification of x120. Y is the axis of symmetry, X is a radial axis.

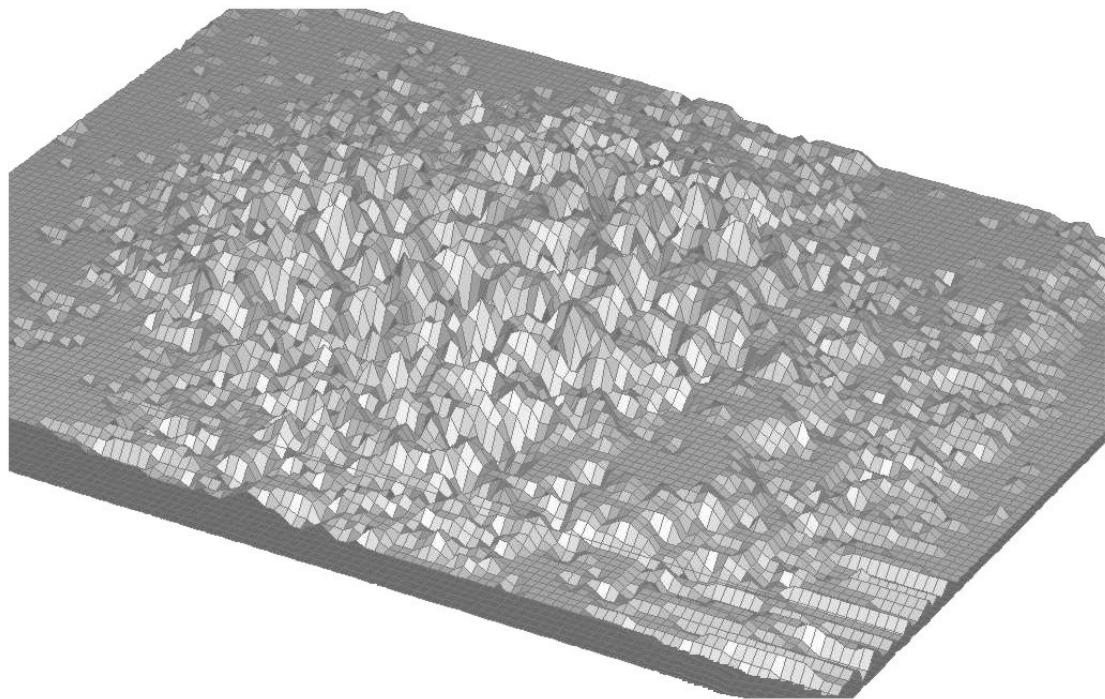


Figure A-3. SEM ma of the sp-Si surface.

extends into it, thereby occupying a certain volume in the substrate, which is not easy to estimate. In other words, the underlying surface between the sp-Si and the Si substrate cannot be mapped correctly either.

Solution to these problems was achieved by the application of stereological measurements. The *expected value theorems* of stereology allow the calculation of volume fraction of phases, surface area per unit volume, average feature size and feature perimeter, to name a few. Detailed description of the various stereological techniques can be found in the literature [108].

In the Measure Theory, the volume V_{Ω} of a set of points Ω (in 3-dimensional space) is defined as a measure of the set Ω . The measure of Ω can also be expressed as a function f , which associates a number V_{Ω} with the set Ω :

$$V_{\Omega} = f(\Omega) \quad (8-1)$$

Using the Peano-Jordan Measure in 3-dimensional space, we can state that the volume V_{Ω} of the set Ω is proportional to the number of points in Ω , and the functional dependence f (equation 8-1) has an integral form:

$$V_{\Omega} \propto \int_{\Omega} dp = \int_{\Omega} dx dy dz, \quad (8-2)$$

where dp is the density of points in 3-dimensional space, $dp=dx dy dz$. The Measure Theory will then allow the calculation of the ratio of two volumes of 3-dimensional sets Ω_1 and Ω_2 as a ratio of their corresponding measures:

$$\frac{V_{\Omega_1}}{V_{\Omega_2}} = \frac{f(\Omega_1)}{f(\Omega_2)}. \quad (8-3)$$

Applied to the case of sp-Si, this ratio will be

$$\begin{aligned} \langle P_p \rangle^{\text{porosity}} &= \frac{V(\text{voids})}{V(\text{entire sample})} = \frac{f(\text{voids})}{f(\text{entire sample})} = \\ &= \frac{\int_{\text{entire sample}} dp}{\int_{\text{entire sample}} dp} = \frac{\int_{\text{entire sample}} dx dy dz}{\int_{\text{entire sample}} dx dy dz} = V_p, \end{aligned} \quad (8-4)$$

where V_p is the volume fraction of porosity. The above equation can be applied directly for calculation of porosity of sp-Si and its form will be:

$$\langle P_p \rangle^{\text{porosity}} = \frac{\text{measure of the set of points in the porous phase}}{\text{measure of the set of points in the entire sample}} = V_p \quad (8-5)$$

where P_p is the so-called “point fraction”. This equation allows us to study the properties of a population of points in 2-dimensional space and apply the result to the 3-dimensional structure of the sample.

It is very important to note, that the expression (8-5) is valid only for samples, which are IUR, *i. e.* isotropic, uniform and random. The application of (8-5) to a sample, which is not IUR will lead to a biased result.

Sp-Si presents a challenge, since the sp-Si sample is not IUR, but exhibits anisotropy of porosity along the X (radial anisotropy) and Y axes (axial anisotropy, Figure 8-2). To avoid bias, we need to calculate an average porosity of the sample, which removes the anisotropy effect. Therefore, we have proceeded as follows:

- A sample of sp-Si was cut in a cross-sectional manner (Figure 8-1);
- The sample was embedded in a resin and fine-polished with diamond powder to produce a smooth cross-sectional surface;
- The image of the cross-sectional surface was captured using scanning electron microscope (SEM) at a magnification of x120 (Figure 8-2);

- A line grid was placed over the image. The spark-processed area (defined by the surface and the interface lines in Figure 8-2) was divided into 154 numbered tiles. Each tile is a square having a side of 44.4 μm ;
- The set of 154 tiles was subdivided into 32 groups of consecutive tiles. Each group contains 4 or 5 tiles;
- From each group, we selected randomly one tile as follows:
 - o tile number 4;
 - o tile number (4+5);
 - o tile number (9+4);
 - o tile number (13+5), and so on.

This process of random selection provided us with 32 tiles with numbers 4, 9, 13, 18, 23, and so on;

- SEM micrographs at magnifications x650 were taken for each of the 32 random tiles. At this magnification, nanopores could not be studied;
- Linear grids were placed over the images of each tile and the porosity was calculated from equation (8-5). The numerator is the number of grid intersections over voids (marked with bright circles, Figure 8-4), while the denominator in (8-5) is the total number of grid intersections.

Since sp-Si also contains pores with nanometer-scale dimensions, they have to be taken into consideration when porosity is calculated. Since a magnification of x650 is insufficient for counting of nanopores, we prepared a second set of SEM micrographs of the above 32 tiles, captured at a magnification of x3000 and applied equation (8-5) to calculate the nanoporosity (Figure 8-5). The magnifications of x3000 showed sufficient detail and were not improved with increase of magnification. To avoid duplicate pore counting, all high-resolution micrographs were captured from random areas (within the given tile) that do not contain macropores.

Thus, the total porosity P_i^{total} measured on a tile i , is determined to be

$$P_i^{\text{total}} = P_i^{\text{micro}} + P_i^{\text{nano}}. \quad (8-6)$$

One also needs to take into account the fact, that the sp-Si sample has cylindrical symmetry (Figure 8-1) with an axis of symmetry Y. The cylindrical symmetry is contingent upon the characteristics of spark processing. Normally, the Si substrate is uniformly doped and therefore its resistivity is the same throughout its bulk. Once a spark event occurs at a given point of the substrate surface, the resistivity of this particular locality increases, since spark processing creates clusters of highly resistive surface compounds [3]. The next spark event will most probably occur at another surface point with lower resistivity. Each spark occurs at a surface spot such, that the resistance between the sparking tip and the spot is minimal. This fact guarantees the circular surface pattern, observed after spark processing of Si (Figure 8-1).

Since each tile is positioned at some distance from the Y axis (Figure 8-2), it represents a volume ΔV_i

$$\Delta V_i = 2\pi h R_i \Delta R , \quad (8-7)$$

where R_i is the distance between the Y axis and the geometrical center of the tile i and $h=\Delta R$ is the tile side. Then, to each tile we associate a statistical weight w_i

$$w_i = \frac{\Delta V_i}{\sum_{\substack{k=1 \\ all 32 tiles}}^{32} \Delta V_k} . \quad (8-8)$$

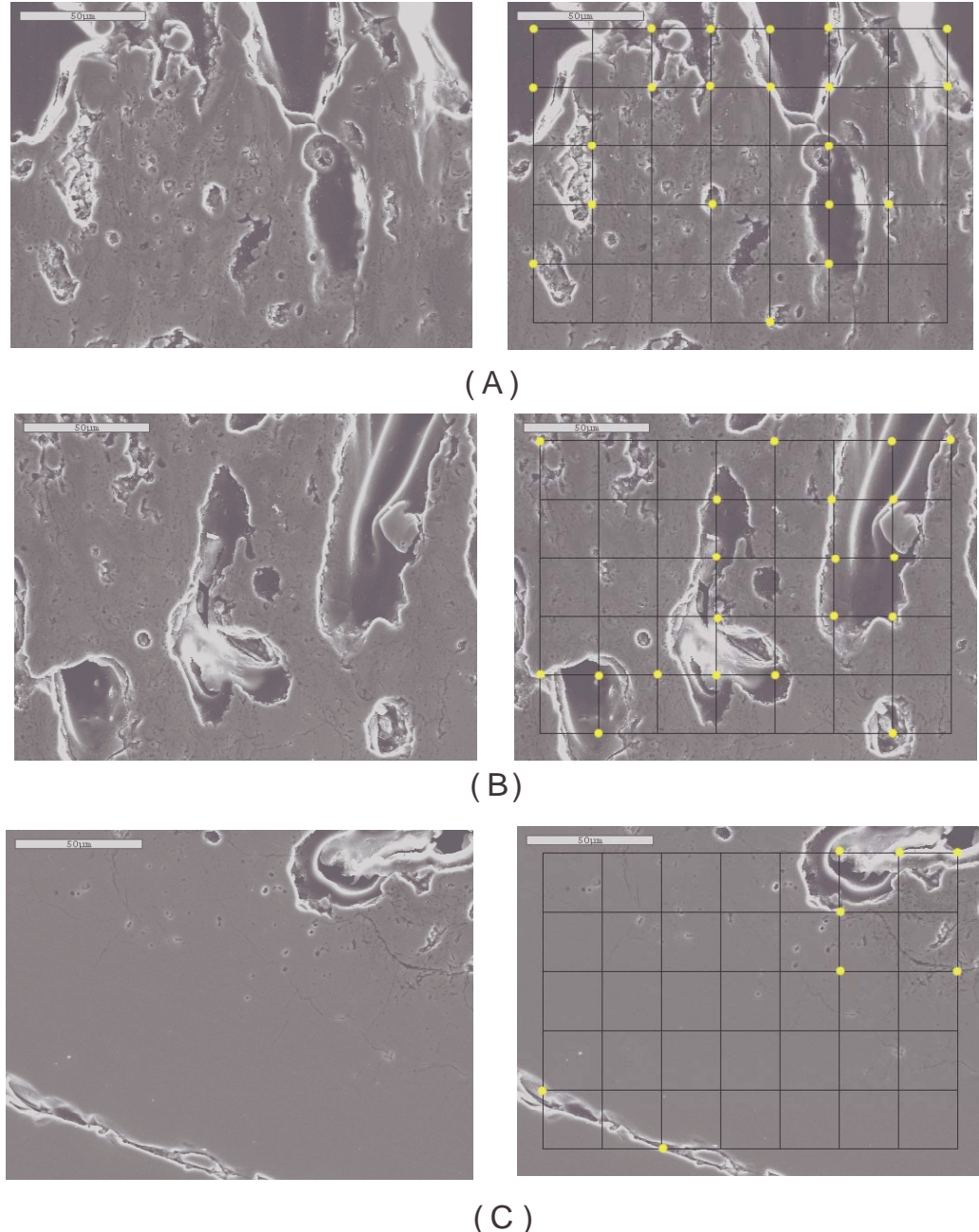


Figure A-4. Selected tile images of the sp-Si sample at a magnification of x650. The right column displays rectangular grids positioned over the images of the material. The bright circular marks denote that the grid intersection resides over a void. A) Near-surface image; B) Image of the sp-Si bulk; C) Near the interface sp-Si/Si.

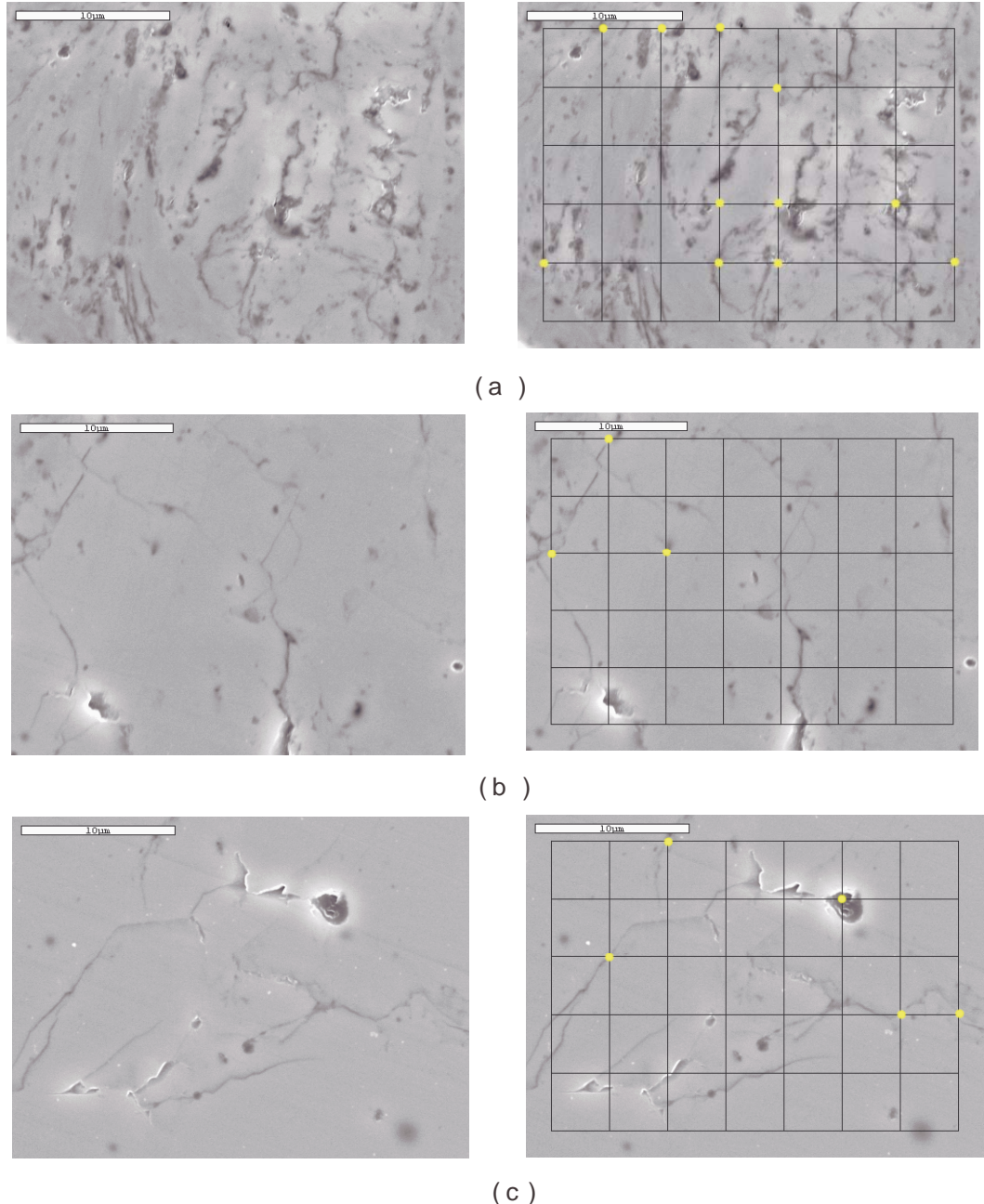


Figure A-5. Selected tile images of the sp-Si sample at a magnification of x3000. The right column displays rectangular grids positioned over the images of the material. The bright circular marks denote that the grid intersection resides over a void. A) Near-surface image; B) Image of the sp-Si bulk; C) Near the interface sp-Si/Si.

The total porosity of the sp-Si sample will be

$$P_{sp-Si} = \sum_{\substack{i=1 \\ all 32 tiles}}^{32} (P_i^{micro} + P_i^{nano}) w_i , \quad (8-9)$$

which takes into account the fact that the volume is an additive quantity.

Results and Discussion

The point count measurement contains a certain error. It is due mainly to microscopy edge effects near the pore boundaries, which appear bright (Figure 8-4). In all cases when a grid intersection was positioned over a bright pore-edge area, we proceeded as follows:

- The corresponding mark was counted into the porosity if the intersection was positioned within the inner (towards the pore) lying half of the bright area;
- The corresponding mark was counted into the porosity and also counted as error if the intersection was positioned within the outer lying half of the bright area.

Thus, the calculated total porosity is an upper limit to the true porosity, and the error corresponds to an interval of possible lower values. The linear grids used in the stereological measurements consist of lines with finite thickness. The points of intersection of two lines were therefore considered to be located on the pixel at the upper right corner of the intersection.

The edge effects and the error associated with them were largely absent in the high-resolution images for nano-porosity calculation. Still, some error was generated in these cases due to the fact, that certain localized areas were not flat. The marks within them were counted into the error of the measurement and into the nano-porosity as well. As a result, the error of the nano-porosity count is larger compared to its counterpart in the macro-porosity measurement.

Applying the equation (8-9), we calculated the micro-porosity of sp-Si to be 26.0% with an accuracy of 2.0%. The nano-porosity is 16.9% with an accuracy of 4.0%. Therefore, the total porosity of sp-Si is calculated to be 42.9% with an accuracy of 6.0%. This should be interpreted to mean that true porosity lies within an interval with numerical length of 6%, defined by the upper limit of 42.9% and the lower limit of 36.9%:

$$36.9\% \leq P_{sp-Si} \leq 42.9\% . \quad (8-10)$$

Figure 8-6 depicts the radial distribution of porosity. The term “radial” refers to the cylindrical symmetry of the sp-Si sample, where Y is the axis of the cylinder, and one of its radii lies along the X axis (Figures 8-1 and 8-2). The porosity is lowest at the sample edges and exhibits peaks symmetrically positioned with respect to the Y axis. It can also be noticed that the porosity can occupy values higher than 80% in certain small localities. Another distribution is shown on Figure 8-7. This is the radial porosity distribution of a surface layer with thickness of approximately 100 μm . P occupies high values even at the edges and is peaked in the middle of the sample. Under such circumstances, metal contact deposition on the sp-Si surface will create a better coverage in the periphery of the sample and will be largely discontinued in its center.

Figure 8-8 displays a depth profile of porosity, achieved by averaging over horizontal slabs with thickness of around 50 μm . Figure 8-9 depicts a porosity depth profile, which has been achieved by averaging over layers with the same thickness as above. In this case, all points of the layers are equally distant from the surface. Both pro-

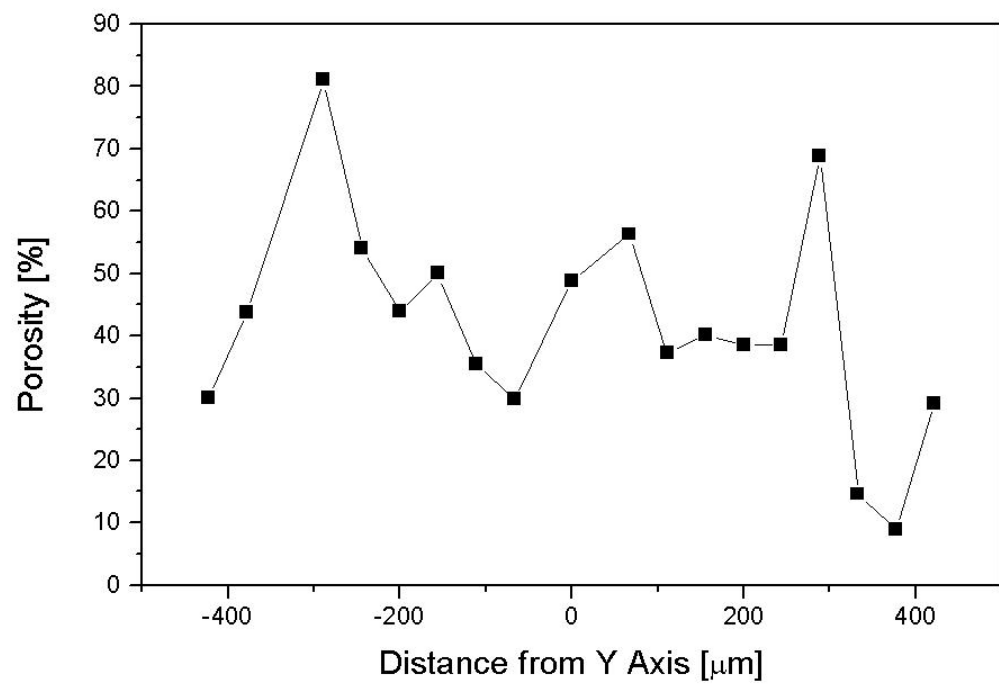


Figure 8-6. Radial distribution of porosity in sp-Si. The lines are a guide to the eye.

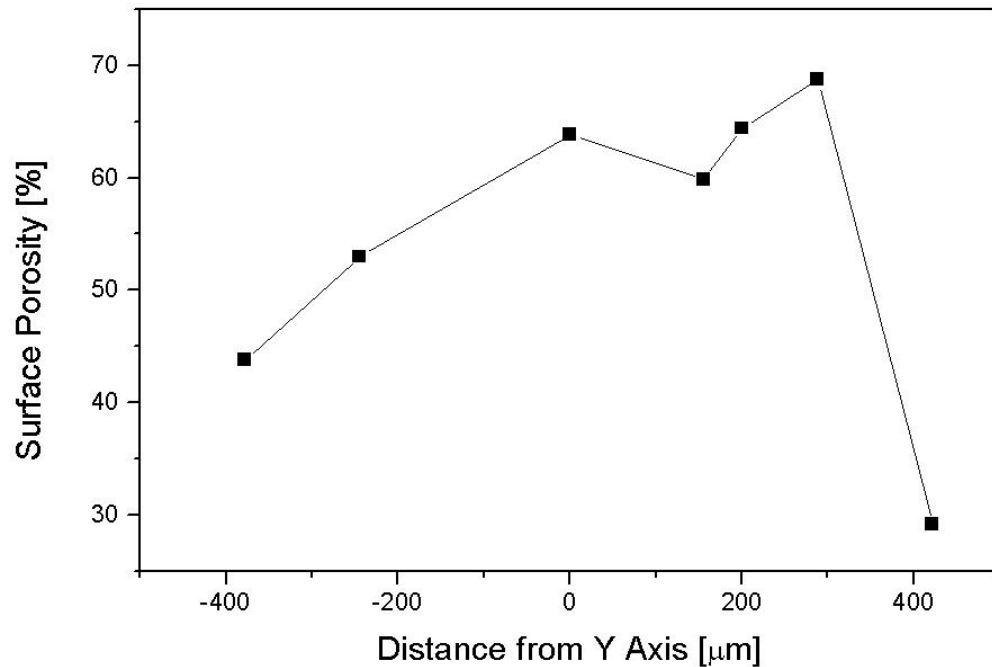


Figure 8-7. Radial distribution of porosity in a layer with thickness of 100 μm at the surface of sp-Si. The lines are a guide to the eye.

files show non-linear decrease of porosity, having lowest value of around a few percent near the sp-Si/Si interface.

Density of Spark-processed Si

The estimate of the density of sp-Si is based on a small-spot X-ray electron spectroscopy (XPS) depth profile of the material, published by Ludwig [3] (Figure 1-2). Since sp-Si is inhomogeneous, its average density will be

$$\rho_{sp-Si}^{solid\ phase} = \frac{m_{sp-Si}}{V_{sp-Si}} = \sum_k \rho_k \left(\frac{V_k}{V_{sp-Si}} \right), \quad (8-11)$$

where the sum is taken over all volumes of the various phases in sp-Si. The factor in the brackets represents the statistical weight of the density ρ_k of the corresponding phase k . It should be noted that (8-11) is calculated entirely based on information from the XPS measurement and as such it represents the density of the solid phase only. Then, the true density of sp-Si will be

$$\rho_{sp-Si} = \rho_{sp-Si}^{solid\ phase} (1 - P_{sp-Si}), \quad (8-12)$$

where P_{sp-Si} is the porosity of the material, calculated in equation (8-9).

To estimate (8-12), certain approximations are adopted. Based on previously published data for plasma-grown Si oxynitride materials with similar depth profiles of SiO_2 , Si and Si_3N_4 [44, 82, 83, 91, 109 - 113], we assume the connecting lines in the XPS diagram of sp-Si (Figure 1-2) to represent data points.

In detail, this assumption is based on the following:

- In the above references, the depth profile of N is typically peaked near the oxide/Si interface for all as-grown samples, which have not been subjected to additional treatment;

Figure 8-8. Depth profile of porosity in sp-Si. The averaging with depth has been performed over horizontal slabs, as shown in inset.

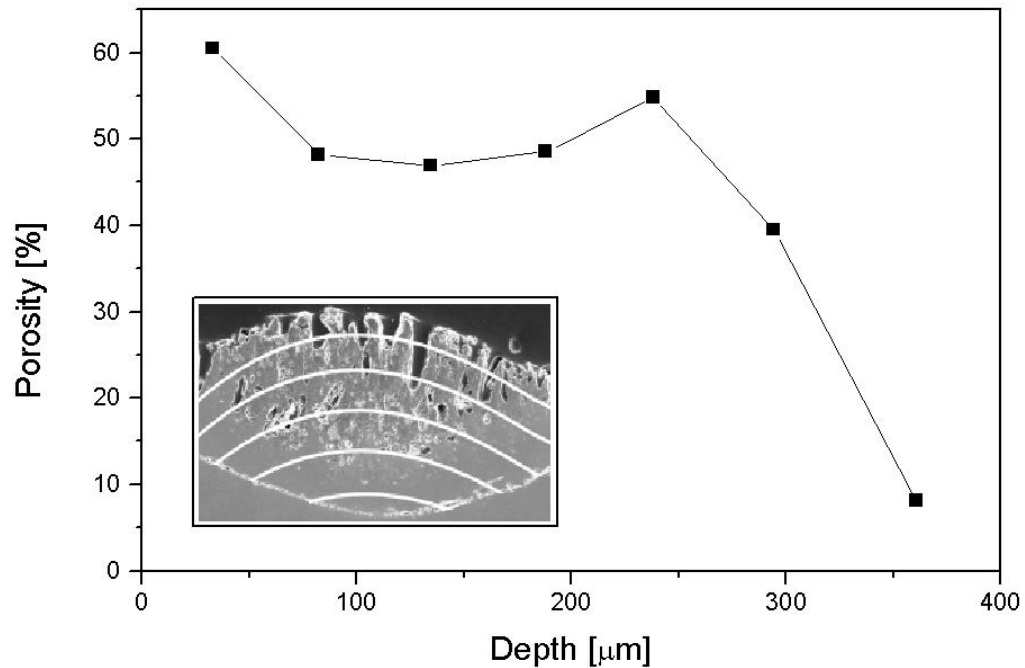


Figure 8-9. Depth profile of porosity in sp-Si. The averaging with depth has been performed over layers, equidistant from sp-Si surface (inset).

- The quoted references show the concentration of SiO_2 to decrease in a non-linear fashion, similarly to the profile shown in Figure 1-2, and the concentration of Si increases in a similar pattern.

Unless the plasma-grown Si oxynitride films have been subjected to a secondary treatment (annealing in N, implantation, secondary plasma treatments), the depth profiles of SiO_2 , N and Si exhibit behavior similar to the approximation shown on Figure 1-2. This approximation allows us to generate data points for the concentration of SiO_2 , crystalline Si (c-Si), amorphous Si (a-Si) and Si_xN_y for 250 horizontal slabs of sp-Si having thickness of 1 μm each (as in Figure 8-8, inset). As a second approximation, we assume for Si_xN_y $x=3$, $y=4$. This allows us to use the density of Si_3N_4 in the calculation.

The densities of the participating chemical compounds are: $\rho(\text{a-SiO}_2) = 2.4 \text{ g/cm}^3$ [114], $\rho(\text{c-Si}) = 2.3 \text{ g/cm}^3$ [115], $\rho(\text{a-Si}) = 2.2 \text{ g/cm}^3$ [116, 117] and $\rho(\text{a-Si}_3\text{N}_4) = 3.0 \text{ g/cm}^3$ [118]. Using these densities and equation (8-11), we determine the average solid phase density of sp-Si in each of the 250 slabs. The results are presented in Figure 8-10. The points of discontinuity are due to the first approximation in the calculation. ρ decreases from the value of 2.4 g/cm^3 , corresponding to the density of SiO_2 , to the value of 2.3 g/cm^3 , corresponding to the density of c-Si.

The average density for the entire solid phase is determined by equation (8-11), where the averaging is conducted over the 250 slabs. However, since the surface of sp-Si and the interface sp-Si/Si substrate cannot be mapped correctly, the precise volume of each slab cannot be estimated. In order to avoid this obstacle, we assumed all slabs to have equal volumes. Mathematically, this means that their densities enter the sum (8-11)

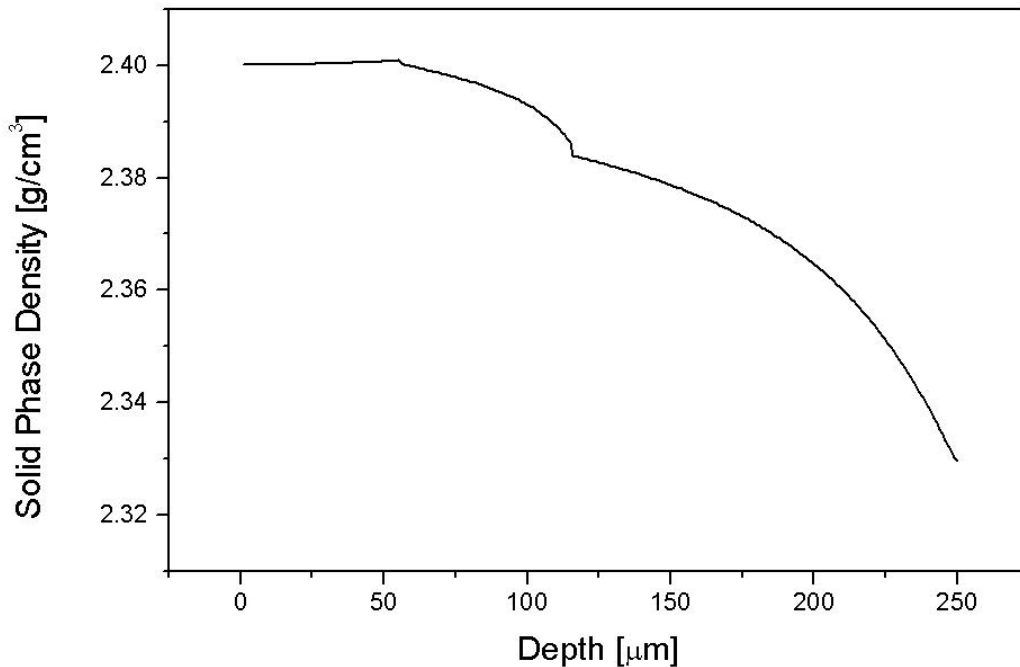


Figure 8-10. Depth profile of sp-Si density. The averaging with depth has been performed over 250 horizontal slabs, as shown in the inset of Figure 8-7.

with equal weights and artificially increase the volume contributions from the surface and interface areas, which are otherwise small. Therefore, the calculated value of the sp-Si density is an estimate, which overstates the participating amounts of a-SiO₂ and c-Si.

Our calculation determines $\rho_{sp-Si}^{solid\ phase}$ to be 2.38 g/cm³. Since most of the volume of the material is occupied by SiO₂ ($\rho(a-SiO_2) = 2.4\text{ g/cm}^3$), the value of 2.38 g/cm³ shows that Si dioxide is the main contributor to the density of sp-Si. The true density of sp-Si, after taking into account the contributions from both the solid phase and the voids in the material, is calculated by equation (8-12):

$$\rho_{sp-Si} = 1.36 \text{ g/cm}^3. \quad (8-13)$$

Conclusions

The total volume fraction of porosity in sp-Si is calculated to be approximately 43%. The surface porosity of the material is high, reaching up to 69% in the central area of the sample. This study was conducted for sp-Si specimen, grown within a fixed set of processing parameters. Despite that the variation of the growth parameters may influence the microstructure of the material, our results have general applicability and describe a non-traditional method for successful porosity measurements. The density of sp-Si is estimated to be 1.36 g/cm³. The main contribution to the density of this material comes from a-SiO₂, which occupies most of its volume.

LIST OF REFERENCES

- [1] R. E. Hummel, S.-S. Chang, *Appl. Phys. Lett.* **61** (1992) 1965.
- [2] M. H. Ludwig, Ch. 5, in *Handbook of Optical Properties: Optics of Small Particles*, R. E. Hummel (Ed.), CRC Press, Boca Raton, FL, 1996.
- [3] M. Ludwig, *Crit. Rev. Solid State Mater. Sci.* **21** (1996) 265.
- [4] R. E. Hummel, M. H. Ludwig, *J. Lumin.* **68** (1996) 69.
- [5] M. H. Ludwig, A. Augustin, R. E. Hummel, Th. Gross, *Appl. Phys.* **80** (1996) 5318.
- [6] M. Stora, Ph. D. Dissertation, University of Florida, 2000.
- [7] A. K. Bhatia, S. O. Karstner, *Solar Phys.* **182** (1998) 37.
- [8] L. Zhang, R. Cameron, R. A. Holt, T. J. Scholl, S. D. Rosner, *Astrophys. J.* **418** (1993) 307.
- [9] P. J. Sarre, M. E. Hurst, T. L. Evans, *Astrophys. J. Lett.* **471** (1996) L107.
- [10] H. Mutschke, B. Begemann, J. Dorschner, J. Gurtler, B. Gustafson, T. Henning, R. Stognienko, *Astron. Astrophys.* **333** (1998) 188.
- [11] F. J. Lovas, *Astrophys. J.* **193** (1974) 265.
- [12] M. C. Zerner, Ch. 8, in *Reviews of Computational Chemistry* (Vol. 2), K. B. Lipkowitz (Ed.), VCH Publishers, New York, 1991.
- [13] C. C. J. Roothaan, *Rev. Mod. Phys.* **23** (1951) 69.
- [14] J. A. Pople, D. P. Santry, G. A. Segal, *J. Chem. Phys.* **43** (1965) S129.
- [15] J. A. Pople, D. L. Beveridge, P. A. Dobosh, *J. Chem. Phys.* **47** (1967) 2026.
- [16] N. J. Bunce, J. E. Ridley, M. C. Zerner, *Theor. Chim. Acta* **45** (1977) 283.
- [17] J. E. Ridley, M. C. Zerner, *J. Mol. Spectrosc.* **76** (1979) 71.
- [18] Ira N. Levine, *Quantum Chemistry*, 4th Ed. Prentice-Hall Inc., New Jersey, 1991.

- [19] A. Szabo and N. S. Ostlund, Modern Quantum Chemistry, 1st Rev. Ed., McGraw-Hill, 1982.
- [20] T.A. O'Brien, P. D. Rack, P. H. Holloway, M. C. Zerner, *J. Lumin.* **78** (1998) 245.
- [21] HyperChem ver. 6.0 program code and Manual, HyperCube Inc., Gainesville, Florida, 2000.
- [22] J. Ridley, M. C. Zerner, *Theor. Chim. Acta* **32** (1974) 111.
- [23] A. D. Bacon, M. C. Zerner, *Theor. Chim. Acta* **53** (1979) 21.
- [24] D. P. Santry, G. A. Segal, *J. Chem. Phys.* **47** (1967) 158.
- [25] J. Polihronov, M. Hedstrom, R. Hummel, H.-P. Cheng, *J. Lumin.* **96** (2002) 119.
- [26] G. Maier, G. Mihm, H. P. Reisenauer, *Angew. Chem. Int. Engl.* **19** (1980) 52.
- [27] G. Maier, G. Mihm, R. O. W. Baumgartner, H. P. Reisenauer, *Chem. Ber.* **117** (1984) 2337.
- [28] G. Maier, G. Mihm, H. P. Reisenbauer, *Chem. Ber.* **117** (1984) 2351.
- [29] C. L. Kreil, O. L. Chapman, G. T. Burns, T. J. Barton, *J. Am. Chem. Soc.* **102** (1980) 841.
- [30] T. Brix, N. L. Arthur, P. Potzinger, *J. Phys. Chem.* **93** (1989) 8193.
- [31] R. K. Vatsa, A. Kumar, P. D. Naik, H. P. Upadhyaya, U. B. Pavanaja, R. D. Saini, J. P. Mittal, *J. Polym. Sci. Part A: Polym. Chem.* **25** (1996) 129.
- [32] E. Bastian, P. Potzinger, A. Ritter, H. -P. Schuchmann, C. von Sonntag, G. Weddle, *Ber. Bunsenges. Phys. Chem.* **84** (1980) 56.
- [33] T. J. Drahak, J. Michl, R. West, *J. Am. Chem. Soc.* **101** (1979) 5427.
- [34] J. J. P. Stewart, *J. Computer-Aided Mol. Design* **4** (1990) 1.
- [35] J. J. P. Stewart, MOPAC 2000.00 Manual, Fujitsu Ltd., Tokyo, Japan, 2000.
- [36] R. E. Hummel, A. Morrone, M. H. Ludwig, S.-S. Chang, *Appl. Phys. Lett.* **63** (1993) 2771.
- [37] R. E. Hummel, M. H. Ludwig, S.-S. Chang, G. LaTorre, *Thin Sol. Films* **255** (1995) 219.
- [38] N. Shepherd, private communication (2002).
- [39] R. E. Hummel, K. Kim, private communication (2002).

- [40] J. Hack, master's thesis, University of Florida, 1995.
- [41] S. Hasegawa, S. Sakamori, M. Futatsudera, T. Inokuma, Y. Kurata, *J. Appl. Phys.* **89** (2001) 2598.
- [42] L. Itoh, Y. Hayamitzu, T. Abe, *Mat. Sci. and Engn. B* **4** (1989) 309.
- [43] Y. Cros and J. Krautwurm, *J. Non-Cryst. Sol.* **187** (1995) 385.
- [44] T. Hori, H. Iwasaki, K. Tsuji, *IEEE Trans. Of Electr. Dev.* **36** (1989) 340.
- [45] K. Nakajima, K. Kimura, A. Kurokawa, S. Ichimura, H. Fukuda, *Jap. J. Appl. Phys. Pt. 1* **40** (2001) 4011.
- [46] F. Shimura, R. S. Hockett, *Appl. Phys. Lett.* **48** (1986) 224.
- [47] J. -W. Lee, N-I. Lee, J.-I. Han, C.-H. Han *IEEE Electr. Dev. Lett.* **18** (1997) 172.
- [48] J. -W. Lee, N.-I. Lee, S.-H. Hur, C.-H. Han, *J. Electrochem. Soc.* **144** (1997) 3283.
- [49] M. Suzuki, Y. Saito, *Appl. Surf. Sci.* **173** (2001) 171.
- [50] J. T. Yount, P. M. Lenahan, G. J. Dunn, *IEEE Trans. Nucl. Sci.* **39** (1992) 2211.
- [51] A.M. Ferrari, E. Garrone, G. Spoto, P. Ugliengo, A. Zecchina, *Surf. Sci.* **323** (1995) 151.
- [52] A. Weiss, A. Weiss, *Z. Anorg. Allg. Chem.* **276** (1954) 95.
- [53] A. Zecchina, S. Bordiga, G. Spoto, L. Marchese, G. Petrini, G. Leofanti, M. Padovan, *J. Phys. Chem.* **96** (1992) 4985.
- [54] B. Bunker, D. Haaland, K. Ward, T. Michalske, W. Smith, J. Binkley, C. Melius, C. Balfe, *Surf. Sci.* **210** (1989) 406.
- [55] M. Du, private communication (2000).
- [56] L.L. Hench, J.K. West, *Ann. Rev. Mater. Sci.* **25** (1995) 37.
- [57] CAChe 4.4 User Guide, Fujitsu Ltd., 2001.
- [58] G. A. N. Connell, R. J. Temkin, *Phys. Rev. B* **9** (1974) 5323.
- [59] D. Beeman, B. L. Bobbs *Phys. Rev. B* **12** (1975) 1399.
- [60] S. Kugler, G. Naray-Szabo, *J. Non-Cryst. Sol.* **97 & 98** (1987) 503.
- [61] K. Winer, *Phys. Rev. B* **35** (1987) 2366.

- [62] N. Mousseau, L. J. Lewis, Phys. Rev. Lett. **78** (1997) 1484.
- [63] N. Mousseau, G. T. Barkema, Phys. Rev. E. **57** (1998) 2419.
- [64] S. J. Clack, J. Crain, G. J. Ackland, Phys. Rev. B **55** (1997) 14059.
- [65] R. M. Valladares, C. C. Diaz, M. Arroyo, M. A. McNellis, A. A. Valladares, Phys. Rev. B **62** (2000) 2220.
- [66] P. Melinon, P. Keghelian, X. Blase, J. Le Bruise, A. Perez, E. Reny, C. Cros, M. Pouchard, Phys. Rev. B **58** (1998) 12590.
- [67] F. Wooten, K. Winer, D. Wearie, Phys. Rev. Lett. **54** (1985) 1392.
- [68] R. Car, M. Parrinello, Phys. Rev. Lett. **60** (1988) 204.
- [69] N. Zотов, M. Marinov, N. Mousseau, G. Barkema, J. Phys. Cond. Matt. **11** (1999) 9647.
- [70] G. T. Barkema, N. Mousseau, Phys. Rev. Lett. **81** (1998) 1865.
- [71] H. Weiqiang, D. Zishang, W. Saizhen, M. Zhusui, Z. Jianhua, Chin. Sci. Bulletin, **41** (1996) 1139.
- [72] L. -S. Wang, J. B. Nicholas, M. Dupuis, H. Wu, S. Colson, Phys. Rev. Lett. **78** (1997) 4450.
- [73] S. J. Pennycook, “Navigating the Nanoworld with Z-Contrast STEM”, seminar presentation at the Dept. of Mater. Sci. and Eng., University of Florida, Feb. 19, 2002.
- [74] K. Raghavachari, C. M. Rohlffing, J. Chem. Phys., **89** (1998) 2219.
- [75] R. Fournier, S. Sinnott, A. DePristo, J. Chem. Phys. **97** (1992) 4149.
- [76] S. Wei, R. N. Barnett and U. Landman, Phys. Rev. B. **55** (1997) 7935.
- [77] X. Jing, N. Troullier, D. Dean, N. Binggeli, J. R. Chelikowsky, Phys. Rev. B, **50** (1994) 12234.
- [78] O. Sankey, D. J. Niklewski, D. A. Drabold, J. D. Dow, Phys. Rev. B, **41** (1990) 12750.
- [79] A. Rubio, J. A. Alonso, X. Blasé, L. C. Balbas, S. G. Louie, Phys. Rev. Lett., **77** (1996) 247.
- [80] J. Polihronov, R. Hummel, H. -P. Cheng, “Optical properties and energetics of oxygenated silicon ring-shaped clusters”, J. Luminescence, accepted for publication.

- [81] R. E. Hummel, N. Sheperd, D. Burton, *Appl. Phys. Lett.* **79** (2001) 3218.
- [82] R. P. Vasquez, A. Madhukar, F. J. Grunthaner, M. L. Naiman, *J. Appl. Phys.* **59** (1986) 972.
- [83] B. Brijs, J. Deleu, T. Conard, H. De Vitte, W. Vandervorst, K. Najajima, K. Kimura, I. Genchev, A. Bergmaier, L. Goergens, P. Neumaier, G. Dollinger, M. Dobeli, *Nucl. Instr. And Meth. In Phys. Res. B* **161-163** (2000) 429.
- [84] M. L. Monaghan, T. Nigam, M. Houssa, S. De Gendt, H. P. Urbach, P. K. De Bokx, *Thin. Sol. Films* **359** (2000) 197.
- [85] G. P. Kennedy, O. Buiu, S. Taylor, *J. Appl. Phys.* **85** (1999) 3319.
- [86] G. Tallarida, F. Cazzaniga, B. Crivelli, R. Zonca, M. Alessandri, *J. Non-Cryst. Sol.* **245** (1999) 210.
- [87] A. Borghesi, E. Bellandi, G. Guizetti, A. Sassella, S. Rojas, L. Zanotti, *Appl. Phys. A* **56** (1993) 147.
- [88] D. Landheer, G. C. Aers, G. I. Sproule, P. Khatri, P. J. Simpson, S. C. Gujrathi, *J. Appl. Phys.* **78** (1995) 1818.
- [89] D. Bouvet, P. A. Clivaz, m. Dutoit, C. Coluzza, J. Almeida, G. Margaritondo, F. Pio, *J. Appl. Phys.* **79** (1996) 7114.
- [90] A. Teramoto, H. Umeda, H. Tamura, Y. Nishida, H. Sayama, K. Terada, K. Kawase, Y. Ohno, A. Shigetomi, *J. Electrochem. Soc.* **147** (2000) 1888.
- [91] A. Glachant, *Thin Sol. Films* **254** (1995) 54.
- [92] R. E. Hummel, R. Enderlein, *Phys. Rev. B* **29** (1984) 1529.
- [93] R. E. Hummel, in *Encyclopedia of Analytical Chemistry*, R. A. Meyers (Ed.), John Wiley & Sons Ltd., Chichester, 2000, p. 9047.
- [94] R. Enderlein, R. E. Hummel, J. B. Andrews, R. J. Nastasi-Andrews, C. W. Shanley, *Phys. Stat. Solidi B* **88** (1978) 173.
- [95] R. J. Nastasi, Doctoral Dissertation, University of Florida 1976.
- [96] J. Polihronov, T. Dubroca, M. Manuel, R. E. Hummel, “Porosity and Density of Spark-processed Silicon”, submitted to *The Journal of Microscopy*.
- [97] F. Fajardo, unpublished data on Light-Emitting Si Achieved with Laser Ablation, University of Florida, 1998.
- [98] L. T. Canham, *Appl. Phys. Lett.* **57** (1990) 1046.

- [99] H. Wong, Microel. Reliab. **42** (2002) 317.
- [100] A. M. Danilevskii, V. B. Shuman, A. Yu. Rogachev, P. A. Ivanov, Semiconductors **29** (1995) 1063.
- [101] A. Konstantinov, C. I. Harris, A. Henry, B. Monemar, E. Janzen, 22nd Int. Confer. On the Phys. Of Semicond. **3** (1995) 2157.
- [102] V. Petrova-Koch, T. Muschik, Thin Sol. Films **255** (1995) 246.
- [103] V. Petrova-Koch, T. Muschik, A. Kux, B. K. Meyer, F. Koch and V. Lehmann, Appl. Phys. Lett. **61** (1992) 943.
- [104] Ya. O. Roizin, A. Alexeev-Popov, S. A. Gevelyuk, D. P. Savin, E. Mugenski, I. Sokolska, E. Rysiakiewicz-Pasek, K. Marczuk, Phys. Chem. Glasses, **37** (1996) 196.
- [105] N. Shepherd, R. E. Hummel, “Improved Electroluminescence of Spark-processed Si by an Aerosol-Assisted Technique”, Physica Status Solidi A, accepted for publication.
- [106] N. Shepherd and R. E. Hummel, “A Model for the Electroluminescence of Spark-processed Si”, J. Phys. Chem. Solids, accepted for publication.
- [107] J. Yuan, D. Haneman, Appl. Phys. Lett. **67** (1995) 3328.
- [108] John C. Russ, R. T Dehoff, Practical Stereology, 2nd Ed., Kluwer Academic/ Plenum Publishers, New York, 2000.
- [109] E. P. Gusev, H.-C. Lu, E. L. Garfunkel, T. Gustafsson, M. L. Green, IBM J. Res. Develop. **43** (1999) no. 3.
- [110] K. Nakajima, K. Kimura, A. Kurokawa, S. Ichimura, H. Fukuda, Jap. J. Appl. Phys. **40** Pt. 1, (2001) 4011.
- [111] Y. Saito, Appl. Phys. Lett. **68** (1996) 800.
- [112] M. L. Monagan, T. Nigam, M. Houssa, S. De Gendt, H. P. Urbach, P. K. De Bokx, Thin Sol. Films, **359** (2000) 197.
- [113] M. Ueda, A. F. Beloto, H. Reuther, S. Parascandola, Surf. Coat. Technol. **136** (2001) 244.
- [114] N. Awaji, S. Ohkubo, T. Nakanishi, Y. Sugita, K. Takasaki, S. Komiya, Jap. J. Appl. Phys. Pt.2, **35** (1996) L67.
- [115] N. I. Koshkin, M. G. Shirkevich, Handbook of Elementary Physics, Mir Publishers, Moscow, 1977.

- [116] A. F. Ruppert, P. D. Persans, G. J. Hughes, K. S. Liang, B. Abeles, W. Landford, Phys. Rev. B, **44** (1991) 11381.
- [117] J. S. Custer, M. O. Thompson, D. C. Jacobson, J. M. Poate, S. Roorda, W. C. Sinke, F. Spaepen, Appl. Phys. Lett. **64** (1994) 437.
- [118] T. Hirai, T. Goto, J. Mater. Sci. **16** (1981) 2877.

BIOGRAPHICAL SKETCH

The author was born April 26, 1969, in the city of Velingrad, Bulgaria. Most of his childhood years were spent in the city of Veliko Tarnovo. He received his high-school diploma with a medal and honors from I^{va} Gimnazia at the city of Veliko Tarnovo. His studies continued at the Faculty of Physics at the University of Sofia in Sofia, the capital city of Bulgaria. He graduated with a masters' degree in solid-state physics and methods of teaching physics. During his university education, he was awarded a governmental scholarship for undergraduate studies in physics. After graduation, he was accepted in a doctoral program in the laboratory of Prof. Krassimira Germanova at the Faculty of Physics. His graduate studies continued at the University of Florida, Gainesville, in the Department of Materials Science and Engineering. His work was mainly conducted in the group of Prof. Rolf Hummel with extensive collaboration with the group of Prof. Hailong Cheng at the Quantum Theory Project at the University of Florida. In the year 2002, he was awarded a masters' degree in Materials Science and Engineering.

Jeliazko Polihronov has authored several scientific publications in refereed journals. He is a member of the American Physical Society. Currently, he has accepted a postdoctoral position with the Department of Physics and Astronomy, University College London, United Kingdom.